Spins in organic semiconductors : revealing the dominant mechanisms of organic magnetoresistance


SPINS IN ORGANIC SEMICONDUCTORS
REVEALING THE DOMINANT MECHANISMS OF ORGANIC MAGNETORESISTANCE
PAUL JANSSEN

Spins in organic semiconductors

Revealing the dominant mechanisms of organic magnetoresistance

PROEFSCHRIFT

ter verkrijging van de graad van doctor aan de
Technische Universiteit Eindhoven, op gezag van de
rector magnificus, prof.dr.ir. C.J. van Duijn, voor een
commissie aangewezen door het College voor
Promoties in het openbaar te verdedigen
op maandag 9 september 2013 om 16.00 uur

door

Paul Janssen

geboren te Roermond

Dit proefschrift is goedgekeurd door de promotor:

prof.dr. B. Koopmans

A catalogue record is available from the Eindhoven University of Technology Library.
ISBN: 978-90-386-3436-4

This research is supported by the Dutch Technology Foundation STW, which is the applied science division of NWO, and the Technology Programme of the Ministry of Economic Affairs (project number 06628).

Cover design by P. Janssen: *An artist's impression of my PhD thesis.*

Printed by Ipskamp Drukkers B.V., Enschede.

Preface

Organic semiconductors are a class of materials which have semiconducting properties and consist mostly of carbon and hydrogen atoms. Due to their relative ease of processing, chemical tunability and possible low costs, organic semiconductors provide exceptional promise for electronic applications. Organic semiconductor devices can show a surprisingly large room-temperature magnetoresistance effect at relatively small magnetic fields, an effect often referred to as organic magnetoresistance. Cheap plastic sensor technology has already been suggested as an example of its application potential. Nevertheless, the desire to unravel the excitingly new physics behind the organic magnetoresistance effect has been the major motivation for intensive experimental and theoretical research over the past years.

Several mechanisms have been proposed in the literature regarding organic magnetoresistance, and novel concepts have been introduced. At this point, the most successful mechanisms rely on the spin selective reaction of (charge carrying) particles, where a magnetic field suppresses the spin mixing of the particle pairs prior to the reaction. Although the microscopic mechanisms regarding spin interactions between the particles in organic materials are well understood nowadays, there is an on-going debate as to which pairs of spin carrying particles are influencing the current in such a drastic manner.

This thesis aims to reveal the dominant mechanisms underlying the organic magnetoresistance effect. Therefore, a combination of simulations and experimental results will be presented. This is done in Chapters 3–7, which can be read independently from the rest of this thesis. However, the reader is kindly referred to Chapters 1 and 2 which provide a basic introduction and a discussion of the current perspectives in the field of spins in organic semiconductors. Finally, the last Chapter concludes the work and gives an outlook on future research.

Paul Janssen, Eindhoven, July 2013.

Contents

Preface **1**

1 Introduction **5**
1.1 Organic semiconductors 6
1.2 Spins in organic semiconductors 8
1.3 Outline of this thesis 10

2 Current perspectives on magnetic field effects in organic semiconductors **13**
2.1 Charges in organic semiconductors 14
2.2 Spins in organic semiconductors 17
2.3 Organic magnetoresistance 19
2.4 Modeling of organic magnetoresistance 27
2.5 Conclusion 32

3 Unraveling the magnetic field effect lineshape **35**
3.1 Introduction 36
3.2 Empirical lineshapes 38
3.3 Results and discussion 43
3.4 Conclusion 48

4 Temperature and voltage dependence of magnetic field effects in organic semiconductors **49**
4.1 Introduction 50
4.2 Methods 51
4.3 Results and discussion 54
4.4 Conclusion 61

5 Tuning spin interactions in organic semiconductors 65
5.1 Introduction 66
5.2 Methods 71
5.3 Results and discussion 72
5.4 Conclusion 80

6 Investigating the influence of the triplet energy alignment on organic magnetoresistance 87
6.1 Introduction 88
6.2 Theory 89
6.3 Methods 92
6.4 Results and discussion 95
6.5 Conclusion 99

7 The role of minority carriers in the frequency dependence of organic magnetoresistance 101
7.1 Introduction 102
7.2 Methods 103
7.3 Frequency dependence 105
7.4 Admittance spectroscopy 106
7.5 Device modeling 110
7.6 Conclusion 111

8 Conclusions and outlook 113
8.1 Conclusions 114
8.2 Outlook 114

Summary 117

Curriculum vitae 121

Publications and presentations 123

Acknowledgements / Dankwoord 127

Bibliography 129

Index 143

1

Introduction

This Chapter provides a basic introduction to the research field of spins in organic semiconductors. First, a brief overview about organic semiconductors is given, highlighting their unique potential and applications in current and future technologies. Then, in the second part of this Chapter, we elucidate on the intriguing role of spins in organic materials and zoom into the novel and exciting field of organic spintronics. Here, we discuss the recently discovered organic magnetoresistance (OMAR) effect, which causes surprisingly large changes in the current through organic semiconductor devices. Finally, the Chapter ends with an outline of this thesis.

1.1 Organic semiconductors

Organic semiconductors (OSC) are a class of materials which have semiconducting properties and consist mostly of carbon and hydrogen atoms.[1,2] They can roughly be subdivided into two categories, namely small molecules (see e.g. Fig. 1.1b,d) and polymers (Fig. 1.1a,c). The first are a class of compounds with a well-defined molecular weight and structure, whereas the latter, by contrast, consist of long-chain molecules with an indeterminate number of molecular repeat units.

History

Although organic materials are often thought to be insulating, it was already discovered in the 1950s that specific organic materials have fairly good electrical conductivity.[3] However, it was not until 1977 that the discovery of highly conducting (doped) polymers really started the active research field of organic electronics.[4] During the past decades, thanks to a global collaborative effort of physicists, chemists and material scientists, the field has evolved from a mere scientific curiosity to a potentially important technology for consumer electronics. In recognition of the major importance for the field of organic electronics, Heeger, MacDiarmid and Shirakawa were awarded the Nobel Prize in Chemistry in the year 2000 for "the discovery and development of conductive polymers".

Apart from conducting electricity, organic semiconductors have another scientific and technological noteworthy property: they can emit light. Electroluminescence from organic materials was already discovered in 1953 by Bernanose and coworkers.[5] Nevertheless, it took until 1987 before the first organic light-emitting diode (OLED) was created by Tang and VanSlyke.[6] They reported on an electroluminescent device using organic small molecules as the emitting layer. The organic layer, prepared by vapor deposition, was sandwiched between two electrodes and the device achieved high efficiency at low driving voltages. Their discovery demonstrated that organic materials can indeed be viable alternatives for optoelectronic applications. Only three years later, Burroughes and coworkers reported on the first OLED using conjugated polymers.[7]

Applications

Organic semiconductors provide exceptional promise for (future) electronic applications. They have several significant advantages over their inorganic counterparts, with, most notably, their seemingly endless chemical tunability. Moreover, they enable unique device properties such as flexibility and transparency.[8] Furthermore, their relative ease of fabrication, such as the possibility of roll-to-roll

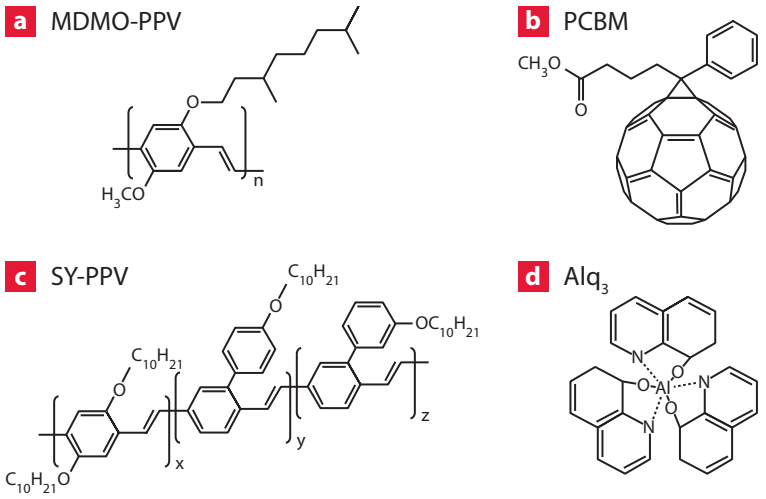

Figure 1.1 | Organic materials as used throughout this thesis. a | poly[(2-methoxy-5-(3,7-dimethyloctyloxy))-1,4-phenylenevinylene] (MDMO-PPV), **b |** [6,6]-phenyl-C_{61}-butyric acid methyl ester (PCBM), **c |** phenyl substituted poly(1,4-phenylenevinylene) (SY-PPV) and **d |** tris-(8-hydroxyquinoline) aluminum (Alq_3).

processing, could result in low-cost devices.[9] Currently, organic semiconductors are beginning to enter the commercial world. At this moment, one of their main applications is in organic light-emitting diodes.

Using organic semiconductors, and especially conjugated polymers, as light-emitting material has several technological advantages. Unlike most inorganic counterparts, polymers can easily be solution processed, enabling roll-to-roll fabrication of large-area displays. Since the organic material can even be applied on a flexible substrate, this allows engineers to develop completely new types of light sources as compared to the traditional incandescent light bulbs. As an example, recently researchers have developed OLEDs which can be integrated in car roofs.[10] The OLEDs are transparent when switched off, allowing for a clear view outside the vehicle, yet providing light only within the vehicle when switched on. Moreover, the light emission from OLEDS can be tuned by simply changing the chemical structure of the polymer[11] or by adding phosphorescent triplet emitters[12] into the active layer.

Another exceptionally promising application of organic semiconductors are organic photovoltaic cells (OPV).[13] Here, the organic materials are not used to create light, but to convert it into electricity. Solar energy is (potentially) the largest source of renewable energy. Organic photovoltaic cells have several advantages over the conventional silicon based cells. Foremost, they can be produced on light, cheap, flexible and even biodegradable substrates.[14] These

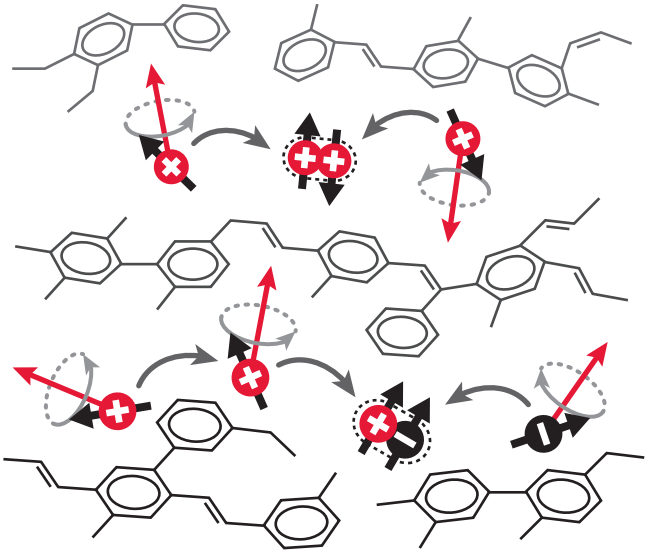

Figure 1.2 | Artist's impression of spins in organic semiconductors. Charge carriers can hop from localized site to site through a disordered organic semiconductor. At each site, the spin of the carrier interacts with a local, randomly orientated, magnetic field called the hyperfine field. As a result, the spins precess around this local magnetic field. Charge carriers also undergo spin-dependent interactions with each other, leading to the formation of new (quasi)particles. These concepts will be explained in more detail in Chapter 2.

unique properties enable OPVs to conquer an alternative market instead of competing with current silicon-based cells. Although great progress has been made over the last years and OPVs have reached efficiencies of more than 10%,[15] significant advances are still required to make organic photovoltaic technologies economically fully viable. Besides these (near-to-market) applications, organic semiconductors are envisioned in a whole range of devices including organic field-effect transistors (OFET),[16–18] organic memory cells,[19] memristors[20] and even energy harvesting ratchets.[21]

1.2 Spins in organic semiconductors

Nowadays, most traditional electronic devices only use the charge of electrons to transport or store information. A whole new world of opportunities emerges when also the intrinsic spin of the charge carriers is exploited. In doing so, we enter the realm of spintronics.[22,23] From an application point of view, we can add the spin degree of freedom to conventional charge-based electronic devices or use the spin alone for e.g. quantum computing.[24,25] A famous example of an

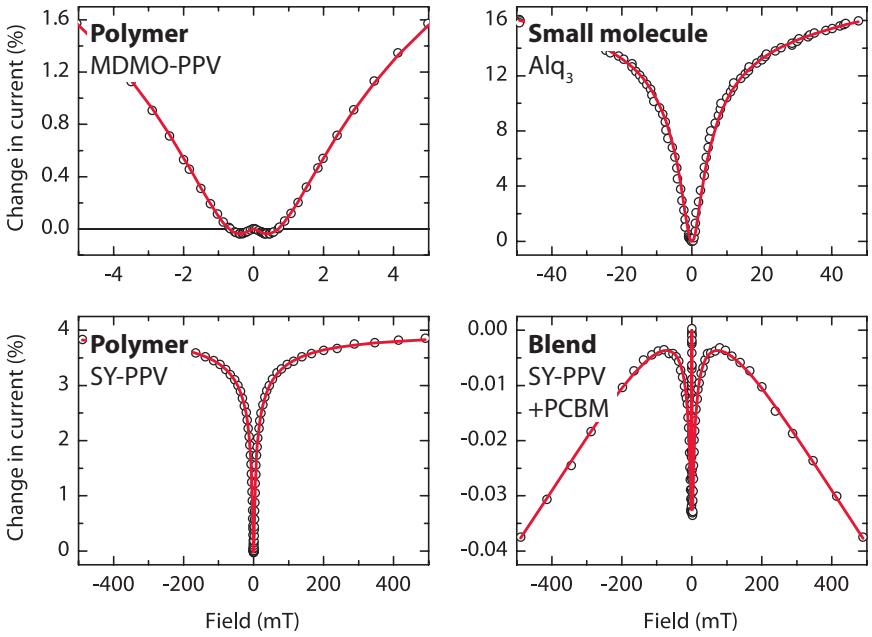

Figure 1.3 | The many faces of organic magnetoresistance traces. The change in the current as a function of magnetic field is shown for various organic devices. One can observe an extremely rich behavior of the magnetic field effect with very pronounced differences in both the amplitudes and line widths.

application is the read head of every modern hard disk drive. The discovery of a spintronic effect called giant magnetoresistance has led to an enormous increase in sensitivity and resulted in an unprecedented miniaturization of the read head, which revolutionized magnetic data storage over the last decades. For "the discovery of giant magnetoresistance",[26,27] Grünberg and Fert were awarded the Nobel Prize in Physics in the year 2007. Spintronics has the potential advantages of non-volatility, faster data processing and lower electric power consumption.

Organic magnetoresistance

Since spintronics relies on the detection and manipulation of spin states, the spin lifetime needs to be long enough in order to do so. In organic materials, extremely long spin lifetimes of orders of magnitude longer than metals, have been reported.[28] Therefore, an obvious next step is to combine the fields of spintronics and organic semiconductors, leading to the novel research field of organic spintronics.[29,30] This rapidly growing field deals with spin physics and magnetic field effects in organic materials (illustrated in Fig. 1.2). The first experiments on the influence of magnetic fields on organic semiconductors date back

to the 1960s. Johnson and coworkers [31] discovered that the delayed fluorescence of anthracene single crystals is quenched by applying an external magnetic field and Frankevich and coworkers [32] showed the photocurrent also depends on the magnetic field. But it was not until the beginning of the 21^{st} century, when it was discovered that the current trough small molecule [33] or polymer [34] based OLEDs is changed considerably by applying an external magnetic field, that the field really emerged and attracted a broad scientific interest. The research group of Wohlgenannt [34,35] showed that this "organic magnetoresistance" (OMAR) effect is found in a wide range of organic materials. Currently, the OMAR effect is recognized as one of the largest, room-temperature, low-field magnetoresistance effect in non-magnetic devices. Besides OMAR, the field of organic spintronics also involves a variety of other topics such as the injection and detection of spins in organic semiconductors, [36–39] organic magnets [40] and single molecule spintronics. [41,42]

During the last decade, OMAR has puzzled the young field of organic spintronics. Even though recently writable OLED displays [43] and cheap plastic sensor technology [44] have been proposed as an example of its application potential, the fundamental understanding of the interactions of spins and charges in organic semiconductors remains the goal of the extensive experimental and theoretical research. It has been experimentally shown that the effect can be tuned by changing the operating conditions such as the applied voltage, temperature, electrodes and even the angle or frequency of the externally applied magnetic field. In doing so, one can observe an extremely rich behavior of the magnetic field effect with very pronounced changes in the amplitudes and line widths (see e.g. Fig. 1.3). To explain this intriguing effect, several mechanisms have been proposed in the literature. However, no single mechanism is currently able to explain all experimentally observed OMAR traces completely. Therefore, the goal of this thesis is:

> "*To reveal the dominant underlying mechanisms of OMAR and present a unified, quantitative framework to describe the experimentally observed trends.*"

By achieving this goal, we open up unprecedented means to bring OMAR research from a phase of passively observing magnetic field effects in the current, to a stage of really engineering devices to tailor the OMAR effect as desired.

1.3 Outline of this thesis

The previous sections illustrated the unique properties of organic semiconductors and highlighted some of their potential applications. Then, the research field of spins in organic semiconductors was introduced. This research has led

to the discovery of an intriguing organic magnetoresistance effect. The goal of this thesis is to reveal the dominant mechanisms underlying this organic magnetoresistance effect, aiming for a deeper fundamental understanding of the interactions of spins and charges in organic semiconductors.

First, in **Chapter 2**, we discuss the current perspectives on organic magnetoresistance and present a unified picture of the contemporary models. Furthermore, we will introduce theoretical models that have been developed to describe OMAR in a quantitative way. This Chapter will serve as a framework for the rest of the thesis. To analyze the underlying physics of the OMAR lineshapes, **Chapter 3** introduces a novel empirical function which has some major, non-trivial advantages. For example, using our empirical approach, we are able to extract the role of different relevant microscopic parameters such as the effective hyperfine fields in the organic materials.

Chapter 4 presents a detailed study, where we measure the magnetic field effects on the current as a function of the applied voltage and temperature. This Chapter shows a fully quantitative analysis of the OMAR lineshape. By studying the extracted parameters as a function of voltage and temperature, detailed information about the spin-interactions in the device can be obtained. Please refer to the Appendix of Chapter 4 for a detailed description of the measurement procedure as used throughout this thesis.

Then, in **Chapter 5**, we determine the dominant mechanism for OMAR by performing a proof of concept study using a polymer–fullerene blend. By changing the blending ratio, we can tune the spin and charge interactions in the device. By systematically investigating the magnetic field effect on the current, and correlating the experimental results to microscopic and device simulations, we show which mechanism dominates. **Chapter 6** extends the work of the previous Chapter by discussing a system where we intentionally dope our samples with an organic material to alter the energetic alignments in the devices. Using the analytical tool developed in the previous Chapters, we correlate changes in OMAR to changes in the energetic alignments of spin states in the organic semiconductor. Next, **Chapter 7** shows further evidence of the often highly non-trivial, yet significant contribution of device physics on OMAR. Here, we have measured the frequency dependence of OMAR and show, using a combination of experiments and device simulations, the important role of minority carriers. Finally, **Chapter 8** gives an outlook for future research in OMAR.

Current perspectives on magnetic field effects in organic semiconductors

2

In this Chapter, we will discuss the current perspectives on magnetic field effects in organic semiconductors, focusing on organic magnetoresistance (OMAR). First, we present a brief introduction of charge transport in organic semiconductor devices. Then, the role of the spin of the charge carriers in organic materials is examined. Thereafter, we will review the most successful mechanisms that have been proposed to explain OMAR, ultimately aiming for a unified picture. Finally, in the last part of this Chapter, we will introduce the theoretical models that have been developed to describe OMAR in a quantitative way. The unified picture, combined with explicit calculations, will serve as a valuable framework to investigate the underlying mechanisms throughout this thesis.

2.1 Charges in organic semiconductors

The fact that organic materials can be conducting seems surprising at first. Therefore, in order to understand the transport of charges in organic semiconductors, we start this section by examining the properties of charges on a single molecule or part of a polymer chain. Then, the hopping of charges from molecule to molecule is described and finally a general description for the transport of charges through real devices is presented.

Origin of conductivity

The origin of conduction in many organic materials lies in the presence of conjugation, which is derived from the Latin word "*coniugare*" that means "to link together". Conjugated molecules are conventionally described as a chain of carbon atoms which are linked by alternating single and double bonds. In such a molecule, three of the four valence electrons of each carbon atom contribute to the in-plane σ-bonds, formed by the hybridized sp^2 orbitals. The remaining electron then occupies the out-of-plane p_z orbital. This orbital can overlap with p_z orbital of neighboring carbon atoms, forming π-bonds. The electrons in the π-bonds do not belong to a specific carbon atom, but they are delocalized over the molecule. The delocalization of π-electrons gives the organic material conducting properties.

If the electrons in the π-bonds would indeed be delocalized over the entire molecule, the conduction would become metallic. In reality, however, due to geometric relaxation, the delocalization does not extend over the entire molecule and alternating shorter and longer bonds are formed. This effect is called Peierls disortion.[45] As a result, the energy of the highest occupied molecular orbit (HOMO) is lowered in energy, while that of the lowest unoccupied molecular orbit (LUMO) is raised. This energy difference, which is often called the bandgap, leads to the semiconducting properties of the organic material.

Charge transport

Now that the origin of conductivity in organic semiconductors has been addressed, we continue by describing the transport of charge carriers through the organic material. The organic semiconductors that are used in this thesis are characterized by energetic and positional disorder.[46,47] The energetic disorder is generally well described by a Gaussian density of states, as indicated in Fig. 2.1a.[48] Due to this disorder, the charge carriers are localized on single molecules or parts of the polymer chain.[49] Because of Coulomb interactions, the carriers induce a deformation of the local environment. The charge carriers and their accompanying deformations are called polarons. The molecules or parts of the polymer chain where the polarons are localized are referred to as

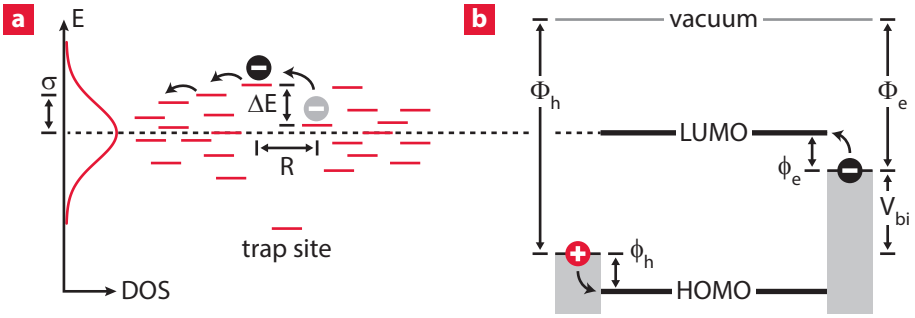

Figure 2.1 | Charge transport in organic semiconductors. a | Hopping of a charge carrier between localized sites in a disordered energy landscape. **b |** Energy diagram of an organic semiconductor device with electron (hole) injecting electrodes with workfunction $\Phi_{e(h)}$ and injection barriers $\phi_{e(h)}$ respectively, when applying a voltage equal to the built-in voltage V_{bi}

sites. Throughout this thesis, when speaking of electrons and holes, we thus actually mean negatively and positively charged polarons, respectively.

Due to the disorder, charge transport in most organic semiconductors occurs by phonon-assisted tunneling where the carriers hop from site to site through the organic material as indicated in Fig. 2.1a. The carrier may overcome the energy difference ΔE between two sites by absorbing or emitting a phonon. The rate at which the hops occur depends also on the wavefunction overlap. In the literature, this rate ω_{hop} is often described by Miller-Abrahams hopping: [50]

$$\omega_{hop} = \omega_0 e^{-2\alpha R} \times \begin{cases} e^{-\Delta E/k_B T} & \text{for } \Delta E > 0, \\ 1 & \text{for } \Delta E \leqslant 0, \end{cases} \tag{2.1}$$

where ω_0 is the attempt frequency, α the inverse wavefunction localization length, R the distance between the two sites and $k_B T$ the thermal energy. From Eq. (2.1) we can conclude that the hopping transport, as depicted in Fig. 2.1a, is a constant tradeoff between hopping distance, energy difference and wavefunction overlap. As a result, the conductivity strongly depends on the disorder. In most organic semiconductors, low-lying energy levels are present within the energy bandgap of the material, as also shown in Fig. 2.1a. [51] These sites are called traps, since the hopping rate out of these sites can become extremely low, depending on the trap depth.

To induce a current in an undoped organic semiconductor, charge carriers need to be injected into and transported through the material. This is usually done by sandwiching the organic layer between two electrodes, as illustrated in Fig. 2.1b. Here, electrons (holes) are injected into the LUMO (HOMO) of the organic layer. A difference in the workfunctions of the electrodes gives rise to a

so-called built-in voltage V_{bi} in the device. This voltage needs to be overcome before drift of charge carriers dominates diffusion. For optimal charge injection, the workfunction of the electrodes need to closely match the energy levels of the organic layer. When these energy levels are misaligned, an injection barrier arises which limits the current. In the absence of an energy barrier, the resulting contact is ohmic. By choosing specific combinations of the electrodes materials, we can either inject only one type of charge carrier (single-carrier devices) or both (double-carrier device).

At low voltages, the current density J as a function voltage V can be described by the Shockley diode equation: [52]

$$J = J_s \left(e^{qV/nk_B T} - 1 \right), \tag{2.2}$$

where J_s is the saturation current, q the elementary charge and n the so-called ideality factor. When increasing the voltage, the injection of charge carriers into the organic layers increases. As a result, a space-charge builds up which limits the current. This so-called space-charge limited current (SCLC) can be calculated by solving the Poisson and drift equations for a single-carrier device with ohmic contacts and is described by the Mott-Gurney equation: [53]

$$J = {}^{8}\!/_{9}\epsilon_0 \epsilon_r \mu \frac{V^2}{L^3}, \tag{2.3}$$

where ϵ_0 is the permittivity of free space, ϵ_r the relative permittivity of the organic semiconductor, μ the charge carrier mobility and L the thickness of the organic layer.

For a double-carrier device the oppositely charged electrons and holes can cancel each other's space-charge. This allows for much more carriers to be injected and a larger current as a result. However, the electrons and holes can also recombine which effectively reduces the current. In the case of Langevin recombination, the recombination rate R is given by the product of the electron n and hole p density:

$$R = \gamma n p, \tag{2.4}$$

where γ is the recombination coefficient which is proportional to the electron and hole mobility. Under the assumption of ohmic contacts, trap-free transport and weak recombination, the current density can be described by the Parmenter-Ruppel equation: [54]

$$J = {}^{8}\!/_{9}\epsilon_0 \epsilon_r \sqrt{\frac{2\pi \mu_e \mu_h (\mu_e + \mu_h)}{\mu_r}} \frac{V^2}{L^3}, \tag{2.5}$$

where $\mu_{e(h)}$ is the electron (hole) mobility and the recombination mobility μ_r for Langevin recombination type is defined as $\mu_r = r(\mu_e + \mu_h)$, with r a prefactor indicating the strength of the recombination.

Before the recombination of an electron and hole can take place, the two charge carriers have to approach each other in space. Since the two carriers have opposite charge, they attract each other due to Coulomb interaction, leading to the formation of so-called coulombically bound electron–hole (e–h) pairs. The distance r at which this happens is called the Onsager radius and is reached when the Coulomb energy is larger than the thermal energy: $r = e^2/4\pi\epsilon k_B T$.[55] In the organic semiconductors investigated in this thesis, the permittivity is approximately three times the permittivity of free space, leading to a radius on the order of 20 nm at room temperature.

Up until now, the mobilities of the charge carriers have been considered as constants and are defined as $\mu \equiv \langle v \rangle / E$, where $\langle v \rangle$ is the average velocity of the carrier and E the electric field. In most organic semiconductors, however, the mobility is not a constant and depends on the temperature, electric field and charge carrier concentration. In the devices as used in this thesis, the mobility can be described using a field-independent activated mobility and a field-dependent mobility of the stretched exponential form and is given by the following empirical relation:[56]

$$\mu(E, T) = \mu_0 \exp\left[-\frac{\Delta}{k_B T} + \gamma(T)\sqrt{E}\right], \tag{2.6}$$

where μ_0 is the zero-field mobility, Δ the characteristic activation energy and $\gamma(T) = B\,(1/k_B T - 1/k_B T_0)$ with B and T_0 empirical constants.

In passing we note that, next to electrical injection as described in this section, charges can also be generated by illuminating the organic layer. This process is called photoconduction. By absorbing a photon, an electron is excited from the HOMO to the LUMO, leaving a hole behind. This excited state can, under the right conditions, dissociate into free charge carriers. This is, in short, the working principle behind organic solar cells. However, all (electrical) measurements performed in this thesis will be done using (electrically) injected charges and not using photocurrents.[57]

2.2 Spins in organic semiconductors

So far, in describing the charge transport in organic semiconductor devices, the spin of the charge carriers was neglected. In this section, we will discuss the role of the spins of the charge carriers in organic semiconductors. In double-carrier devices, where both electrons and holes are present, recombination can take place from the coulombically bound electron–hole pairs. For this to happen, the

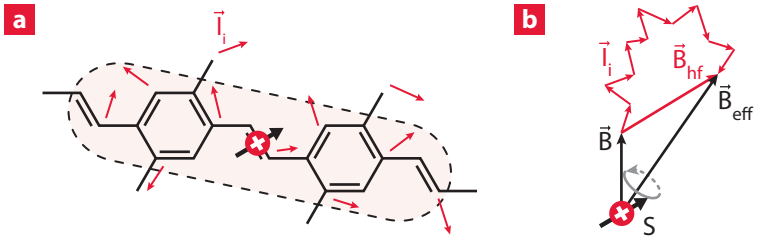

Figure 2.2 | Hyperfine fields in an organic semiconductor. a | The spin S of a polaron, located on a conjugated polymer, interacts with the nuclear magnetic moments $\vec{I}_i$ of the surrounding hydrogen atoms. **b |** In a semiclassical approximation, the hyperfine field $\vec{B}_{\mathrm{hf}}$ is the vector sum of the nuclear magnetic moments. The polaron spin then precesses around the total effective field $\vec{B}_{\mathrm{eff}}$, which is the sum of the hyperfine field and an externally applied magnetic field $\vec{B}$.

electron and hole need to approach each other even closer. When the e–h pair is so close together that their wavefunctions start to overlap, exchange interactions become important and –only then– the pair is referred to as an exciton.

Now the spin of the charges becomes important. Since the electron–hole pair consists of two spin 1/2 particles, the total spin-state of the pair can be in a singlet (total spin 0) or triplet (total spin 1) configuration. Because the injected charge carriers have a random spin, a singlet–triplet ratio of 1:3 is expected according to spin-statistics. This implies that also the singlet (S) and triplet (T) excitons are formed with this ratio. However, in the literature there is a debate about the violation of this ratio, because also more [58–60] or less [61,62] singlets are reported. Moreover, in the remainder of this section, we will show that applying a magnetic field can also change this statistical ratio.

Besides spin-dependent interactions between the charge carriers themselves, there are also interactions with the environment. Because most organic semiconductors mainly consist of low-weight atoms (such as carbon, hydrogen, nitrogen and oxygen), spin–orbit interactions are generally weak. However, the spin of the charge carriers can interact with the nuclear magnetic moments of e.g. hydrogen and nitrogen atoms. This interaction is called hyperfine interaction and is schematically depicted in Fig. 2.2. Here, the charge carrier is delocalized over a part of a polymer chain (depicted by the shaded area) and it interacts with the nuclear magnetic moments $\vec{I}_i$ of the surrounding hydrogen atoms. This interaction can be approximated by an effective magnetic hyperfine field $\vec{B}_{\mathrm{hf}}$ which is the vector sum of the nuclear magnetic moments (illustrated in Fig. 2.2b), as has been shown by Schulten and Wolynes. [63] As a result, the spin of the charge carrier starts to precess around the local hyperfine field. The magnitude of the hyperfine field is on the order of a millitesla. [64,65] The orientation is random, because every localized site is different due to disorder. [66]

We will now discuss how this random hyperfine field influences the spin state of the charge carriers. Let us therefore examine the electron–hole pair again. Once the carriers are injected into the organic semiconductor, their spins start to precess around the local hyperfine fields. Because the hyperfine field is randomly oriented at each site, the electron and hole spin of the pair will have a different precession. This leads to dephasing of the initial spin-state of the e–h pair.

If we now apply an external magnetic field, indicated in Fig. 2.2b, the spins start to precesses around the total effective field $\vec{B}_{\text{eff}}$, which is the sum of the hyperfine field and the applied magnetic field. Dephasing of the electron and hole spins within the pair will then be governed by an interplay of the random hyperfine fields and the externally applied magnetic field. At small applied fields, dephasing is an efficient process, and, as a result, the singlet and triplet spin-states are efficiently mixed, leading to deviations from the statistical 1:3 ratio. At large fields ($\vec{B} \gg \vec{B}_{\text{hf}}$), the random hyperfine fields are overruled and spin mixing is significantly reduced. Such a control of spin mixing by an externally applied magnetic field is an essential ingredient in all relevant mechanisms explaining OMAR. In the next sections, we discuss how the different mechanisms explain the changes in the current through a device.

2.3 Organic magnetoresistance

In this section, we will review the most successful mechanisms that have been proposed to explain OMAR and we ultimately aim for a unified picture. Before starting off, we note that already at an early stage it was realized that conventional mechanisms for magnetoresistance, like Lorentz-force deflection, hopping magnetoresistance or effects like weak localization are no viable candidates to explain the effect.[35,67] Alternatives were therefore needed.

To successfully develop a mechanism which describes the magnetic field effect (MFE) on the current (MC) in an organic semiconductor device, we need the answer the following questions:

(1) Which particles are of importance?
(2) Which (spin-dependent) reactions take place?
(3) How does the magnetic field influence the spin-state of the particles?
(4) How does the change in spin-state influence the current?

All contemporary mechanisms that have been proposed for OMAR, rely on spin-selective reactions between pairs of particles, where a magnetic field suppresses the spin mixing of the particle pairs prior to the reaction, thereby changing the spin fraction and the outcome. The principal question in the field is now which particle pairs and subsequent reactions are dominating the magnetic field

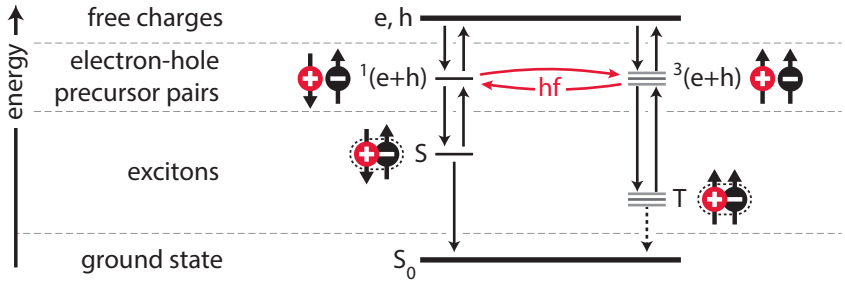

Figure 2.3 | Energy diagram of spin-dependent transitions from free charges to the ground state. Free charges can form precursor pairs in a singlet ^{1}( ) or triplet ^{3}( ) configuration. From this pair state, the precursor pair can either recombine into a singlet (S) or triplet (T) exciton or dissociate back into free carriers again. Due to hyperfine fields (hf), the singlet and triplet precursor pairs can mix. An externally applied magnetic field can suppress this mixing, giving rise to a low magnetic field effect (LFE).

effect. With respect to question (1), we can divide the possible mechanisms into three categories: (i) reactions of polarons with the same charge into bipolarons, (ii) reactions of polarons with opposite charge into excitons and (iii) reactions of triplet excitons with polarons or other excitons. We will refer to those mechanisms as bipolaron,[68] electron–hole[69], triplet–polaron[70] and triplet–triplet[71] mechanism, respectively.

In the next section we will briefly explain the different mechanisms for OMAR. In order to do so, we will make use of so-called Jabłoński diagrams.[72] An example is presented in Fig. 2.3, which shows an energy diagram of the spin-dependent transitions from free charges to the ground state. Here, free charges can form electron–hole precursor pairs in a singlet or triplet configuration. From this pair state, the precursor pair can recombine into a singlet or triplet exciton. Due to hyperfine fields, the singlet and triplet precursor pairs can mix, as described in the previous section. An external magnetic field suppresses this mixing and thereby changes the transition to the singlet and triplet exciton. Such a magnetic field effect governed by the hyperfine field strength, will be referred to as a low-field effect (LFE) in this thesis. In addition to the LFEs, so-called high-field effects (HFE) occur at field scales much larger than the local hyperfine fields. These effects will be discussed later on.

Low-field effects

Bipolaron mechanism

The first mechanism which we will discuss takes the reactions of polarons with the same charge into consideration. Within this so-called bipolaron mechanism,

as proposed by Bobbert *et al.*,[68] an external magnetic field will decrease the current by spin blocking. The bipolaron model treats the scenario where a charge carrier is quasi-stationary trapped at an energetically relatively low lying state. A nearby free carrier, which contributes to the current, has to pass this site by –at least as a temporary intermediate state– forming a doubly occupied site, the so-called bipolaron. Note that because of the large exchange interaction within the bipolaron state, its formation is spin-dependent, similar to the case of excitons. It is well possible for a pair of polarons in a singlet-configuration to form a singlet bipolaron, but very unlikely for the triplet state, because it is too high in energy.[73] Then, if the two carriers in the precursor pair are in a triplet configuration, the current is effectively blocked. At low magnetic fields, the spin blocking is lifted due to the hyperfine fields efficiently mixing the precursor spin states, as discussed in the previous section. At high fields, blocking is regained, because random hyperfine fields are now overruled, and spin character becomes well-preserved. Thus, the bipolaron mechanism gives rise to a magnetic-field dependence of the charge carrier mobility μ and leads, in this case, to a negative magnetic field effect on the current.

The bipolaron mechanism is based on the notion that the energy landscape of molecular levels in the organic semiconductor displays a Gaussian disorder, as depicted in Fig. 2.1, which can be described by an energy spread σ on the order of 0.1 eV. As introduced in Sec. 2.2, charge transport occurs via a hopping type of transport, effectively taking place along a limited number of quasi-one-dimensional percolation paths. The polaronic nature of the charge carriers gives rise to a relatively modest energy cost U to form the doubly occupied site. Because of the strong disorder, this energy is comparable to the energetic disorder ($U \sim \sigma$).[74] Monte Carlo simulations have shown that the effect on the total current through a device can become significant as a result of the quasi-one-dimensional nature of the charge transport. An intuitive 'branching' ratio b has been introduced, which controls to what extent the current is free to go around blocking sites, or how much it is forced to branch through this site. Bobbert *et al.*[68] found that the lineshape of the magnetic field effect on the current depends on b. Also, it was observed that although generally the spin blocking mechanism is dominant, a transition to the opposite effect could be obtained. The latter occurred when changing model parameters such as to optimally facilitate the formation of bipolarons. As a consequence, because of charge neutrality, this goes at the expense of the density of mobile polarons.

Recently, Harmon and Flatté introduced a model, related to the bipolaron mechanism, for magnetic field effects in positionally disordered organic materials using percolation theory.[75,76] Their model describes the effects of spin flips on hopping transport by considering the effect of spin dynamics on an effective density of hopping sites. Here, spin-flips open up spin-blocked pathways to be-

come viable conduction channels and hence produce magnetic field effects. The authors found an analytical description, and show that it is possible to observe large negative magnetic field effects on the current. The magnitude and shape of the magnetic field effects are shown to be dependent on the site density and hopping speed.

Electron–hole mechanism

Next, we will discuss a mechanism which takes the reactions of polarons with opposite charge into consideration. This is done in the so-called e–h mechanism as proposed by Prigodin *et al.*[69] Here, the crucial reaction is between weakly, coulombically bound electron–hole precursor pairs. These pairs form statistically with a ^{1}(e–h):^{3}(e–h) ratio of 1:3, as discussed Sec. 2.2. They can dissociate to form free polarons, but can also react to form an exciton from where they finally can recombine to the ground state, as depicted in Fig. 2.3. If at least one of the two reactions is spin selective, the magnetic field will control the charge balance in the device, and thereby the current. Prigodin *et al.* derived a magnetic field-dependent recombination rate, which was then linked to recombination mobility μ_r. The authors assumed a different recombination rate for singlets and triplets. So, with less mixing due to a magnetic field, there is less recombination. In the space-charge limited regime, this reduction leads to more current because of compensation of positive and negative space-charge and thus gives rise to a positive magnetic field effect on the current.[69,77]

In passing we note that generally the e–h mechanism is unlikely to produce large magnetic field effects, since it requires a competition between recombination and dissociation of precursor pairs, i.e. e–h pairs that in a single step can form an exciton. Usually, this is highly unlikely since once the electron and hole have approached each other that closely they are well within the Coulomb radius, making dissociation a very unlikely event.

Triplet–polaron mechanism

A final mechanism to be discussed takes the reactions of triplet excitons with polarons into consideration. We will refer to this mechanism as the triplet–polaron mechanism, as first proposed by Desai *et al.*[70] In their mechanism, triplet excitons can react with polarons by scattering events, which effectively reduce the mobility of the free charges and thereby decrease the current through the device. Since triplet excitons in general have a much longer lifetime than singlet excitons, their concentration can become large enough so that these reactions become significant. By applying a magnetic field, less triplet excitons are formed and thereby the current is increased, thus giving rise to a positive magnetic field effect on the current. We emphasize that even though the current

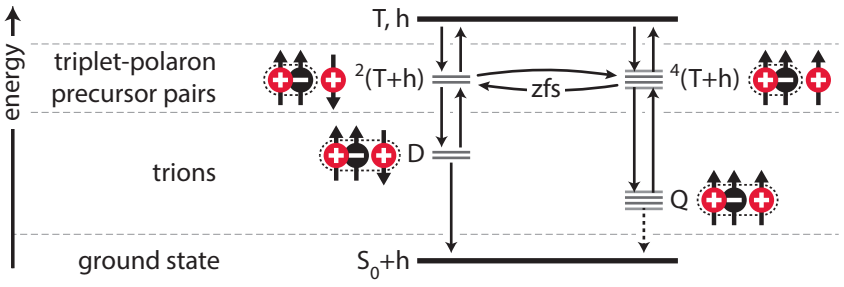

Figure 2.4 | Energy diagram of spin-dependent transitions for triplet polaron reactions to the ground state. Triplet exciton polaron pairs are created as a doublet ^{2}( ) or quartet ^{4}( ) precursor pair, whereafter they can either recombine to a doublet (D) or quartet (Q) trion or dissociate again. Here, mixing between doublet and quartet pairs is governed by the zero-field splitting (ZFS) of the triplet exciton and leads to a high magnetic field effect (HFE).

is now influenced by the reaction of triplets with polarons, the low-field effect arises from the magnetic-field dependent formation of these triplet excitons. Therefore, the hyperfine induced spin mixing of e–h precursor pairs, as indicated in Fig. 2.3, is a crucial ingredient of the triplet–polaron mechanism.

Very recently, Cox *et al.*[78] proposed an analytical model which explicitly describes the triplet–polaron mechanism. Although a full description is beyond the scope of this introducing Chapter, we will briefly highlight the main findings. In their model, spin-selective formation of so-called metastable trions from triplet exciton–polaron pairs at trap sites is used to explain the experimentally observed magnetic field effects. The low-field effect on the current is caused by the capturing of free polarons into the temporary trion state. By solving a set of elementary rate equations describing the relevant reactions, the authors derive an analytical expression which is able to correctly describe the low-field effect, the high-field effect (as discussed below) and, for the first time, the corresponding voltage dependencies. Cox *et al.* show that trap sites –and more specifically which particles occupy them– are imperative for fully understanding the experimentally observed OMAR effect.

High-field effects

Spin-dependent interactions involving triplets

Besides low-field effects, governed by the hyperfine field strength and discussed in the foregoing, high-field effects on the current, manifesting at larger magnetic field scales, can also arise due to different mechanisms. As an example, we will briefly discuss the magnetic field effect on the current due to spin-dependent triplet–polaron interactions. Here, triplet excitons can temporary capture free

charge carriers into a so-called trion state and thereby hinder the current through the device. Within this mechanism, spin mixing occurs between doublets $^2( )$ and quartets $^4( )$ of triplet exciton–polaron pairs, as indicated in Fig. 2.4. Schellekens *et al.*[79] demonstrated, using a theoretical framework discussed in Sec. 2.4, that in disordered organic semiconductors this mixing is governed by the zero-field splitting (ZFS) of the triplet excitons. As a result, the magnetic field effect manifests itself as a high-field effect at a linewidth related to the ZFS, which is on the order of 10–100 mT in most organic semiconductors.[80] The magnetic field effect arises due to the difference in lifetime of the doublet (D) and quartet (Q) trions, where the latter is expected to be much longer lived. Increasing the magnetic field decreases the mixing, resulting in less quartets which hinder the current. Thus, this mechanism yields a positive magnetic field effect on the current. Cox *et al.*[78] used the spin-selective formation of trions from triplet exciton–polaron pairs to explain the high field effect on the current.

The mutual annihilation of triplets also gives rise to a high-field effect with a linewidth determined by the ZFS.[79] However, since this triplet–triplet mechanism creates free charges, and an increasing magnetic field effectively reduces the amount of available triplets, this leads to a negative magnetic field effect on the current.

Dephasing due to different g-factors

A distinctly different high-field effect displays in the e–h mechanism. Due to the low spin–orbit interaction, the polarons in most organic semiconductors have a g-factor very close to the free electron g-factor. However, the opposite polarons in the e–h pair will generally have a (slightly) different g-factor due to a difference in localization. This difference in g leads to dephasing of the precessing electron and hole spins.[81] As a consequence, additional spin mixing occurs at large fields (typically 1 T), referred to as the Δg-mechanism. The associated HFE on the current will necessarily have a sign opposite to the corresponding LFE, which is based on the suppression of spin mixing.

Please note that in the pristine organic semiconductors as used in this thesis, the difference in electron and hole g-factor is typically only 0.03%,[82,83] making the Δg-mechanism a very unlikely candidate to produce significant magnetic field effects using moderate (up to 1T) magnetic fields. However, in certain organic materials, or when using blends of organic materials, Δg can easily be an order of magnitude larger,[84,85] resulting in measurable high-field effects on the current in this field range.

Introducing additional states

Having introduced the basic mechanisms for OMAR, we will now briefly discuss what happens in more complex systems. Until now, we only considered magnetic

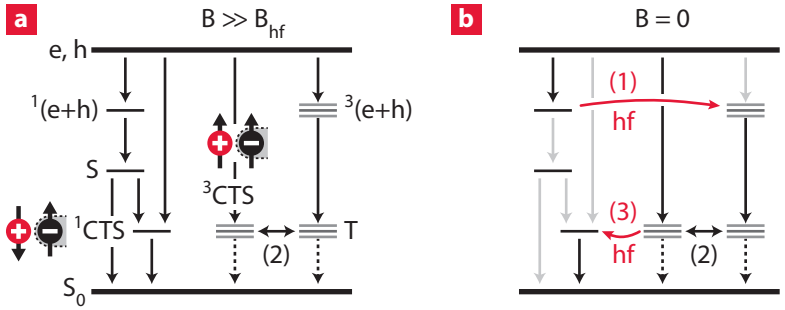

Figure 2.5 | Spin-dependent transitions for devices with additional states. The introduction of charge-transfer states (CTS) creates additional paths to the ground state. **a |** In a large applied magnetic field, the CTS can influence the triplet exciton density, indicated by process (2). **b |** In the absence of an applied magnetic field, spin mixing occurs for electron–hole pairs as well as CTS, depicted by transitions (1) and (3) respectively.

field effects in a single organic semiconductor. In this thesis we will exploit the versatility of organic materials to assess the validity of the various models for OMAR. In Chapter 5, for example, we will create devices consisting of a blend of two organic materials. The presence of the second organic material creates additional states in the energy diagram. An example is shown in Fig. 2.5. Here, so-called charge-transfer states (CTS) emerge, where the electron and hole reside on the different materials. The energetic alignment of the CTS and triplet exciton can shift for different material combinations. This system will be studied in detail in Chapters 5 and 6. Note that the introduction of the charge-transfer states creates additional paths to the ground state. Furthermore, as we will show in this thesis, these new states can significantly influence the density of other states and, moreover, enable new spin-mixing channels.

Towards a unified picture

In the foregoing, we introduced the different mechanisms as proposed for OMAR. We now continue by presenting a unified picture, which is shown in Fig. 2.6. Here, the relevant particles and their (spin-dependent) reactions are depicted as a function of energy. In all mechanisms, the magnetic field effects arise due to the spin state mixing of precursor pairs. The low magnetic field effect (LFE) originates from mixing of precursor pairs by hyperfine fields (hf). Whereas the mixing of triplet exciton–polaron pairs at the zero field splitting field scale (ZFS) leads to a high-field effect (HFE). Throughout this thesis we will use this energy diagram, or parts of it, to explain the observed magnetic

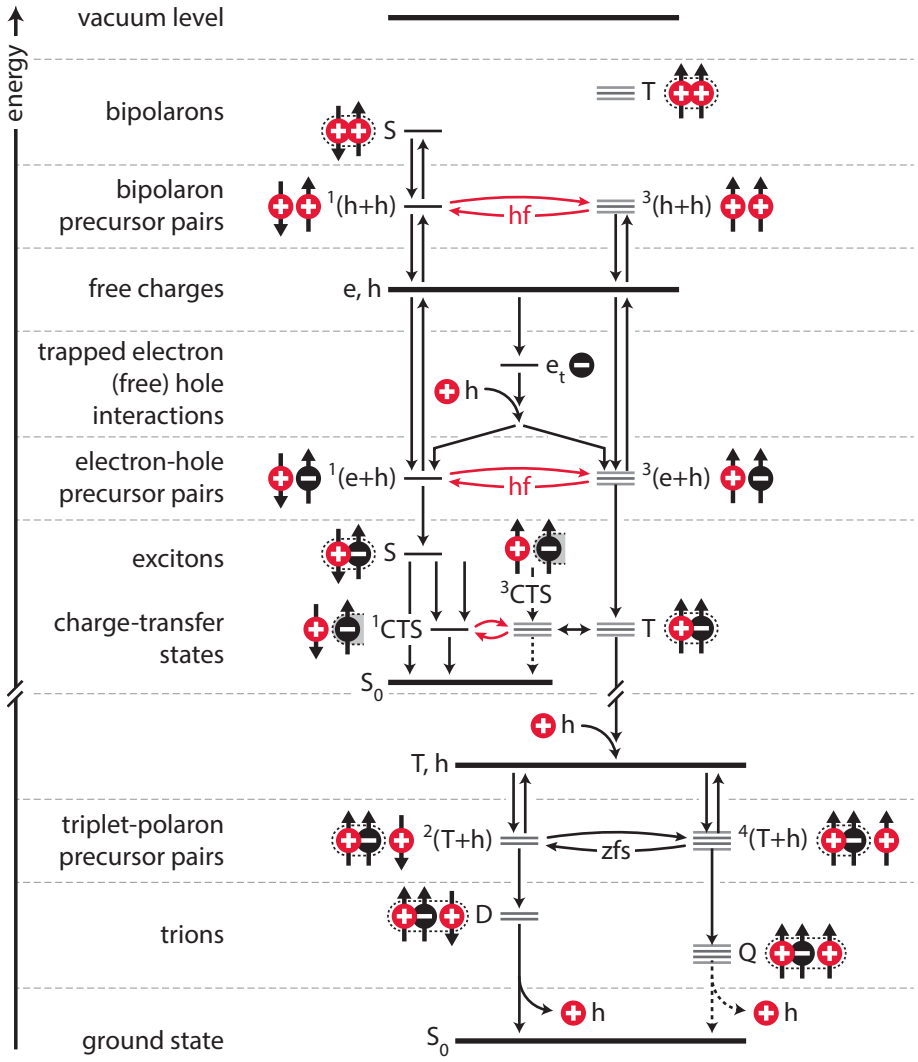

Figure 2.6 | Unified picture of relevant particles and their (spin-dependent) reactions. The magnetic field effects arise due to the spin state mixing of precursor pairs. The low magnetic field effect (LFE) originates from mixing of precursor pairs by hyperfine fields (hf). Whereas the mixing of triplet exciton–polaron pairs at the zero field splitting field scale (ZFS) leads to a high-field effect (HFE). In this overview, electrons and holes are interchangeable.

field effects. By altering energy levels we unravel the dominant mechanism in specific regimes of operation.

2.4 Modeling of organic magnetoresistance

In the last part of this Chapter, we will introduce the theoretical frameworks that have been developed to describe OMAR in a quantitative way. The first part of this section discusses microscopic modeling which enables us to calculate the magnetic field effect lineshape. The second part presents a device model, which allows us to numerically calculate how the different mechanisms influence the current through actual devices.

Microscopic models

This section presents the theoretical frameworks as used in this thesis. We do not aim for a full derivation of the models, but only briefly discuss their main characteristics. In the case of slow hopping, where the effective hopping rate is slower than the precession frequency of spins at the molecular sites, a very simple set of rate equations can be set up for a so-called two-site implementation of the bipolaron or e–h mechanism. Following Bobbert *et al.*, spin states are defined with respect to the local magnetic field direction, $\hat{h}_i$, as being parallel (P) or anti-parallel (AP).[68] Then, it can be shown that the spin-dependent rates scale with the time-averaged singlet component of the two-particle wave function, $P_{\mathrm{P/AP}} = \frac{1}{4}(1 \pm \hat{h}_1 \cdot \hat{h}_2)$, where the plus (minus) sign applies to the AP (P) orientation. Wagemans *et al.* derived for the two-site bipolaron model a generic expression for the MC in terms of $P_{\mathrm{P/AP}}$:[86]

$$\mathrm{MC}(B) - \mathrm{MC}(\infty) \propto \left\langle 1 - \frac{1}{1 + \Gamma P_{\mathrm{P}} P_{\mathrm{AP}}} \right\rangle, \tag{2.7}$$

where Γ is a line-width parameter, and $\langle \cdots \rangle$ denotes the ensemble average over $\vec{B}_1$ and $\vec{B}_2$, as resulting from the vector sum of the applied field and the randomly distributed $\vec{B}_{\mathrm{hf},i}$. It was shown that a small branching ratio ($b \ll 1$, easy to bypass blocking site) leads to a combination of a small amplitude of the MC as well as $\Gamma \ll 1$. Thus, Eq. (2.7) can be simplified to $\mathrm{MC}(B) - \mathrm{MC}(\infty) \propto \langle P_{\mathrm{P}} P_{\mathrm{AP}} \rangle$. In contrast, for a large branching ratio ($b \gg 1$), large MC and Γ are obtained, and thus the line shape is governed by a different averaging of $P_{\mathrm{P}} P_{\mathrm{AP}}$, that is $\mathrm{MC}(B) - \mathrm{MC}(\infty) \propto \langle 1/P_{\mathrm{P}} P_{\mathrm{AP}} \rangle$. In Chapter 3, we will show that we are able to describe both results using a single empirical lineshape. We emphasize that, although in this original work focus was entirely on the bipolaron mechanism, the e–h mechanism yields similar results. More specifically, the two mechanisms produce identical lineshapes when allowing for arbitrary tuning of certain parameters.

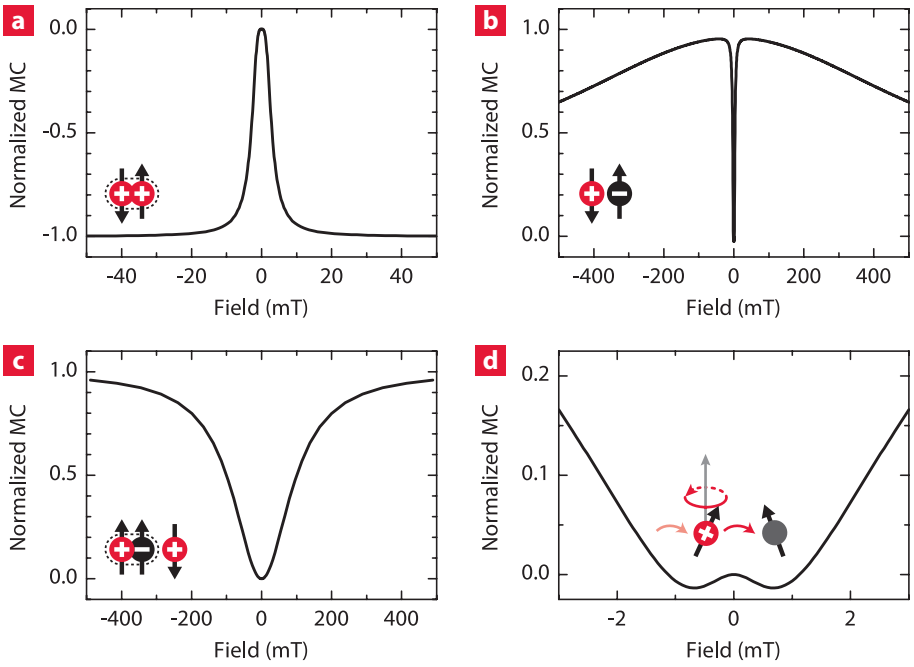

Figure 2.7 | Microscopic calculations using the stochastic Liouville approach. Calculations for **a |** the bipolaron mechanism, **b |** the e–h mechanism and **c |** the triplet–polaron mechanism. **d |** Under certain conditions, magnetic field effects at ultra-small field scales can be observed. Please refer to Appendix 2.A (Table 2.1) for an overview of the calculation parameters.

Treating more complicated cases, including interactions between the spins within the pair (such as dipolar or exchange), or magnetic field effects in the fast-hopping regime, the simple methodology introduced in the preceding paragraph no longer suffices. Schellekens *et al.* demonstrated that a density matrix formalism for open quantum systems provides an elegant and very powerful platform for calculating the magnetic field effects in such nontrivial cases.[79] For the equation of motion of the density matrix $\boldsymbol{\rho}$ (describing the coherent admixture of spin states), the stochastic Liouville equation was used, which in steady-state reads:

$$\frac{d\boldsymbol{\rho}}{dt} = -\frac{1}{\hbar}\left[\mathbf{H}(t), \boldsymbol{\rho}(t)\right] - \frac{1}{2}\left\{\boldsymbol{\Lambda}, \boldsymbol{\rho}(t)\right\} + \boldsymbol{\Gamma} = 0. \tag{2.8}$$

The first term is the Liouville term describing the evolution of the density matrix under the influence of the Hamiltonian of the system $\mathbf{H}$, where the square brackets denote the commutator. The second term is a sink term that spin-selectively removes particles from the system, where $\boldsymbol{\Lambda}$ is the operator that

projects on the corresponding spin subspace and the curly brackets denote the anti-commutator. The last term $\mathbf{\Gamma}$ is a source term, which adds particles to the system. We emphasize that in the slow-hopping regime, when restricting ourselves to the two-particle case of the bipolaron or e–h mechanism, and neglecting interactions between the two spins, the approach becomes identical to the simple rate equations that led to Eq. (2.7).

As an example of its potential, but without going into the details of the calculations, Fig. 2.7 shows an overview of calculations using stochastic Liouville equation. Figures 2.7a and b show the magnetic field effect lineshape for the bipolaron and e–h mechanism respectively. In both cases, the low-field linewidths are determined by the hyperfine field. In Fig. 2.7b we imposed a difference in g-factor for the electron and hole, resulting in a negative high-field effect. In contrast, the high-field effect as a result of spin-dependent triplet polaron interactions is shown in Fig. 2.7c. Here, the linewidth is governed by the zero-field splitting of the triplet excitons.

Furthermore, the calculations also allow us to observe magnetic field effects at ultra-small fields (USFE). An example is shown in Fig. 2.7d. This distinctive feature, which has also been observed experimentally recently,[87,88] can be explained by a competition between the hopping rates of the charge carrier and its precession frequency around the effective magnetic field.[89] At ultra-small fields ($B < B_{\mathrm{hf}}$), increasing the externally applied magnetic field first leads to a small increase in spin-mixing due to an increase in precession frequency. Eventually, when further increasing the magnetic field ($B \gg B_{\mathrm{hf}}$), the spin-mixing reduces again due to the suppression of the hyperfine field effects as discussed in Sec. 2.2. We will also adress this magnetic field effect in more detail in Chapter 3.

Device models

It should be noted that the relation between the microscopic mechanisms and the way they affect the magnetic field effect on the current on a device level, have been found to be particularly nontrivial. As a consequence, extreme care should be taken in properly accounting for the device physics when considering the magnitude and sign of the magnetic field effect. Therefore, after having discussed a methodology for calculating the magnetic field effect lineshape microscopically, we will now briefly introduce the device physics model for OMAR as used throughout this thesis.

In this device model,[90–93] we calculate how the injected charge carriers pass through the device under the influence of drift and diffusion. Drift results from charge carriers moving under the influence of an electric field, while the diffusive current is a result of carriers moving due to a charge concentration

gradient. The electron (hole) current density $J_{n(p)}$ is the sum of the drift and diffusion contributions and can be described as:

$$\begin{aligned} J_n &= q\mu_n n\nabla\varphi + qD_n\nabla n \\ J_p &= q\mu_p p\nabla\varphi - qD_p\nabla p, \end{aligned} \tag{2.9}$$

where the electron (hole) density is given by $n(p)$ and $D_{n(p)}$ and the diffusion constant by $D_{n(p)} = k_\mathrm{B}T/q\mu_{n(p)}$. Furthermore we have to solve the continuity equation:

$$\begin{aligned} \frac{\partial n}{\partial t} &= \frac{1}{q}\nabla J_n - r\gamma np \\ \frac{\partial p}{\partial t} &= -\frac{1}{q}\nabla J_p - r\gamma np \end{aligned} \tag{2.10}$$

and Poisson's equation:

$$\epsilon\nabla^2 = q(n-p). \tag{2.11}$$

In order to obtain a unique solution to this system of coupled differential equations, one needs to define the boundary conditions for carrier densities and potential at the contacts. [94,95]

To model the magnetic field effects on the current in the device simulations, we assign the different mechanisms as proposed in Sec. 2.3 to certain device parameters. In the case of the bipolaron mechanism, the magnetic-field dependent spin blocking is modeled as a reduction in charge carrier mobility. Normally, the magnetoconductance (MC) is calculated as the change in current I due to the magnetic field B using:

$$\mathrm{MC} = \frac{I(B) - I_0}{I} = \frac{\Delta I}{I}, \tag{2.12}$$

with I_0 the current at $B = 0$. Here, we calculate the normalized magnetocurrent (NMC) as:

$$\mathrm{NMC}_{n(p)} = \frac{\Delta I}{I}\frac{\mu_{n(p)}}{\Delta\mu_{n(p)}}, \tag{2.13}$$

where ΔI is the change in current due to the change in mobility $\Delta\mu_{n(p)}$.

In the case of the e–h mechanism, the magnetic field effectively reduces the recombination in the device. This is can be simulated straightforwardly in the device model by reducing the recombination prefactor r, resulting in a total change of the recombination mobility $\mu_\mathrm{r} = r(\mu_\mathrm{e} + \mu_\mathrm{h})$. The NMC can then be calculated as:

$$\mathrm{NMC}_r = \frac{\Delta I}{I}\frac{\mu_r}{\Delta\mu_r} = \frac{\Delta I}{I}\frac{r}{\Delta r}. \tag{2.14}$$

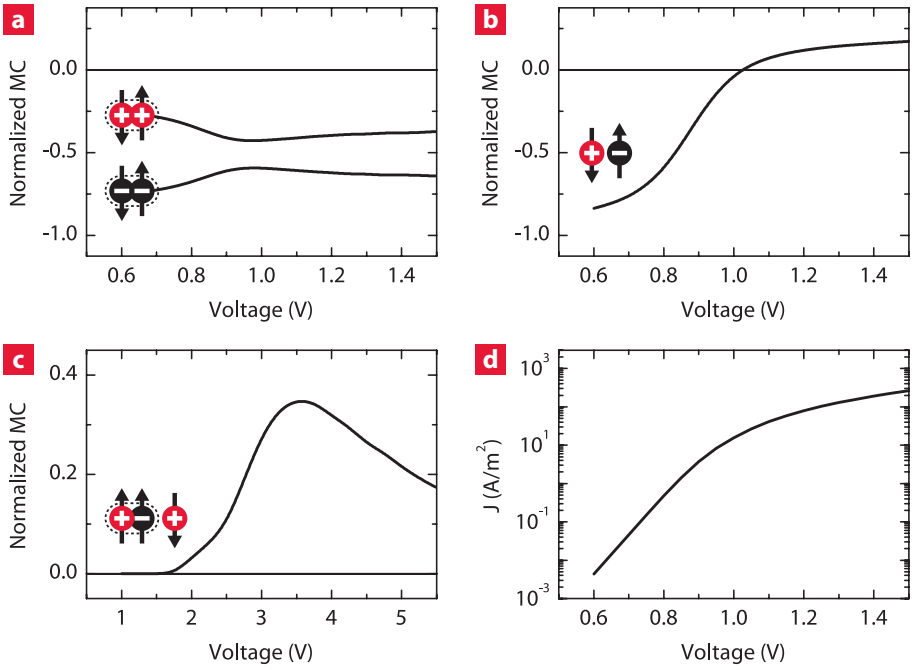

Figure 2.8 | Magnetic field effects as a function of voltage simulated using a device model. Simulations for **a |** the bipolaron mechanism, **b |** the e–h mechanism and **c |** the triplet–polaron mechanism. **d |** A typical current density as a function of voltage obtained from the simulations. Please refer to Appendix 2.A (Table 2.2) for an overview of the calculation parameters.

Very recently, Cox *et al.*[95] have extended the device model to also describe the triplet–polaron mechanism. Therefore, they incorporated the continuity equations of the triplet exciton and trion density into the device model. The excitons are created from electron–hole recombination and the trions from triplet exciton–polaron reactions, as described in Sec. 2.3. Also Poison's equation has been adjusted accordingly. The magnetic field effect on the current is calculated by assuming a reduction in the formation of triplet excitons ΔP_T. Then, the NMC of the triplet–polaron mechanism is given by:

$$\mathrm{NMC_{TP}} = \frac{\Delta I}{I}\frac{1}{\Delta P_T}. \tag{2.15}$$

Finally, as an example of its unique potential, but without going into the details of the calculations, Fig. 2.8 shows an overview of calculations using the device model. Here, we calculated the magnetic field effects as a function of voltage for the different mechanisms. We observe distinctly different voltage dependencies for the three mechanisms.

In the case of the bipolaron mechanism (Fig. 2.8a), we observe a negative, hardly voltage dependent MC due to spin blocking. We can explain differences in magnetic field effect magnitude with a difference in charge carrier mobility. The voltage dependence of the e–h mechanism (Fig. 2.8b), shows a distinctively different voltage dependence. Intriguingly, we observe a sign change in the magnetic field effect while simulating only a single mechanism. This sign change occurs at the transition from the diffusion to drift dominated regime and will be discussed in more detail in Chapter 5. Lastly, for the triplet–polaron based mechanism (Fig. 2.8c), we observe a peaked behavior of the voltage dependence. Using the trion model, as proposed by Cox *et al.* [78] we can intuitively explain this shape. The initial increase simply stems from the increase of the triplet density with voltage, while the eventual decrease arises from the fact that there is only a limited number of traps available in a device. In Chapter 4, we will show that we can also explain the temperature dependence of the MC(V)-curves using this model.

We emphasize that these specific fingerprints, combined with the the calculations of the magnetic field effect lineshapes as presented in the previous section, will prove invaluable in identifying the dominant mechanisms for OMAR and will therefore be used throughout this thesis.

2.5 Conclusion

In conclusion, in this Chapter we have presented the current perspectives on organic magnetoresistance. The contemporary mechanisms that have been proposed for OMAR have been introduced and their differences and similarities have been discussed. Furthermore, we presented a unified picture of the different mechanisms, which will serve as a basis for the rest of this thesis. Finally, we introduced the theoretical frameworks that have been developed to describe OMAR in a quantitative way. Using this framework, we are able to relate changes in the measured OMAR lineshapes and voltage dependencies to microscopic and device parameters in the rest of this thesis.

Appendix 2.A Modeling parameters

The theoretical frameworks that have been presented in Sec. 2.4 can be used to describe OMAR in a quantitative way. The microscopic modeling enables us to calculate the magnetic field effect lineshape, whereas the device modeling allows us to numerically calculate how the different mechanisms influence the current through an actual device.

To calculate the magnetic field effects using the microscopic model, we need to specify the rate-constants of the system (indicated by the arrows in

Figs. 2.3–2.6). The parameters used to calculate the magnetic field effects for the different mechanisms as shown in Fig. 2.7 are listed in Table 2.1. To calculate the magnetic field effects using the device model, we need to specify certain device parameters of the system. Table 2.2 gives an overview of the parameters used to calculate the magnetic field effects for the different mechanisms as shown in Fig. 2.8.

In the case of triplet–polaron interactions, the following additional parameters are used: the number of electron trap sites N_t (2×10^{-4} /nm^{-3}), the electron trapping coefficient γ_t (2×10^{8} nm^3/s), the hole recombination coefficient with trapped electrons γ_r (1×10^{8} nm^3/s), the triplet exciton lifetime t_T (6×10^{-5} s), the triplet–polaron interaction coefficient γ_{TP} (1×10^{9} nm^3/s) and the triplet–polaron pair lifetime t_{TP} (1×10^{-3} s).

Table 2.1 | Parameters as used in the microscopic calculations. The calculations in the slow-hopping limit for **a |** the bipolaron mechanism, **b |** the e–h mechanism and **c |** the triplet–polaron mechanism. **d |** Calculations in the intermediate-hopping regime for the e–h pair model. Figure 2.7 show the corresponding lineshapes. Please refer to Ref. [79] for more details on the calculations, and to Chapter 4 (Figs. 4.1 and 4.8) for more information on the rates.

a. bipolaron	**b.** e–h pair	**c.** triplet–polaron	**d.** e–h pair
$r_{\alpha\beta} = 100\,\mathrm{s}^{-1}$	$q = 1\,\mathrm{s}^{-1}$	$\mathrm{r} = 1\,\mathrm{s}^{-1}$	$q = 10^{7.75}\,\mathrm{s}^{-1}$
$r_{\alpha\varepsilon} = 1\,\mathrm{s}^{-1}$	$q_S = q_T = q$	$r_D = r_Q = r$	$q_S = q_T = q$
$r_{\varepsilon\alpha} = 1\,\mathrm{s}^{-1}$	$k_S = 10\,\mathrm{s}^{-1}$	$k_D = 1\,\mathrm{s}^{-1}$	$k_S = 10^{8.75}\,\mathrm{s}^{-1}$
$B_{\mathrm{hf}} = 1\,\mathrm{mT}$	$k_T = 1\,\mathrm{s}^{-1}$	$k_Q \to \infty$	$k_T = 10^{7.75}\,\mathrm{s}^{-1}$
	$B_{\mathrm{hf}} = 1\,\mathrm{mT}$	$B_{\mathrm{hf}} = 1\,\mathrm{mT}$	$B_{\mathrm{hf}} = 1\,\mathrm{mT}$
	$\Delta g = 0.5\%$	$D_{\mathrm{ZFS}} = 100\,\mathrm{mT}$	
	$d = 2B_{\mathrm{hf}}$	$E_{\mathrm{ZFS}} = 0\,\mathrm{mT}$	

Table 2.2 | Parameters used in the drift-diffusion simulations. For all devices, the workfunctions of the contacts are set to give rise to ohmic electron and hole injection. The calculations are performed for **a |** the bipolaron mechanism, **b |** the e–h mechanism and **c |** the triplet–polaron mechanism. Please refer to Ref. [95] and Chapter 5 (Appendix 5.B) for more details on the simulations.

	a. bipolaron	**b.** e–h pair	**c.** triplet–polaron
	$\Delta\mu_{n(p)}$	$\Delta\mu_r$	ΔP_T
μ_{p} (m^2/Vs)	8×10^{-9}	8×10^{-9}	1×10^{-10}
μ_{n} (m^2/Vs)	2×10^{-9}	2×10^{-9}	2×10^{-9}
ε_{r}	3.6	3.6	3.0
g_0 (nm^{-3})	0.3	0.3	0.3
HOMO (eV)	5.2	5.2	5.2
LUMO (eV)	4.1	4.1	2.4

3

Unraveling the magnetic field effect lineshape

A surprisingly large organic magnetoresistance (OMAR) has been found in both polymers and small molecule organic semiconductors at relatively small applied magnetic fields and at room temperature. In all models proposed for OMAR, spin dephasing due to hyperfine fields plays an essential role. The characteristic magnetic-field dependence is generally fitted with either a Lorentzian or a so-called non-Lorentzian function. The shape is determined by both the hyperfine fields and an additional broadening due to microscopic mechanisms, as described in the models. In this Chapter, a new empirical function is introduced that captures the two effects separately, and converges to the earlier introduced lineshapes in specific limits. Recently it has been demonstrated that an additional feature can be observed at ultra-small magnetic fields. This effect can be easily incorporated in our empirical approach by explicitly treating the limit in which hopping of carriers is no longer slow compared to spin precession in the hyperfine fields. Our approach is used to analyze several theoretical and experimental results. It is shown that experimentally observed trends can be well understood, and important parameters can be obtained from experimental data without prior knowledge about which model applies.[*]

[*] Published as part of: *The many faces of organic magnetoresistance.* W. Wagemans, P. Janssen, A.J. Schellekens, F.L. Bloom, P.A. Bobbert, and B. Koopmans, SPIN **1**, 93 (2011).

3.1 Introduction

Organic spintronics aims at exploiting the spin degree of freedom in organic semiconductor-based electronics. One class of activities is aiming at the realization and exploitation of spin injection devices, in which a spin polarized current is injected from a ferromagnetic electrode into an organic medium. That work is inspired by the long spin coherence times in organic semiconductors (OSC) consisting of low mass elements and thereby having weak spin–orbit interactions.[30,36,38,96–101] Another class of activities has been triggered by the observation of a considerable organic magnetoresistance (OMAR) in organic light-emitting diodes, or similar devices that use a wide variety of OSCs. The possibility to obtain a large magnetoresistance at room temperature, applying only small magnetic fields (several milliteslas), and without using any ferromagnetic electrodes has attracted much attention.[35,68,69,87,102–106] The effect seems promising for applications and also allows for new insights into the electrical transport in organic semiconductors. In this Chapter we will introduce a novel empirical approach to gain more insight in the underlying physical effects.

Experimentally, the OMAR traces –described as a change in current with magnetic field– show many faces. Both positive and negative effects have been observed and also the magnetic field scales can vary over orders of magnitude. In our work we show that, even though different mechanisms are responsible for OMAR, they can all be captured in a universal empirical function. The general consensus within the field is that the low-field effects (LFE, typical field scale of 1–10 mT), are due to an interplay between the applied magnetic field and the random hyperfine fields in the material resulting from the surrounding hydrogen nuclei.[68,69,103,107] At small applied magnetic fields, the random hyperfine fields B_{hf} experienced by charge carriers (polarons) at different molecular sites cause an efficient channel for spin decoherence. This leads to a rapid change of singlet (S) and triplet (T) character of carrier precursor pairs. At applied fields much larger than B_{hf} the precession of spins on different sites gets more coherent, and S and T character will be preserved for a (much) longer time.

As to the line shape of the LFE, it has been shown that the magnetoconductance versus magnetic field MC(B) curves have a characteristic shape. They can be fitted well with either a Lorentzian function,

$$\mathrm{MC}(B) \propto B^2/(B_0^2 + B^2), \tag{3.1}$$

or an empirical non-Lorentzian function,[35]

$$\mathrm{MC}(B) \propto B^2/(B_0 + |B|)^2. \tag{3.2}$$

Both functions have a similar width, characterized by the parameter B_0 that is typically 3–6 mT,[35] where B_0 is believed to be related to the magnitude of the hyperfine fields.

As introduced in the foregoing, in contemporary models for OMAR mixing of the spin states of charge pairs by precession in local random hyperfine fields plays a crucial role. The shape of the MC(B) curves originates from the suppression by the external magnetic field of this hyperfine-field induced mixing. The shape, or width, of the curves is, however, not only determined by the magnitude of the hyperfine fields. From the bipolaron model, it is known that –even with the same hyperfine fields– additional broadening occurs through the interactions in the model.[68,86] This additional, hyperfine-field independent, broadening also affects the value of B_0 obtained with either fitting function. The broadening, caused by the microscopic details of the model, is not unique to the bipolaron model. A similar type of additional broadening will also occur in the electron–hole pair model,[69] because this model can be treated in an equivalent way.[108]

Moreover, the models show that a smooth transition occurs from a narrow Lorentzian to a broader non-Lorentzian.[68] Curves falling in such a transition regime cannot be fitted well by either of the two functions. Therefore, a fitting function is needed that replaces the two empirical fitting functions and is capable of describing the transition regime, and that includes the theoretical observation that the shape of the curves is both determined by the hyperfine fields and by an additional broadening. Such an approach is presented in the present Chapter.

A clear difference between the Lorentzian and the non-Lorentzian curves is the way they converge to their high-field value MC_∞. This can be seen by calculating $1 - MC(B)/MC_\infty$, which converges as $1/B^2$ for the Lorentzian and as $1/B$ for the non-Lorentzian. The exact power of the convergence is difficult to check experimentally, as MC_∞ is usually not well defined due to the limited measuring range and large-field effects possibly playing a role as well.[109] In spite of these limitations, the majority of the reported experimental curves can be much better fitted with the non-Lorentzian function than with the Lorentzian. Nevertheless, systematic differences between the measured line shapes and the non-Lorentzian described by Eq. (3.2) occur, and we will show that experiments are significantly better described by our new approach.

More recently other deviations from the empirical lineshapes of Eqs. (3.1,3.2) have been discovered. It was found that in the (sub)mT-range a so-called ultra-small-field effect (USFE) can be observed, producing a tiny dip in the MC(B) curve.[87,88] In this Chapter, we also discuss progress in understanding this specific new feature, and show how it can be incorporated in a natural way in our empirical procedure.

Summarizing, in this Chapter we will introduce an alternative empirical function for analyzing the experimental MC(B) curves. This function separately includes the magnitude of the hyperfine fields and the effect of the model. Thereby, we can extract these parameters independently when fitting various

theoretical and experimental data sets. In the next section the new fitting function will be introduced and thereafter it will be applied to a series of recent experimental and numerical data sets.

3.2 Empirical lineshapes

Inspired by the similarity of the various models discussed in Sec. 2.3, but aiming at a generic, model-independent function that is capable of describing line shapes in different regimes, we propose an empirical approach. We emphasize that the function we propose cannot be derived analytically, neither is its choice completely unambiguous. Yet it can be shown to be a simple (if not simplest) realization of a function that fulfills a specific (but sensible) set of requirements. Moreover, we will show that the specific function reproduces MC traces in various test cases, both from numerical modeling and experiments, and the physical parameters correctly represent the underlying physics. Therefore we expect this new fitting function to provide a particularly useful tool for all researchers in the field of OMAR.

Requirements for the empirical lineshape

Throughout this section, focus will be on the so-called low magnetic field effects (LFEs) as introduced in the introduction. We will start by assuming the slow-hopping regime, and are searching a function $F(B)$, related to the MC according to:

$$\mathrm{MC}(B) = \mathrm{MC}_\infty[1 - F(B)], \tag{3.3}$$

where MC_∞ is the MC at large applied magnetic field. Furthermore we assume that the dependence of F on B can be fully specified through an effective field, $B_{\mathrm{eff}}(B)$, that converges to a somehow averaged local hyperfine field, $B_{\mathrm{eff}} = B_{\mathrm{hf}}$, for $B = 0$, while it approaches $B_{\mathrm{eff}} = B$ for $B \gg B_{\mathrm{hf}}$.

In order to make this relation more explicit, we plotted the average magnitude of the vector sum of the hyperfine field and the external field, averaged over different distributions of hyperfine fields in Fig. 3.1a. The two examples shown correspond to the average over a three-dimensional Gaussian distribution of hyperfine fields (characterized by a standard deviation of $|\vec{B}_{\mathrm{hf}}|$ equal to σ_{hf}), and the average over a randomly oriented hyperfine field (defined to have a fixed magnitude σ_{hf}). It is found that both can be parameterized well with:

$$B_{\mathrm{eff}} = (B_{\mathrm{hf}}^n + |B|^n)^{1/n}, \tag{3.4}$$

which gives the best fit for $n = 2.2$ ($B_{\mathrm{hf}} = \frac{2\sqrt{2}}{3}\sigma_{\mathrm{hf}} \approx 0.94\,\sigma_{\mathrm{hf}}$) and $n \approx 2.7$ ($B_{\mathrm{hf}} = \sigma_{\mathrm{hf}}$), for the Gaussian and fixed-magnitude average, respectively (depicted

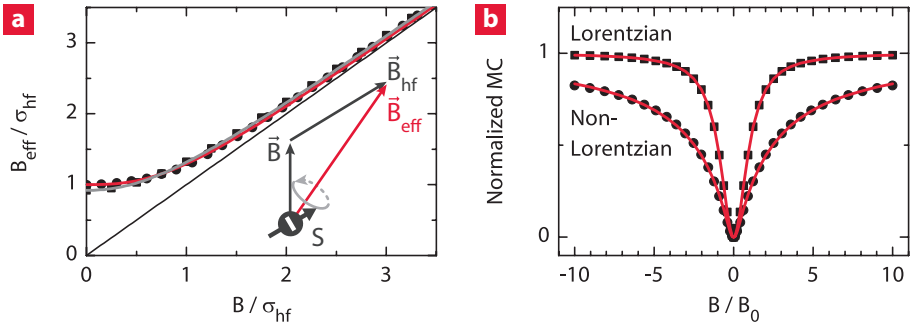

Figure 3.1 | Requirements for the empirical lineshape. a | Magnitude of the effective magnetic field B_{eff} calculated using an average over a three dimensional Gaussian distribution of hyperfine fields (squares), and the average over a randomly oriented hyperfine field with a fixed magnitude (circles). The solid lines are a fit to Eq. (3.4), with $n = 2.2$ and $n \approx 2.7$ respectively. **b |** Fits with Eq. (3.5) (lines) of a Lorentzian ($B_{\mathrm{m}} = 0$, $B_{\mathrm{hf}} = B_0$ and $n = 2$) and non-Lorentzian curve ($B_{\mathrm{m}} \approx 10B_0$, $B_{\mathrm{hf}} \approx 0.22B_0$ and $n \approx 2.7$).

by the squares and circles in Fig. 3.1a). Later in this section, we will show that we can determine n from microscopic simulations.

Next we specify the sensible set of requirements for $F(B)$:

1. $F(B)$ is normalized according to $F(0) = 1$ and $F(\pm\infty) = 0$.
2. The dependence of F on B is through B_{eff} defined in Eq. 3.4, i.e. $F(B) = F[B_{\mathrm{eff}}(B)]$.
3. The width of $F(B)$ is fully specified through the effective field in Eq. (3.4), and a single additional model parameter B_{m}.
4. $F(B)$ converges to a curve that resembles the Lorentzian-like lineshape for $B_{\mathrm{m}} = 0$, while it approaches the non-Lorentzian-like line shape for $B_{\mathrm{m}} \to \infty$. More specifically, the convergence of $F(B)$ for $B \to \infty$ goes like $1/B^2$ and $1/B$, respectively.
5. In order to make this dependency of the shape on B_{m} unambiguous, we require that the half-width at half maximum (HWHM) of $F(B)$ corresponds to $B_{\mathrm{eff},1/2} = B_{\mathrm{eff},1/2}|_{B_{\mathrm{m}}=0} + B_{\mathrm{m}}$, i.e., B_{m} can be interpreted as the additional broadening compared to the Lorentzian line shape.

As a trial function to match all these requirements, we propose:

$$F(B) = \frac{C}{1 + c_1(B_{\mathrm{eff}}/B_{\mathrm{m}}) + c_2(B_{\mathrm{eff}}/B_{\mathrm{m}})^2}, \tag{3.5}$$

where $C = 1 + c_1(B_{\mathrm{hf}}/B_{\mathrm{m}}) + c_2(B_{\mathrm{hf}}/B_{\mathrm{m}})^2$, just to normalize the function at $B = 0$. The constants c_1 and c_2 depend only on B_{m}, and are yet to be determined. Using $c_1 = 1$, and using c_2 such that it is neither vanishing for $B_{\mathrm{m}} = 0$ nor

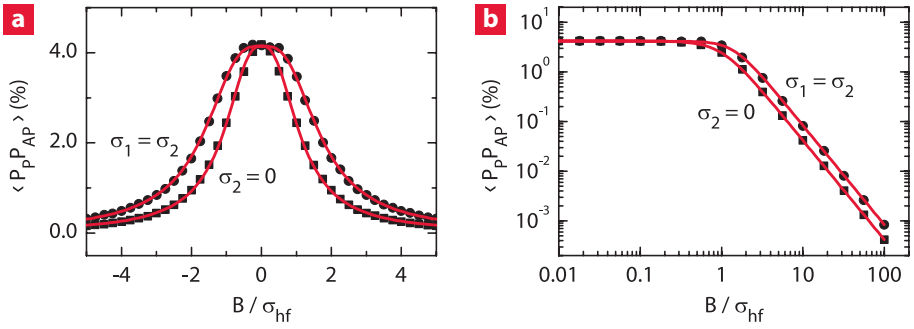

Figure 3.2 | Microscopic calculations fitted using the empirical lineshape. Normalized magnetoconductance as a function of the normalized magnetic field for a numerical integration of Eq. (2.7) over random hyperfine fields. **a |** Calculations of $\langle P_P P_{AP} \rangle$ using a random hyperfine field only present on one of the two sites (squares) and on both sites (circles). **b |** The same calculation, but for a much larger field range. The solid lines are a fit using $B_m = 0$, but for different values of $n \approx 2.5$ ($B_{hf} = \sigma_{hf}$) and $n \approx 3.1$ ($B_{hf} = \sqrt{2}\sigma_{hf}$), respectively.

diverging for $B_m \to \infty$, it can be easily seen that requirements 1 through 4 are fulfilled. Finally, in order to meet requirement 5, and fixing $c_1 = 1$, one finds $c_2 = (2 - \sqrt{2})/(2\sqrt{2} + B_m/B_{eff})$. Note that the function thus derived has a HWHM of $B_{eff,1/2} = \sqrt{2}B_{hf}$ for $B_m = 0$, and $B_{eff,1/2} \approx \sqrt{2}B_{hf} + B_m$ for $B_m > 0$. Please note that although B_m has been introduced as a separate parameter, in experiments where B_{hf} is being changed, e.g. by deuteration, one would expect that B_m scales linearly with B_{hf}.

As specified, Equation (3.5) can generate curves that are in good agreement with both Lorentzian and non-Lorentzian curves, reproducing both the fast and slow saturation. This is shown in Fig. 3.1b where a Lorentzian and non-Lorentzian curve are fitted with Eq. (3.5) (lines). For large B_m/B_{hf} a non-Lorentzian-like curve is found. For these curves, $1 - \mathrm{MC}(B)/\mathrm{MC}_\infty$ converges as $1/B$ for $B \to \infty$, as is characteristic for the non-Lorentzian. For $B_m \to 0$, a narrow curve is found, which exactly resembles a Lorentzian in the case $n = 2$, as shown.

The function $F(B)$ has some specifically interesting properties. Of particular importance is that, although for $B_m/B_{hf} \gg 1$ the HWHM is entirely determined by B_m, the rounding near zero field is still a function of both B_{hf} and B_m. More specifically, it can be derived that the curvature near $B = 0$ is determined by $F(B) \approx 1 - (B/B_m)(B/B_{hf})^{n-1}$. In line with this behavior, as a function of increasing B_m, lineshapes are broadening, but the relative curvature around zero field increases. Thereby, by measuring MC lineshapes both at large field ($B > B_m$), as well as accurately near zero ($B \ll B_{hf}$), it should be possible to derive B_m and B_{hf} separately from a single experiment. In passing, we note that

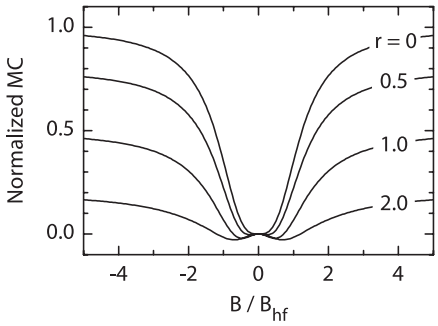

Figure 3.3 | The empirical lineshape in the intermediate hopping regime. Normalized magnetoconductance as a function of the normalized magnetic field calculated with Eq. (3.7) using different values for r.

in the pure non-Lorentzian as formerly proposed, the broadening of the entire curve is governed by a single parameter B_0. We will show in the next section that such a uniform scaling fits less well to experimental observations, and thereby it misses an essential part of the physics!

To determine the value of n (and the corresponding B_{hf}) from Eq. (3.4), we have calculated the MC(B) for the two-site bipolaron model in terms of $P_{\mathrm{P/AP}}$ by a numerical integration of Eq. (2.7) over random hyperfine fields. Figure 3.2 shows calculations of $\langle P_P P_{AP} \rangle$ using a situation where a random hyperfine field is only present on one of the two sites, as well as a situation where identical Gaussian distributions are present at both sites. It is found that both curves can be fitted extremely well by our model function using $B_{\mathrm{m}} = 0$, but for different values of $n = 2.54 \pm 0.04$ ($B_{\mathrm{hf}} = \sigma_{\mathrm{hf}}$) and $n = 3.07 \pm 0.06$ ($B_{\mathrm{hf}} = \sqrt{2}\sigma_{\mathrm{hf}}$), respectively. The fact that the different values of n are obtained, just reflects its dependence on the exact way averaging is being performed. In the situation where a random hyperfine field is only present on one of the two sites, we find that the hyperfine field as extracted from the fit, is equal to the standard deviation of the random hyperfine field as used in the calculation ($B_{\mathrm{hf}} = \sigma_{\mathrm{hf}}$). However, in the situation where identical Gaussian distributions are present at both sites, we find $B_{\mathrm{hf}} = \sqrt{2}\sigma_{\mathrm{hf}}$. Throughout the rest of this Chapter we will merely address the symmetric case of equal hyperfine distributions at different molecular sites, and thereby fix the value $n = 3.1$ (and $B_{\mathrm{hf}} = \sqrt{2}\sigma_{\mathrm{hf}}$ correspondingly) in the expression for B_{eff} when using Eq. (3.5).

Including the intermediate-hopping regime

A final refinement of the generic lineshape is that of including the fast-hopping regime, i.e. when $r = \omega_{\mathrm{hop}}/\omega_{\mathrm{hf}}$ is no longer small with respect to unity. As

explained in the previous section, in that case only a partial dephasing of the spin state of the carriers may occur before a hopping event takes place. We will treat such a partial spin dephasing by hyperfine fields in a simple model. We assume a single precession frequency ω_{prec}, and a statistical distribution of waiting times, $\exp(-\omega_{\mathrm{hop}}t)$, with an average $1/\omega_{\mathrm{hop}}$, before a hopping event takes place. Doing so, one can derive an average dephasing factor:

$$\begin{aligned} D(B) &= 1 - \int_0^\infty \omega_{\mathrm{hop}} \exp\left(-\omega_{\mathrm{hop}}t\right) \cos\left(tB_{\mathrm{eff}}/B_{\mathrm{hf}}\right) \mathrm{d}t \\ &= 1 - \frac{1}{1 + (B_{\mathrm{eff}}/rB_{\mathrm{hf}})^2}, \end{aligned} \tag{3.6}$$

which converges to $D(B) = 1$ in the slow-hopping limit ($r \ll 1$). We note that in this case the dephasing is a process that occurs due to the difference of the hyperfine fields at both sites, and therefore determined by $(\vec{B}_{\mathrm{hf},i} - \vec{B}_{\mathrm{hf},j}) + \vec{B}$ for pairs of carriers at site i and j. Calculating the corresponding effective field for identical Gaussian distributions at both sites yields a result that again matches Eq. (3.4), but now with a best fit for $n \approx 2.3$, and $B_{\mathrm{hf}}/\sigma_{\mathrm{hf}} \approx 1.2$ (not shown). Please note that averaging a different observable over the same hyperfine field distribution yields a *different* optimal value for n, as could have been expected. Thus we will be using the latter result ($n = 2.3$) in the expression for B_{eff} whenever applying the dephasing factor of Eq. (3.6). The final expression for the MC now reads:

$$\mathrm{MC}(B) = \mathrm{MC}_\infty D(B)[1 - F(B)]. \tag{3.7}$$

Normalized this way, MC_∞ is defined as the maximum MC that would be achievable within the slow-hopping regime; for fast-hoppingFast hopping $\mathrm{MC}(\infty)$ will be less than MC_∞. Traces for different values of r according to Eq. (3.7) are plotted in Fig. 3.3. An USFE is nicely developing once r becomes of the order of unity. In passing we note that the critical value of r at which a dip in $F(B)$ develops strongly depends on B_{m}, and in general for $B_{\mathrm{m}} \to 0$ increasingly larger values of r are necessary. A full treatment of the behavior of this function is considered beyond the scope of this Chapter.

Concluding, in this section we introduced an alternative analysis of OMAR lineshapes. In the slow-hopping limit, it reproduces both the Lorentzian, and a non-Lorentzian lineshape. More specifically, for model parameter $B_{\mathrm{m}} = 0$ we find:

$$\mathrm{MC}(B) \propto \frac{B^2}{(B^n + B_{\mathrm{hf}}^n)^{2/n}}, \tag{3.8}$$

and for $B_{\mathrm{m}} \gg B_{\mathrm{hf}}$:

$$\mathrm{MC}(B) \propto 1 - \frac{B_{\mathrm{m}} + B_{\mathrm{hf}}}{B_{\mathrm{m}} + (|B|^n + B_{\mathrm{hf}}^n)^{1/n}}, \tag{3.9}$$

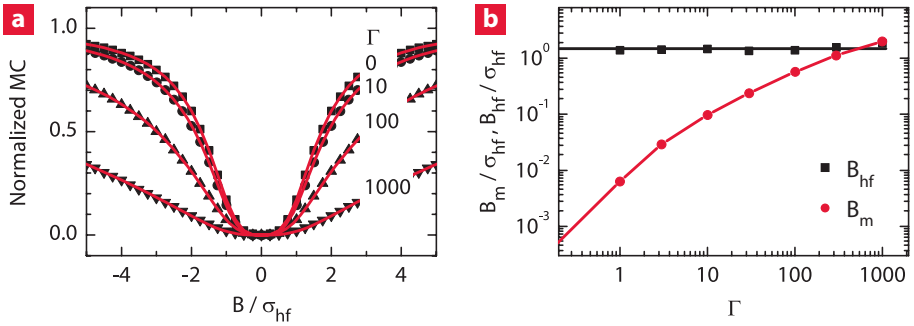

Figure 3.4 | Microscopic calculations fitted using the empirical lineshape. **a |** Normalized magnetoconductance as a function of the normalized magnetic field for a numerical integration of Eq. (2.7) over random hyperfine fields using different values of Γ. **b |** Intrinsic hyperfine contribution B_{hf} and additional broadening B_m, obtained by the fitting, as a function of Γ.

replacing Eqs. (3.1) and (3.2), respectively. For the case of equal hyperfine field distributions at the sites of the two reacting polarons, one should use $n = 3.1$ and the B_{hf} fitted from an experiment then corresponds to $\sqrt{(2)}\sigma_{hf}$. For intermediate cases, the full Eq. (3.5) should be applied. Extending to fast-hopping requires use of Eq. (3.7), while using a different value of $n = 2.3$ for calculating B_{eff} in Eq. (3.6).

3.3 Results and discussion

In the remaining part of this Chapter we will use Eqs. (3.5) and (3.7) to fit a selection of theoretical and experimental data sets, covering effects for different conditions and materials. In all cases, we find that for a single materials system B_{hf} is approximately constant while B_m and r account for the changes in the curves when any of the device conditions is being varied.

Numerical simulation

To illustrate the clear advantage of our empirical approach, let us re-examine the results of Fig. 3.2. Therefore, we calculated the normalized magnetoconductance for the two-site bipolaron model using different values of Γ. As can be seen in Fig. 3.2a for all values of Γ, the Lorentzian-like line shapes obtained from the two-site model is actually less rounded than expected from a pure Lorentzian behavior. This flattening can be assigned to the actual hyperfine field distributions considered, and the way they appear in the average MC. Moreover, with increasing Γ we observe a broadening of the MC(B) curves. Our empirical lineshape allows us to separately extract the intrinsic hyperfine field (B_{hf})

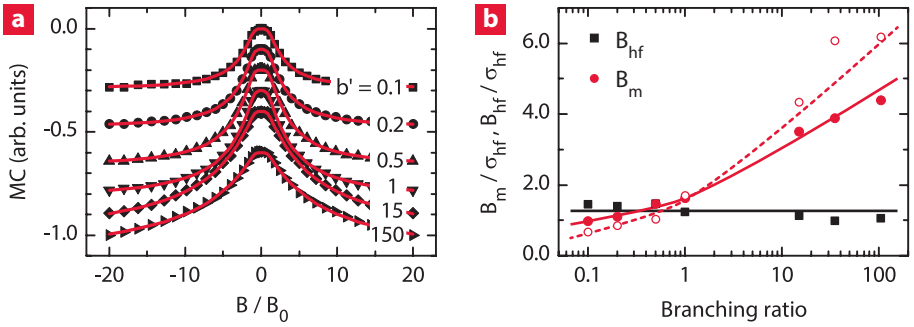

Figure 3.5 | Analyzing numerical simulation results using the empirical lineshape. a | MC curves from Monte Carlo simulations of the bipolaron model[68] for various branching ratios b' (curves are vertically shifted for clarity), fitted with Eq. (3.5) (lines). **b |** Characteristic fields B_{hf} and B_m, obtained by the fitting, as a function of branching ratio b'. Dashed lines are for individual fits, while full lines are for a global fit with $B_{hf} \approx 1.3\sigma_{hf}$ shared for all curves, where σ_{hf} is the average value of the hyperfine fields used in the simulations.

and additional broadening (B_m) caused by the microscopic mechanism. This is shown in Fig. 3.4b, where B_m increases over three orders of magnitude with increasing Γ while B_{hf} remains approximately constant.

For treating more complex cases, the simple two-site model can be extended using Monte Carlo simulations. In doing so, Bobbert *et al.* have shown that a Monte Carlo simulation of the bipolaron model can produce both Lorentzian and non-Lorentzian curves.[68] One of the parameters they investigated was the effect of the branching ratio. Therefore, Bobbert *et al.* introduced a factor b' by which all ratios for bipolaron formation and dissociation in the Monte Carlo scheme were multiplied. The results of the calculations are shown in Fig. 3.5a. We can observe that by changing only b', a gradual transition between the two types of curves is achieved. Re-analyzing these results, we fitted all the curves with Eq. (3.5) to obtain B_{hf} and B_m as a function of b'. The parameters resulting from these fits are shown in Fig. 3.5b. The values for B_{hf} thus found are nearly constant over the broad range of branching ratios, while B_m is found to change considerably. This is similar to the two-site model and indeed what would be expected based on the input of the simulations, where the hyperfine fields are kept constant for all the simulations and only the branching ratio is changed. Thus, the new function does not only allow us to fit the Lorentzian and non-Lorentzian curves, but also the intermediate cases.

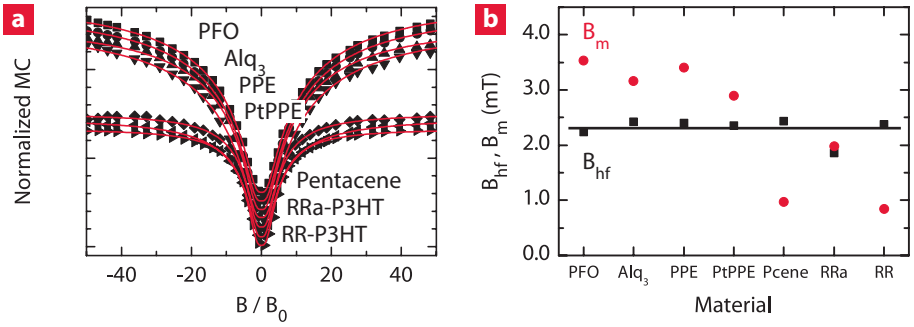

Figure 3.6 | Analyzing the MC of different organic materials using the empirical lineshape. a | OMAR curves measured for different materials, fitted with Eq. (3.5) (curves are vertically shifted for clarity). Data adapted from Ref. [110]. **b |** Characteristic fields B_{hf} and B_m, obtained by the fitting. The horizontal line indicates the mean $B_{hf} \approx 2.3$ mT.

Experimental results

Experimentally, for various materials different line shapes have been observed. We fitted the different curves reported by Mermer *et al.*,[110] as shown in Fig. 3.6a. Figure 3.6b shows that B_m completely determines the change in shape of these experimental curves, while B_{hf} has approximately the same value for all materials, $B_{hf} \approx 2.3$ mT. The values B_{hf} we thus find are considerably larger than those found from more recent data on similar materials, where care was taken to very accurately measure data near $B = 0$. Thus we conclude that in this specific case the value of 2.3 mT is largely affected by the instrumental resolution, and possibly characteristic differences in B_{hf} between different materials may be obscured. Our main focus here will be a further discussion of the differences in B_m. The variations in B_m can give additional information when comparing between materials or samples. For example, the value found for the polymer RRa-P3HT is larger than the value for the very similar polymer RR-P3HT. The main difference between the polymers is that RRa-P3HT is more disordered. In the bipolaron model, a larger disorder would indeed give a larger branching ratio, and thus a larger B_m according to Fig. 3.5b. Similarly, the small value of B_m for pentacene is also in good agreement with this observation, because pentacene is expected to be less disordered.

As an additional example, we analyzed results from experiments recently performed by Bloom *et al.* on devices using Alq_3 with a small fraction of DCM (a dye molecule that acts as both an electron and a hole trap).[83] Here, we will not go into the details of the experiments, but the main observations were a decrease of MC on increased DCM concentration, in combination with a broadening of the MC(B) curves, as shown in Fig. 3.7a. Moreover, on increasing the voltage,

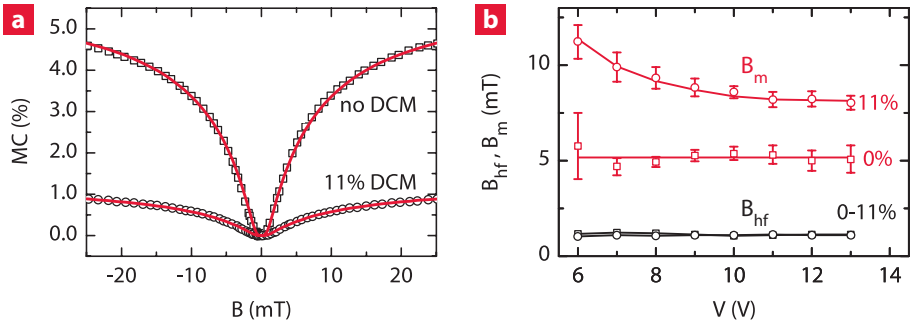

Figure 3.7 | Analyzing the MC of a blend of organic materials using the empirical lineshape. a | OMAR curves measured at 10 V for Alq_3 devices with and without DCM doping, fitted with Eq. (3.5). **b |** Characteristic fields B_{hf} and B_m, obtained by the fitting, as a function of voltage for different amounts of DCM doping.

the width of the curves decreased. We fitted the MC(B) curves with Eq. (3.5) to obtain B_{hf} and B_m as a function of voltage for the different doping concentrations, see Fig. 3.7b. The resulting B_{hf} are approximately constant for all measurements and all voltages, with a mean of $B_{hf} \approx 1.1$ mT. In sharp contrast, B_m changes considerably both between different doping concentrations and when changing the voltage. Thus, from these fits, it can be concluded that doping does not change the hyperfine fields, but changes the microscopic processes involved in OMAR. More generally, the fitting results show that all the changes in the shape and width of OMAR curves can most likely be attributed to details of the microscopic model.

The reader may have noticed that B_{hf} values found by fitting the experimental results with our new function are smaller than the values of B_0 obtained with the conventional Lorentzian and non-Lorentzian functions. The latter values of B_0 were considered anomalously large compared to the hyperfine coupling constants known for these materials ($B_0 = 5.8$ mT versus a hyperfine coupling of 1.8 mT for pentacene).[107] The values found for B_{hf} using the new function ($B_{hf} = 1.1 \pm 0.1$ mT) are more in the range of these hyperfine coupling constants. It should be noted that B_{hf} for Alq_3 in Fig. 3.6b and 3.7b differ more than a factor of two. Most probably this is due to the limited experimental resolution in Fig. 3.6b, as commented on before.

Intermediate hopping

Finally, we discuss effects of fast-hopping again using both model simulations and experimental data sets. In Sec. 3.2 we saw how increasing the hopping rate (increasing r) leads to a broadening of MC line shapes, and ultimately to

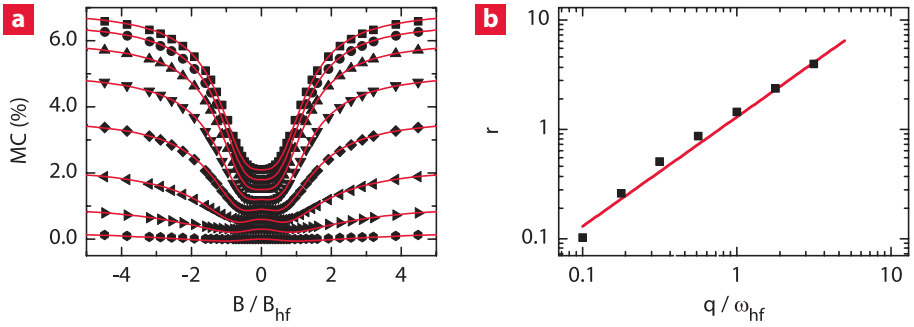

Figure 3.8 | Analyzing the MC in the intermediate hopping regime using the empirical lineshape. a | MC curves from density matrix calculations of the e–h mechanism for various hopping rates r (curves are vertically shifted for clarity), fitted with Eq. (3.7) using only r as fitting parameter (lines). **b |** The value of r obtained from the fit as a function of e–h pair dissociation rate q, where the drawn line is a fit assuming that q and r are proportional.

the appearance of an additional dip at ultra-small fields (USFE). In Fig. 3.8 we applied the extended fitting function, Eq. (3.7), to a numerical data set. We were able to obtain a satisfactory fit to all lineshapes, including their relative amplitude, by fitting r and keeping all other parameters fixed for all curves. The fitted values of r thus obtained are plotted in the Fig. 3.8b. We observe an almost perfect scaling with the dissociation rates q used for the numerical simulations. This result demonstrates that not only Eq. (3.7) is capable of fitting line shapes in the fast-hopping regime, it also can be used to extract sensible physical parameters, and properly reproduces physical trends. Without further proof, we mention that an even better fit of the anomalous feature around $B = 0$ can be obtained by allowing for small differences in the values of n used for different curves. Such a further optimization is considered beyond the scope of this Chapter.

As a final example of the relevance of our new analysis, but without attempting a full fitting of data sets, we emphasize its importance for recent experiments where changes of OMAR curves upon deuteration are being explored. In such experiments, one might naively predict the line shapes to be just scaled by the ratio of the relative hyperfine field of deuterium with respect to the one of hydrogen. However, in cases where the hopping parameter r is not much smaller than unity this can turn out be quite inadequate. While lowering B_{hf} by a factor of 3.26 (the ratio of the nuclear magnetic moments), the value of r increases by the same factor. Thereby the tendency of narrowing upon deuteration can be partially compensated by a less efficient dephasing, which tends to broaden the curves.

3.4 Conclusion

In conclusion, we introduced a new empirical function that allows us to separately extract the role of the hyperfine field and the broadening induced by the microscopic mechanisms involved. By addressing recent numerical and experimental studies on OMAR, it was shown that the new function can be successfully used to analyze MC(B) curves. The tool thus developed is believed to be extremely useful within future research on OMAR.

Temperature and voltage dependence of magnetic field effects in organic semiconductors

4

*In recent years it was discovered that the current through an organic semiconductor, sandwiched between two non-magnetic electrodes, can be changed significantly by applying a small magnetic field. This surprisingly large magnetoresistance effect, often dubbed as organic magnetoresistance (OMAR), has puzzled the young field of organic spintronics during the last decade. Here, we present a detailed study on the voltage and temperature dependence of OMAR, aiming to unravel the lineshapes of the magnetic field effects and thereby gain a deeper fundamental understanding of the underlying microscopic mechanism. Using a full quantitative analysis of the lineshapes we are able to extract all linewidth parameters and the voltage and temperature dependencies are explained with a recently proposed trion mechanism. Moreover, explicit microscopic simulations show a qualitative agreement to the experimental results.**

*Under review at Journal of Applied Physics as: *Unraveling the temperature and voltage dependence of magnetic field effects in organic semiconductors.* P. Janssen, S.H.W. Wouters, M. Cox and B. Koopmans.

4.1 Introduction

One of the exciting developments in the field of organic electronics is the discovery of a surprisingly large, room temperature, magnetoresistance effect in organic semiconductor devices without any ferromagnetic components, an effect often referred to as organic magnetoresistance (OMAR).[33,34] The current through such a device, where the organic layer is sandwiched between two non-magnetic electrodes, can be changed significantly (up to 25%) by applying a small (~mT) magnetic field. The effect can be tuned by changing the operating conditions such as voltage, temperature and angle between the current and magnetic field.[35,87,102,104,106,111–118] Recently, cheap plastic sensor technology has been proposed as an example of its application potential.[44] Nevertheless, a fundamental understanding of the interactions of spins and charges in organic semiconductors currently remains the goal of extensive experimental[33–35,87,102,104,106,111–118] and theoretical[68–70] research.

To explain OMAR, all contemporary models incorporate pairs of spin-carrying particles undergoing spin-dependent reactions. The outcome of these reactions is influenced by the intrinsic mixing of the pair's spin state and subsequent suppression thereof in an external applied magnetic field. The models then diverge on the matter of which particle reaction is at the origin of OMAR. One can mainly distinguish between the reactions of: (i) equally charged polarons into bipolarons,[68] (ii) polaronic electrons and holes[69] and (iii) triplet excitons with polarons or other triplets.[70] Very recently, we have shown that the dominant mechanism for OMAR depends on the exact material choice and operating conditions of the device.[119] Therefore, a thorough investigation of all relevant operating conditions is crucial in understanding magnetic field effects (MFEs) in organic semiconductors.

As introduced in the foregoing, mixing of spin states plays a crucial role in OMAR, regardless of the exact underlying model. There is a growing consensus about the importance of hyperfine fields, originating from the hydrogen nuclei in the organic material, for spin mixing.[87] In this case the lineshape of the OMAR curve is related to the hyperfine field strength which is on the order of a millitesla and we will refer to this as a low-field effect (LFE). The lineshape is, however, not only determined by the magnitude of the hyperfine fields. From the bipolaron model, for example, it is known that even with the same hyperfine fields, additional broadening occurs when the bipolaron formation rate is increased.[68,120] Moreover, it has recently been shown that the LFE can be accompanied by a distinct magnetic field effect at ultra-small field scales (USFE, typically $\leq$ mT).[87] Beside low-field effects, OMAR curves can also show distinct features at higher magnetic field scales (HFE, ~ 20 mT up to a few Tesla). Accurately measuring and understanding the exact lineshapes of the LFE and

HFE is therefore of major importance, since the lineshapes can be correlated to the dominant underlying mechanism.[119]

In this Chapter we present a detailed study on the voltage and temperature dependence of OMAR, aiming to unravel the magnetic field effects on the current in pristine conjugated polymer devices. Even though OMAR has been studied extensively, there are only a few detailed reports on its temperature dependence.[34,35,102,111–113] Moreover, these studies mainly focus on the magnitude of the OMAR effect. We show a full quantitative analysis of the lineshape and also extract the linewidth parameters. It was demonstrated before that in OLED type devices the MFEs are dominated by the reactions between (trapped) triplets and polarons.[70,78,121] A schematic overview of this mechanism is shown in Fig. 4.1. Here, the relevant particles and their (spin-dependent) reactions are depicted as a function of energy. We can distinguish between the rates of dissociation and recombination of singlet and triplet electron–hole pairs ($q_{S,T}$ and $k_{S,T}$) or doublet and quartet triplet–polaron pairs ($r_{D,Q}$ and $k_{D,Q}$) respectively.[78] The low magnetic field effect (LFE) originates from mixing of precursor pairs by hyperfine fields (hf). Whereas the mixing of triplet exciton–polaron pairs at the zero field splitting field scale (ZFS) leads to a high-field effect (HFE). By studying the MFE lineshapes as a function of voltage and temperature we obtain a deeper understanding of these triplet–polaron reactions.

4.2 Methods

Device fabrication

In this work we studied the magnetic field effects on the current for devices consisting of a phenyl substituted poly(1,4-phenylenevinylene) semiconducting polymer called Super Yellow PPV (SY-PPV, Merck, used as received). The SY-PPV is dissolved in orthodichlorobenzene (ODCB) at a concentration of 8 mg/mL, and stirred on a hot plate at 50 °C for at least 2 hours. The devices were prepared on glass substrates with patterned indium tin oxide (ITO) anodes. After careful cleaning, followed by a UV-ozone treatment, a thin layer of poly(3,4-ethylenedioxythipophene):poly(styrenesulfonate) (PEDOT:PSS) was applied by spin coating. The SY-PPV was spin coated at 1200 RPM for 60 seconds, resulting in a layer thickness of 100 nm. Subsequently, the samples were transferred to a nitrogen filled glove box where the cathode, consisting of LiF and Al, was evaporated in a high vacuum system ($\leq 10^7$ mbar). From this point on, the samples always remained in a dry nitrogen environment. The total junction stack thus consisted of ITO/PEDOT:PSS(60 nm)/SY-PPV(100 nm)/LiF(1 nm)/Al(100 nm).

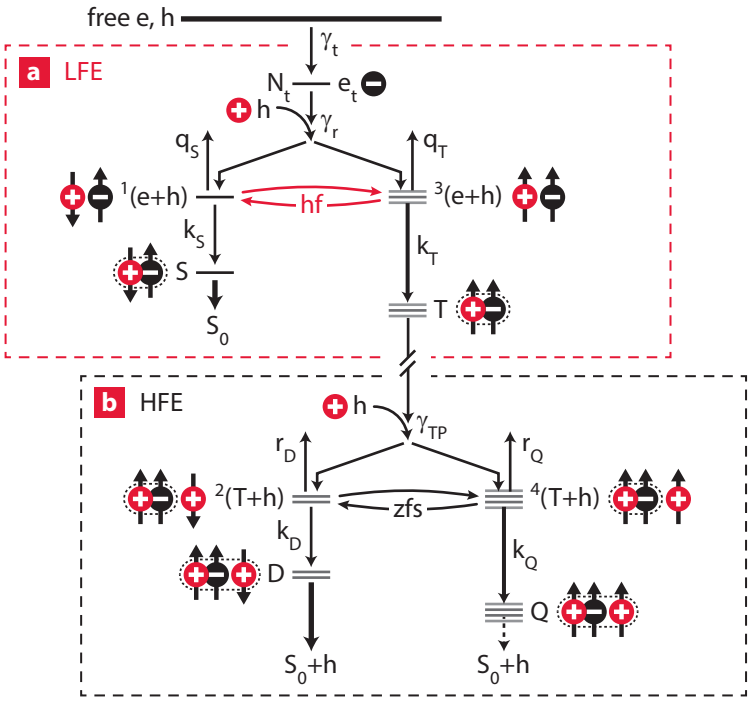

Figure 4.1 | A schematic overview of all relevant particles and reactions of the trion model. a | The low magnetic field effect (LFE) originates from mixing of polaronic electron–hole pairs by hyperfine fields (hf). **b |** Whereas the mixing of triplet exciton–polaron pairs at the zero field splitting field scale (ZFS) leads to a high-field effect (HFE).

Measurements

Magnetic field effect measurements were performed in a cryostat that is attached to a glovebox with a dry nitrogen environment ($[O_2] < 0.3$ ppm, $[H_2O] < 0.3$ ppm) and the sample temperature can be controlled from 10 K up to room temperature. The cryostat is placed between the poles of an electromagnet, which allows us to apply an external magnetic field up to 0.5 T, with an accuracy of 50 μT. The devices were driven at a constant voltage V using a Keithley 2400 Series SourceMeter. We measured the current I through the device while sweeping the magnetic field B. From this measurement, the magnetoconductance (MC) was calculated with $\mathrm{MC}(B) = [I(B) - I(0)]/I(0)$. Please refer to Appendix 4.A for a detailed description of the measurement procedure.

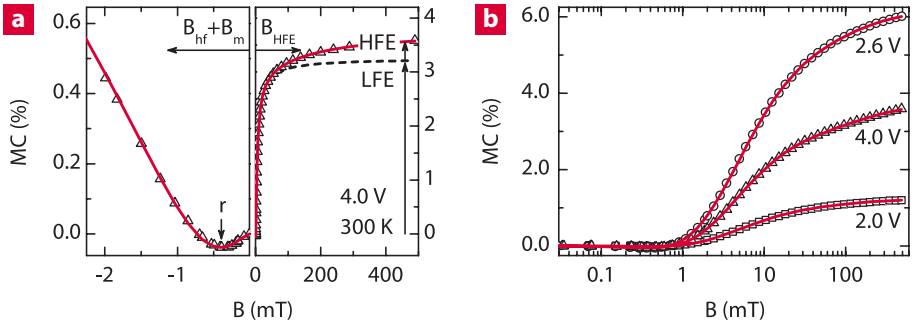

Figure 4.2 | Magnetoconductance as a function of magnetic field. a | Experimental result for a bias voltage of 4.0 V at roomtemperature. The solid line is a fit using the empirical lineshape Eq. (4.1), where the low (LFE) and high magnetic field (HFE) contributions are separately depicted. The magnitude of LFE and HFE and their corresponding linewidth parameters (B_{hf}, B_{m}, r and B_{HFE}) are also shown. **b |** Magnetoconductance as a function of magnetic field on a logarithmic scale for different bias voltages.

Empirical lineshapes

In this study, we analyzed the magnetoconductance as a function of magnetic field $\mathrm{MC}(B)$ for different voltages and temperatures (refer to Fig. 4.2 for a typical result). To analyze the experimental results, we used the following fitting function:

$$\mathrm{MC}(B) = \mathrm{LFE} \cdot f(B, B_{\mathrm{hf}}, B_{\mathrm{m}}, r) + \mathrm{HFE} \cdot \frac{B^2}{(|B| + B_{\mathrm{HFE}})^2} \tag{4.1}$$

The function $f(B, B_{\mathrm{hf}}, B_{\mathrm{m}}, r)$, with $f(B = 0) = 0$ and $f(B = \infty) = 1$, is explained in full detail in Chapter 3. The function correctly describes the low-field effect (LFE) including the ultra-small-field effect, as is shown in the left panel of Fig. 4.2a. This empirical function allows us to separately extract the role of the intrinsic hyperfine field (B_{hf}) and the extrinsic additional broadening (B_{m}) induced by the microscopic mechanism. The function converges to a Lorentzian lineshape for $f(B_{\mathrm{m}} = 0)$ and a so-called non-Lorentzian for $f(B_{\mathrm{m}} \gg 0)$. The USFE is incorporated by the parameter r which describes the limit in which hopping of carriers is no longer slow compared to spin precession in the hyperfine fields. The high-field effect (HFE) is fitted with non-Lorentzian lineshape and has a characteristic linewidth B_{HFE}. In the fitting procedure, the hyperfine field B_{hf} is a shared fitting parameter, whereas the other parameters (LFE, B_{m}, r, HFE and B_{HFE}) can vary with temperature and voltage.

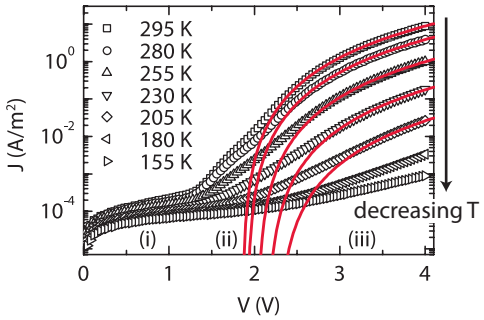

Figure 4.3 | Current density as a function of voltage for different temperatures. Three regimes are depicted: (i) an ohmic leakage current, (ii) a diffusion current below the built-in voltage ($V_{bi} \approx 2$ V) and (iii) a space-charge limited current above the built-in voltage. The solid line is a power law fit for the space-charge limited regime.

4.3 Results and discussion

Current density

In order to fully understand the voltage and temperature dependence of the magnetic field effects, we first need to address the effects on the current without an applied magnetic field. Therefore, we have measured the current density J as a function of voltage V for different temperatures T and the results are shown in Fig. 4.3. We can identify three transport regimes: (i) an ohmic leakage current at the lowest voltages, (ii) a diffusion current in the diode regime below the built-in voltage ($V_{bi} \approx 2$ V), with a rectifying exponential dependence $J \sim \exp(qV/nk_BT)$ and (iii) a space-charge limited current above the built-in voltage, with a power law dependence $J \sim (V - V_{bi})^n$. Using this relation, we can extract V_{bi} and n, as depicted by the solid line in Fig. 4.3. We obtain a power factor $n = 3.1$, whereas $n = 2$ for a trap free device with ohmic electrodes, indicating the presence of traps in the organic layer. [56]

Magnetic field effects

To investigate the magnetic field effect on the current, we have systematically measured the magnetoconductance as a function of magnetic field, bias voltage and temperature. We have analyzed the results by fitting this extensive experimental data set using Eq. (4.1), which allows us to unravel the lineshape of the MFE as a function of voltage and temperature. A typical result is shown in Fig. 4.2. It is found that the lineshapes are accurately described, thereby obtaining reliable values for the amplitudes and linewidth parameters of the low- and high-field effects. Moreover, the ultra-small-field effect is also accurately

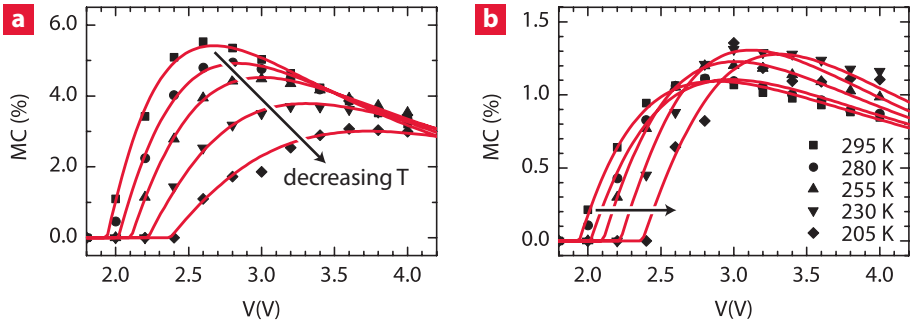

Figure 4.4 | Magnetic field effects as a function of voltage for different temperatures. a | Magnitude of the low-field effect (LFE) as a function of voltage for different temperatures. **b |** Magnitude of the high-field effect (HFE) as a function of voltage for different temperatures. The solid lines are a fit using the trion model.

characterized. We will start our discussion with the amplitudes of the MFEs. Thereafter, we will address the linewidths.

The magnitude of the low- and high-field effect as a function of voltage and temperature is shown in Figs. 4.4a and b, respectively. Both magnetic field effects show a very characteristic MC(V) dependence, vanishing below the built-in voltage and peaking somewhat above. Both the onset as well as the peak value of the magnetic field effect MFEs, shift to higher voltages with decreasing temperature. Lately, it was shown that the magnetic field effect on the current in pristine organic semiconductors is predominantly governed by the reactions between triplet excitons and polarons.[70,78,119,121] Moreover, Cox *et al.* recently proposed an analytical model where these reactions are described by the spin-selective formation of so-called metastable trions from triplet exciton–polaron pairs.[78] Their model provides an intuitive explanation of the MC(V) dependence. The initial increase originates from the increase of triplet density with voltage, while the eventual decrease can be assigned to a saturation of trap filling.

In addition to this qualitative explanation, we analyzed the MC(V)-curves using the analytical model as proposed by Cox *et al.* To describe the amplitude of the low-field effect, only two free fitting parameters are used: the onset voltage V_{on} and the triplet–polaron interaction coefficient γ_{TP}. The other parameters such as the trap density (N_t ~10^{-4} nm^3), electron trap coefficient (γ_t ~10^5 nm^{3}s^{-1}), electron–hole capture coefficient (γ_R ~10^8 nm^{3}s^{-1}), triplet rate (k_T ~10^4 s^{-1}) and trion rate (k_Q ~10^3 s^{-1}), indicated in Fig. 4.1, are taken from the literature.[122–124] The resulting fits are depicted by the solid lines in Fig. 4.4a and describe the MC(V)-curves remarkably well.

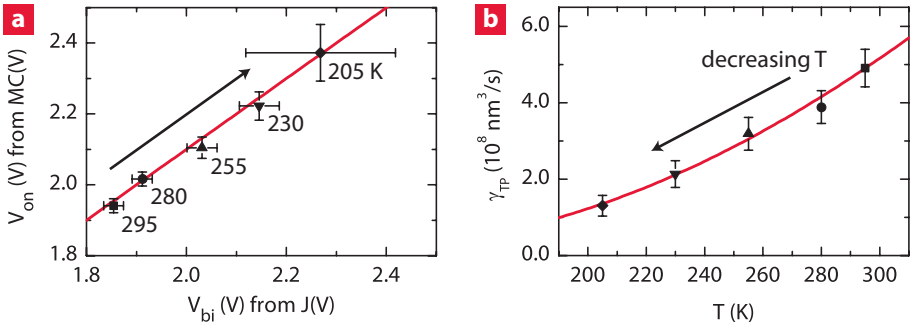

Figure 4.5 | Extracted model parameters as a function of temperature. **a |** The onset voltage V_{on} obtained from the fit of the MC(V)-curves using the trion model compared to the built-in voltage V_{bi} as acquired from the $J(V)$-curves. The solid line is a guide to the eye showing a clear correlation between the two voltages. **b |** The reaction rate between trions and free polarons γ_{TP}, extracted from the LFE, as a function of temperature.

To confirm the physical validity of the fitting parameters, we have plotted the onset voltage V_{on} obtained from the fit of the MC(V)-curves as a function of the built-in voltage V_{bi} as acquired from the $J(V)$-curves. The result is shown in Fig. 4.5a. We observe a clear correlation between the two voltages, i.e., once the condition for bipolar charge injection is met ($V > V_{bi}$), we can measure a MFE ($V > V_{on}$), indicating the importance of both charge carriers for the measured MFE. The increase in built-in voltage with decreasing temperature is in agreement with literature results.[94,125] Furthermore, we can evaluate the triplet–polaron interaction coefficient γ_{TP} as a function of temperature. The triplet–polaron interaction has been shown to scale with temperature as $\gamma_{TP} \propto \mu_h \langle R \rangle kT$,[122] where $\langle R \rangle$ is the interaction radius. The hole mobility scales with $\mu_h \propto \exp(-\Delta/kT)$, where Δ is the activation energy.[56] The triplet–polaron interaction coefficient as a function of temperature can be described using this relation, as shown in Fig. 4.5b. We find an interaction radius $\langle R \rangle \sim 10^{-9}$ m when using an activation energy $\Delta = 0.48$ eV which is in agreement with literature values.[56]

The analytical model can also explicitly describe the magnitude of the high-field effect, as is shown in Fig. 4.4b. The temperature dependence of the high-field effects is less pronounced than the low-field effect. In passing, we note that, assuming V_{on} is equal for the LFE and HFE, there is only one remaining free fitting parameter, namely the trion dissociation rate. Although the resulting fit is not as accurate as the low-field effect, it still captures the essential trends.

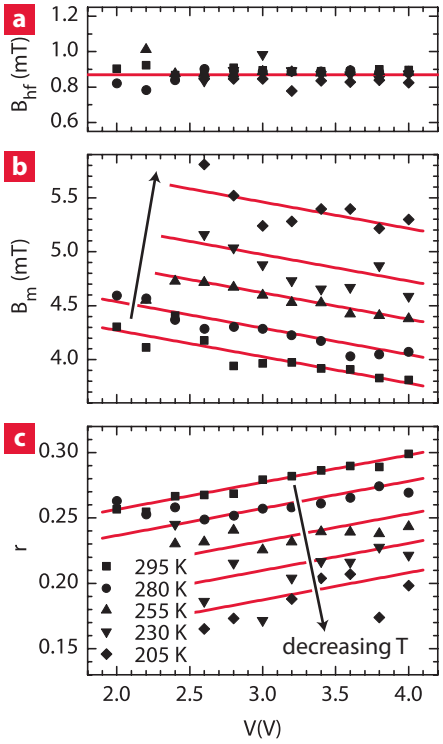

Figure 4.6 | Extracted low-field effect parameters as a function of voltage for different temperatures. a | The hyperfine field strength B_{hf} showing no temperature dependence. **b |** The extrinsic low-field linewidth B_m as a function of voltage and temperature. The solid lines are a guide to the eye showing a decrease in linewidth with increasing voltage and temperature. **c |** The hopping ratio r as a function of voltage and temperature. The lines are a guide to the eye showing an increase in hopping rate with increasing voltage and temperature.

Linewidth analysis

After this satisfactory description of the magnitudes of the magnetic field effects, we continue our discussion with the linewidths of the effects, where we first adres the low-field effect. Figure 4.6a–c show the intrinsic hyperfine field strength B_{hf}, the additional broadening of the low-field linewidth B_m and the ratio between hopping and precession r, respectively. Using our fitting procedure, we find, as expected, no temperature dependence in the hyperfine field strength and obtain an almost identical hyperfine field strength of approximately 0.9 mT for all measurements. However, B_m and r do show a remarkable voltage and temperature dependence. In previous studies, the explicit linewidths have often been neglected. Nevertheless, studying the voltage and temperature dependency

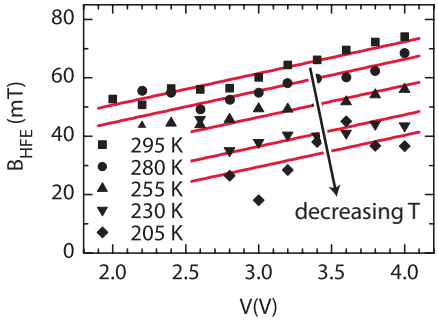

Figure 4.7 | Extracted high-field effect parameter as a function of voltage for different temperatures. The linewidth of the high-field effect B_{HFE} shows an increase in linewidth with increasing voltage and temperature.

of the linewidths provides new insights in the underlying mechanisms for the MFEs on the current. The lines in Fig. 4.6b indicate a decrease in B_{m} with increasing voltage and temperature. To explain this dependency, we need to elucidate the exact role of the extrinsic low-field linewidth parameter. Therefore, we performed numerous simulations and investigated the linewidths of the magnetic field effect MFEs.[79,120] The simulations reveal that additional broadening can be observed when the formation, dissociation and recombination rates of the interacting polaron pairs are altered. Although a full description goes beyond the scope of this present Chapter, a brief discussion of our findings is presented in the next section.

The final parameter, which we introduced to correctly describe the ultra-small-field effect, is the ratio between hopping and precession r. Figure 4.6c shows this ratio as a function of voltage and temperature and an increase in hopping rate with increasing voltage and temperature is observed. This trend can intuitively be explained by the increase in hopping rates upon raising the bias voltage or temperature, whereas the precession frequency remains unaffected. One might naively expect a much larger dependency of r on the voltage and temperature. We conjecture that this weak dependency is caused by a distribution of hopping times.[66] Only a certain range of hopping rates contribute to the MFEs in the current, because the fastest hops are not influenced by hyperfine based mixing mechanisms and the slowest hops hardly contribute to the total current. Changing the voltage or temperature only shifts the small range of hops which contribute to the MFEs.

Finally, we will discuss the linewidth of the high-field effect. The width of the HFE, caused by triplet–polaron interactions, is known to be related to the zero-field splitting (B_{ZFS}) of the triplet excitons, which is independent of temperature. Yet, in contrast to the hyperfine field strength, the linewidth of the high-field

effect does show a clear voltage and temperature dependence, as can be seen in Fig. 4.7. We attribute this difference to our description of the high-field effect, which is characterized by a single linewidth parameter B_{HFE}. We propose that the high-field effect also has an intrinsic component, governed by the zero-field splitting rather than the hyperfine field, and an additional broadening parameter. This additional broadening will also be briefly discussed using simulations in the next section.

Simulations

In all the models that have been proposed for OMAR, the magnetic-field dependent reactions of the spin carrying particles play an essential role. Schellekens *et al.* used an adapted Stochastic Liouville equation in a density-matrix formalism to successfully perform calculations on magnetic field effects in organic semiconductors.[79] We have used their approach to simulate magnetic field effects caused by triplet–polaron interactions. The calculations for the LFE and HFE, indicated by the dashed boxes in Fig. 4.1, are schematically depicted in Fig. 4.8a and b respectively. We calculated the influence of changes in the different recombination and dissociation rates on the MFEs lineshapes.

For the LFE, the simulations reveal that additional broadening can be observed when the recombination and dissociation rates for singlets (k_S, q_S) and triplets (k_T, q_T) are varied, as is clearly shown in Fig. 4.8c. We have analyzed the LFE lineshape using Eq. (4.1), where we have fixed the value of the hyperfine field strength so that the only free fitting parameter is the extrinsic broadening parameter B_{m}. The results are shown in Fig. 4.8e. Increasing the dissociation rate, while keeping the other rates in the system constant, causes less broadening of the MC(B)-curves, as described by a decrease in B_{m}. We conjecture that an increase in voltage or temperature can increase the dissociation rate of the polaron pairs and, accordingly, decrease the extrinsic low-field linewidth B_{m}. This is in agreement with our experimental results. Furthermore, the simulations show that this effect is more pronounced for a greater singlet to triplet recombination ratio. In passing we note that the simulations do not take device physics into account, which could also cause additional broadening.

Finally, we have calculated the HFE for triplet–polaron interactions as a function of the magnetic field for different triplet–polaron dissociation (r_D) and reaction rates (k_D). The resulting lineshapes are shown in Fig. 4.8d. The HFE lineshape shows a similar lineshape as the LFE, but, as mentioned before, on a different field scale (B_{ZFS} instead of B_{hf}). From the calculations we can conclude that an increase in reaction rate, while keeping the other rates in the system constant, causes additional broadening of the MC(B)-curves even though B_{ZFS} is kept constant. We have also analyzed the HFE lineshape using our empirical function. In this case, the intrinsic linewidth, which is governed

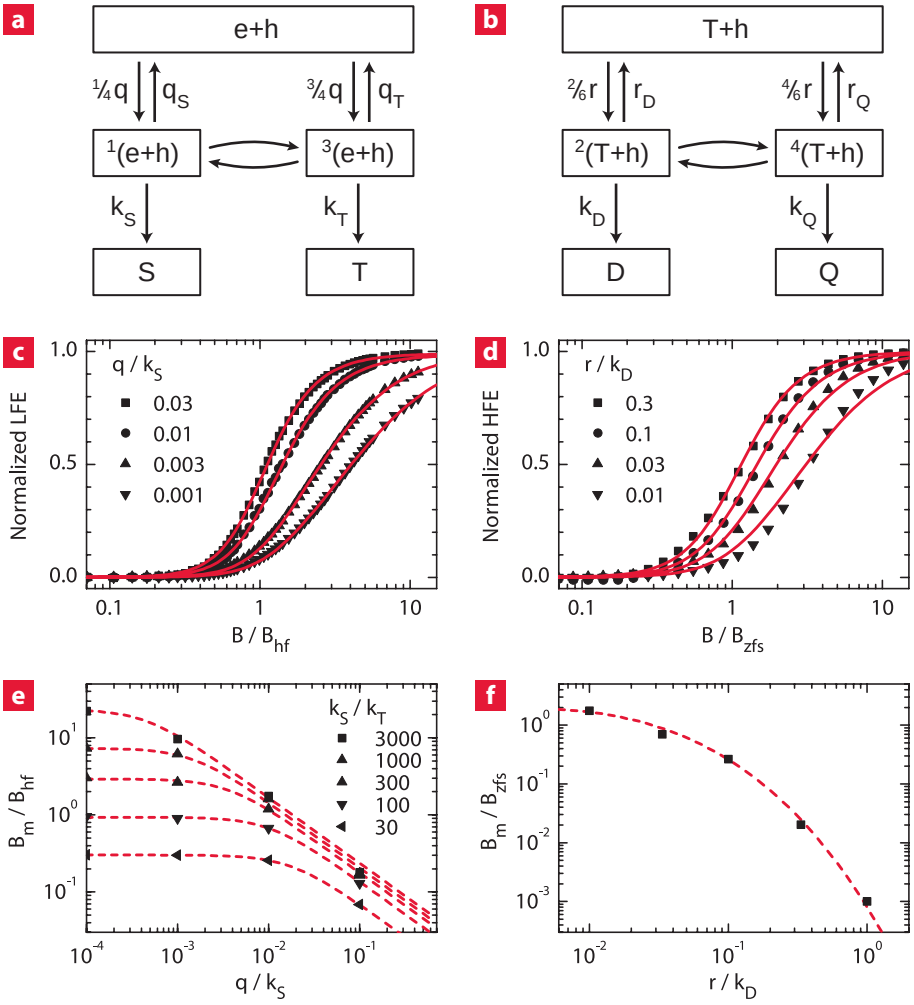

Figure 4.8 | Simulating the magnetic field effects linewidths. a | Simulations for the low-field effect (LFE) and **b |** high-field effect (HFE). Normalized **c |** LFE and **d |** HFE as a function of the normalized magnetic field. Additional broadening extracted from the simulations for the **e |** LFE and **f |** HFE linewidths. Solid lines are fits and the dashed lines provide a guide to the eye.

by B_{ZFS} instead of B_{hf}, is also fixed so that the only free fitting parameter is the extrinsic broadening parameter B_m. The result is shown in Fig. 4.8f. We conjecture that an increase in voltage or temperature could lead to an increase in reaction rate, explaining the experimental results in Fig. 4.7. Please note that, to the best of our knowledge, these calculations are the first to show the influence of the different triplet–polaron reaction rates on the HFE lineshape.

4.4 Conclusion

In conclusion, we have investigated the magnetic field effect on the current for a wide range of temperatures and voltages. Using a full quantitative analysis of the lineshapes we are able to extract all linewidth parameters (both the linewidths and amplitudes) and explain their voltage and temperature dependence accordingly. We attribute the MFEs to the recently proposed trion mechanism.[78] We analyzed the MC(V)-curves using the analytical model as proposed by Cox *et al*. and confirmed the physical validity of the fitting parameters. The linewidths of the low-field effects have been analyzed and we show that the hyperfine field strength B_{hf} is almost identical for all measurements, whereas B_m and r do show a remarkable voltage and temperature dependence. Finally, the high-field effect linewidth B_{HFE} also show a surprising voltage and temperature dependence. Preliminary results on microscopic simulations show a qualitative agreement to the experimental results. This opens up unprecedented routes towards a deeper fundamental understanding of the relevant triplet polaron reaction rates for OMAR.

Appendix 4.A Measuring organic magnetoresistance

We measure the magnetic field effects using a dedicated setup which attached to a glovebox with a dry nitrogen environment. The setup allows us to use many different measurement techniques. We can measure the current through the devices and simultaneously their light output. Furthermore, by illuminating the devices with an external light source, we can measure the photocurrent. This can all be done while applying a varying magnetic field. Moreover, the samples can also be rotated in the magnetic field during the measurements.

To measure the magnetoconductance as a function of magnetic field, one could simply measure the current trough the device at constant bias voltage while sweeping the magnetic field. However, this simple scheme is very inaccurate if the current also changes (in time) without applying a magnetic field. This effect is often referred to as drift and it is observed in many organic semiconductor devices.[126] A typical example of a drift in the current is shown in Fig. 4.9a. For the devices studied in this thesis, it has been found that after a certain time the

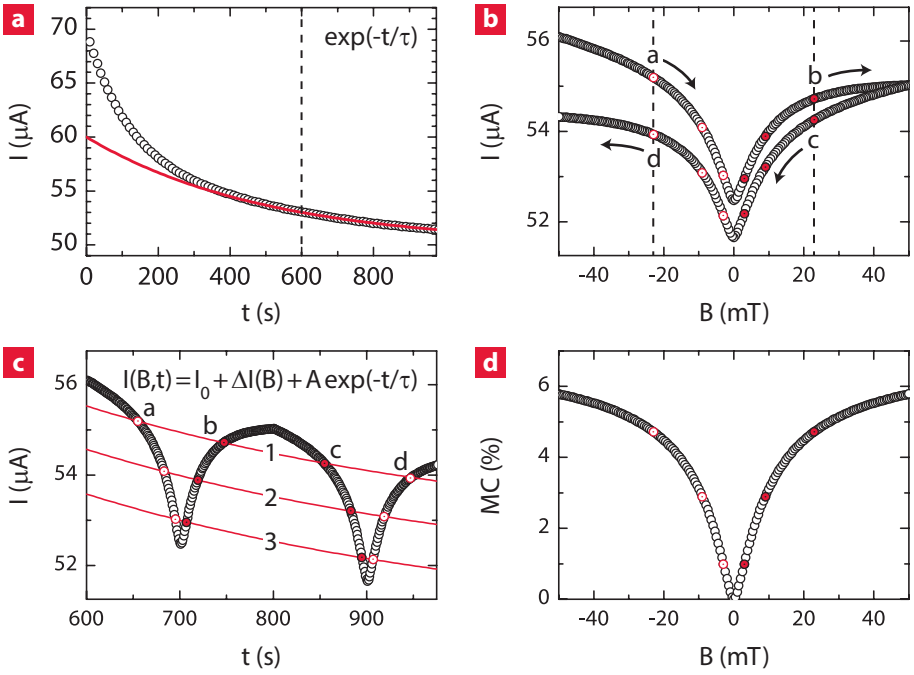

Figure 4.9 | Method for measuring organic magnetoresistance. a | The current through an organic semiconductor device changes in time even without applying a magnetic field. **b |** We measure the current while sweeping the magnetic field forward and backward. **c |** The current as a function of time while sweeping the magnetic field. **d |** The magnetoconductance after correction for the drift.

drift in the current can be described with a single exponential decay, as depicted by the dashed line in Fig. 4.9a. To separate the magnetic field effect from the drift in the current we can use different approaches. We can use a lock-in based modulation technique [57] or use an alternative scheme for the measurement. In this Chapter we have used the latter, which is illustrated in Fig. 4.9 and will now be described in more detail.

Prior to the measurement, we apply a constant bias voltage over the device and wait for the drift to relax to a single exponential decay as indicated in Fig. 4.9a. Then, we start the measurement by measuring the current trough the device while sweeping the magnetic field from negative to positive and back as shown in Fig. 4.9b. As a result, the current trough the device is now a function of time and magnetic field and can be described by:

$$I(B, t) = I_0 + \Delta I(B) + \exp(-t/\tau), \tag{4.2}$$

where I_0 is the current without a magnetic field, $\Delta I(B)$ the change in current due to the externally applied magnetic field and $\exp(-t/\tau)$ describes the drift in time. Figure 4.9c shows the current in time while sweeping the field.

In the devices as studied throughout this thesis, the magnetic field effects do not display any hysteresis. Therefore, the change in current at a specific magnetic field should be the same for the forward and backward sweep, i.e. $\Delta I(a) = \Delta I(d)$ in Fig. 4.9b and c. Moreover, if the magnetic field effect is symmetric, than there is no dependence on the polarity of the magnetic field, i.e. $\Delta I(a) = \Delta I(b) = \Delta I(c) = \Delta I(d)$. We are now able to separate the drift from the magnetic field effect by fitting the data in Fig. 4.9c for a fixed magnetic field (23 mT in this example) using Eq. 4.2. To increase the accuracy of the fit, we can perform this fitting routine for multiple magnetic fields simultaneously (3 in this example). The resulting magnetoconductance is calculated using $\mathrm{MC}(B) = \Delta I(B)/I_0$ and the result is shown in Fig. 4.9d. In the example as discussed above, we have used a linear point distribution in the magnetic field. In this thesis, however, we also often use a logarithmic distribution. Furthermore, we are not restricted to a linear sweep in time. Using simple interpolation techniques, we are able to extract the magnetic field effect using an arbitrary distribution in time and magnetic field.

5

Tuning spin interactions in organic semiconductors

Harnessing the spin degree of freedom in semiconductors is generally a challenging, yet rewarding task. In recent years the large effect of a small magnetic field on the current in organic semiconductors has puzzled the young field of organic spintronics. Although the microscopic interaction mechanisms between spin carrying particles in organic materials are well understood nowadays, there is no consensus as to which pairs of spin carrying particles are actually influencing the current in such a drastic manner. Here, we demonstrate that the spin-based particle reactions can be tuned in a blend of organic materials, and microscopic mechanisms are identified using magnetoresistance lineshapes and voltage-dependencies as fingerprints. We find that different mechanisms can dominate, depending on the exact materials choice, morphology and operating conditions. Our improved understanding will contribute to the future control of magnetic field effects in organic semiconductors.[*]

[*] Accepted for publication in Nature Communications as: *Tuning organic magnetoresistance in polymer-fullerene blends by controlling spin reaction pathways.* P. Janssen, M. Cox, S.H.W. Wouters, M. Kemerink, M.M. Wienk and B. Koopmans.

5.1 Introduction

The field of organic spintronics deals with spin physics and magnetic field effects in organic materials.[30,127] Besides spin injection into organic semiconductors,[37,38] a lot of attention was drawn to non-spin-polarized organic semiconductor devices. Despite the absence of magnetic elements, they show a large room-temperature magnetoresistance effect at relatively small magnetic fields of only a few millitesla, an effect sometimes referred to as organic magnetoresistance (OMAR).[33,34,68–70,79,86,87,89,91,104,106,114–118] Cheap plastic sensor technology has been suggested as an example of its application potential.[44] However, since this magnetic field effect was discovered a decade ago, the desire to unravel the exciting new physics behind the intrinsically magnetic-field dependent charge transport properties of organic semiconductors has been the major motivation for intensive experimental[33,34,87,104,106,114–118] and theoretical[68–70,79,86,89,91] research.

Several mechanisms have been suggested to explain organic magnetoresistance. These mechanisms all rely on spin-selective reactions between pairs of particles, where a magnetic field suppresses the spin mixing of the particle pairs prior to the reaction, thereby changing the spin fraction and the outcome. Partly based on recent studies –where the magnetic field effects from standard and deuterated polymers were compared– there is a growing consensus about the importance of hyperfine fields for spin mixing.[87] The principal question in the field is now which particle pairs and subsequent reactions are dominating this magnetic field effect. The possible mechanisms are currently divided into three categories: (i) reactions of polarons with the same charge into bipolarons ,[68] (ii) reactions of polarons with opposite charge into excitons[69] and (iii) reactions of triplet excitons with polarons[70] or with other triplet excitons.[71] We will refer to those mechanisms as bipolaron, electron–hole (e–h), triplet–polaron and triplet–triplet mechanism, respectively.

Most experimental studies have focused on trying to isolate a certain mechanism, e.g. by creating a device where only one type of polaron is present, but a magnetoresistive response was always observed and no mechanism could be excluded. So far the largest effects have been observed in organic light-emitting materials and devices, where all particle reactions can potentially occur. In order to proactively unravel the underlying mechanism, an exquisite control of the spin carrying particle interactions and subsequent magnetic-field dependent reactions is required. We propose a polymer–fullerene blend as the most suitable candidate. Introducing fullerene to the polymer system enables a detailed control of the particle and spin interactions and provides a novel method to investigate the different mechanisms. At low concentration, the fullerene effectively quenches excitons into weakly bound, spatially separated charge-transfer (CTS) states, thereby reducing the exciton densities.[13,128] At higher concentra-

tion, phase separation additionally leads to separate electron and hole current pathways through the device.[13,129,130] Following earlier suggestions by Wang *et al.*[106] on magnetic field effects in polymer–fullerene blends, we succeeded in fully correlating pronounced changes in the magnetic field effects to the complementary (spin) physics in the different concentration regimes. Using detailed experimental analysis, explicit microscopic and numerical device simulations, we thus unravel the dominant underlying mechanisms of OMAR. In contrast to earlier work, our analysis allows us to quantitatively explain the observed linewidths and sign changes.

Relevant OMAR mechanisms and their fingerprints

A unified picture of the relevant particles and their (spin-dependent) reactions is shown in Fig. 5.1. The left panel shows possible polaron pairs in an organic semiconductor as a function of energy. Free charges can form precursor pairs in a singlet or triplet configuration. From this pair state, the precursor pair can either recombine into a singlet (S) or triplet (T) exciton (in the case of an electron–hole pair), a singlet bipolaron (in the case of a bipolaron pair) or dissociate back into free carriers again. Within the precursor pairs the separation between the two carriers is such that exchange interactions are still negligible, enabling hyperfine field-induced mixing of the singlet and triplet precursor pairs.[81] An external magnetic field suppresses this mixing and thereby changes the transition to the singlet and triplet exciton or bipolaron state. Such a magnetic field effect governed by the hyperfine field strength, typically on the order of milliteslas, is referred to as a low-field effect (LFE). Recently, it has been shown that the LFE can be accompanied by a distinct magnetic field effect at ultra-small field scales (USFE, ≤mT).[87–89]

The magnetic field controlled transitions between S and T precursor pair states can have profound LFEs on the current through the organic semiconductor. Firstly, within the bipolaron mechanism,[68] an external magnetic field will decrease the current by spin blocking, an effect well know from low-temperature transport studies on double quantum dot systems.[131] The bipolaron model treats the scenario where a charge carrier is quasi-stationary trapped at an energetically relatively low lying state. A nearby free carrier, which contributes to the current, has to pass this site by –at least as a temporary intermediate state– forming a doubly occupied site, i.e. a bipolaron. It should be noted that because of the large exchange within the bipolaron state, its formation is spin-dependent. Therefore, it is well possible for a pair of polarons in a singlet-configuration (S) but very unlikely for the triplet (T), as depicted in Fig. 5.1a. Then, if the two carriers in the precursor pair are in a triplet configuration, the current is effectively blocked. At low magnetic fields, the spin blocking is lifted due to the hyperfine fields efficiently mixing the precursor spin states, as indicated by the

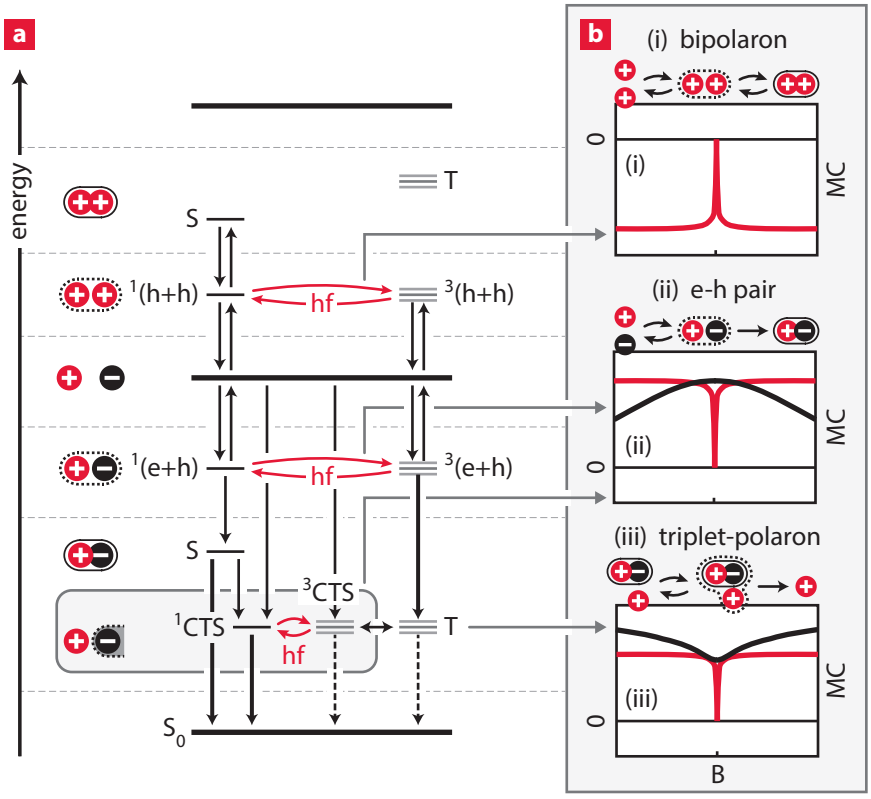

Figure 5.1 | Unified picture of relevant particles and their (spin-dependent) reactions. a | Possible polaron pairs in an organic semiconductor as a function of energy. Free charges can form precursor pairs in a singlet ^{1}( ) or triplet ^{3}( ) configuration. From this pair state, the precursor pair can either recombine into a singlet (S) or triplet (T) exciton (in the case of an electron–hole pair), a singlet bipolaron (in the case of a bipolaron pair) or dissociate back into free carriers again. Due to hyperfine fields (hf), the singlet and triplet precursor pairs can mix and an external magnetic field can suppress this mixing. The magnetic-field dependent transitions between the pair states are indicated with curved arrows. The energy levels and possible mixing mechanisms of a charge-transfer (CTS) state are also included in the diagram. Bipolaron pairs, in this diagram, can also be formed by two electrons. **b |** The characteristic low (red) and high (black) field lineshapes of the (i) bipolaron, (ii) electron–hole and (iii) triplet–polaron mechanism, all according to explicit calculations using a density matrix formalism.

curved arrows in Fig. 5.1a. At high fields, blocking is regained, because random hyperfine fields are overruled, and spin character becomes well-preserved. Thus, the bipolaron mechanism gives rise to a magnetic-field dependence of the charge carrier mobility μ and leads, in this case, to a negative MC.

Next, within the e–h mechanism as proposed by Prigodin *et al.*[69] the crucial reaction is between weakly, coulombically bound, electron–hole precursor pairs as shown in Fig. 5.1a. These pairs form statistically with a ^{1}(e+h):^{3}(e+h) ratio of 1:3. They can dissociate to form free polarons, but can also react to form an exciton from where they finally can recombine to the ground state. If at least one of the two reactions is spin selective, the magnetic field will control the charge balance in the device, and thereby the current. Prigodin *et al.* derived a magnetic field-dependent recombination rate, which was then linked to a so-called recombination mobility μ_r. The authors assumed a different recombination rate for singlets and triplets. So, with less mixing due to a magnetic field, there is less recombination. In the space-charge limited regime, this reduction leads to more current because of compensation of positive and negative space-charge and thus gives rise to a positive MC.[69] In passing we note that generally the e–h mechanism is unlikely to produce large MFEs, since it requires a competition between recombination and dissociation of precursor e–h pairs –that is, e–h pairs that in a single step can form an exciton. Usually, this is highly unlikely, since once the electron and hole have approached each other that close they are well within the Coulomb radius, making dissociation a very unlikely event. However, in organic photovoltaic cells, the e–h pairs are in the form of charge-transfer states, where dissociation does become relatively large[128] and, as we show, the e–h mechanism can result in significant MFEs.

Lastly, we will discuss the triplet–polaron mechanism as first proposed by Desai *et al.*[70] In this model, triplet excitons can react with polarons by scattering events, which effectively reduce the mobility of the free charges and thereby decrease the current through the device. Since triplet excitons in general have a much longer lifetime than singlet excitons, their concentration can become large enough so that these reactions become significant. By applying a magnetic field less triplet excitons are formed, and thereby the current is increased, thus giving rise to a positive MC. We emphasize that even though the current is now influenced by the reaction of triplets with polarons, the LFE arises from the magnetic-field dependent formation of these triplet excitons. Therefore, the hyperfine induced spin mixing of e–h precursor pairs, as indicated in Fig. 5.1a, is a crucial ingredient of the triplet–polaron mechanism.

In addition to the LFEs, so called high-field effects (HFE) occur at field scales much larger than the local hyperfine fields. Within the triplet–polaron mechanism spin mixing occurs between doublets (D) and quartets (Q) of triplet exciton–polaron pairs. Due to the zero-field splitting (ZFS, typically 80 mT[80])

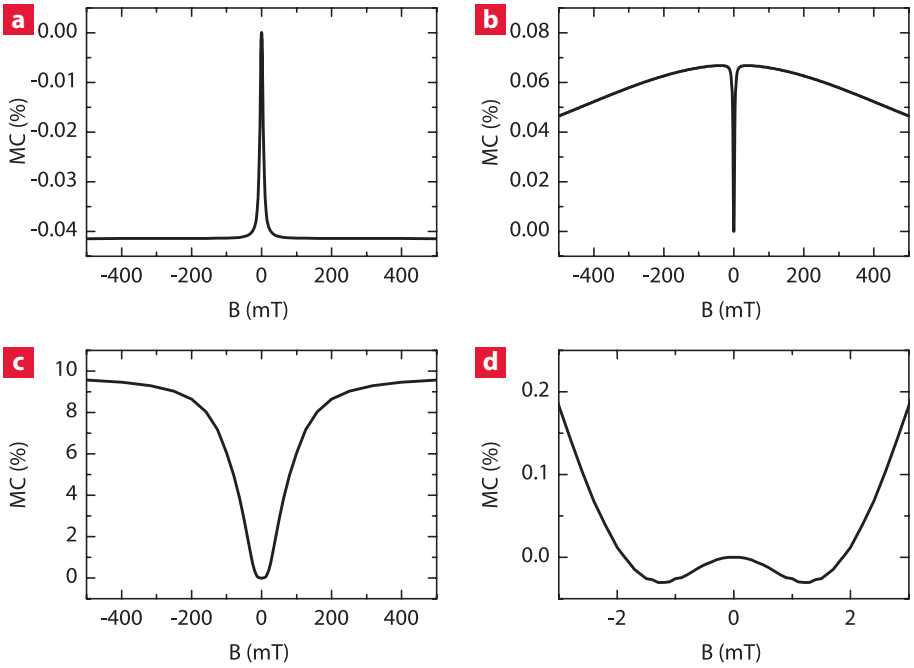

Figure 5.2 | Calculated magnetic field effects on the current as a function of the applied magnetic field for three different mechanisms. a | The bipolaron mechanism. Calculation in the slow-hopping limit using $r_{\alpha\beta} = r_{\varepsilon\alpha} = 1\ s^{-1}$, $r_{\alpha\varepsilon} = 2\ s^{-1}$ and $B_{hf} = 1$ mT. **b |** The e–h mechanism including Δg-mixing. Calculation in the slow-hopping limit using $\Delta g = 0.4\%$, $d = B_{hf} = 1$ mT, $k_T/k_S = 2/3$ and $q/k_S = 10$. **c |** The exciton-charge mechanism. Calculation in the slow-hopping limit using $k_1 = k_{-1} = k_2 = 10\ s^{-1}$, $B_{hf} = 1$ mT, $D_{ZFS} = 100$ mT and $E_{ZFS} = 0$ mT. **d |** Calculation for the e–h mechanism in the intermediate-hopping regime, $r = \omega_{hop}/\omega_{hf} = 1$, clearly displaying the ultra-small-field effect.

of the triplet exciton, the hyperfine field induced spin mixing now manifests itself as a HFE at a broader linewidth. Using the same arguments as for the LFE, this HFE gives rise to a positive MC. The mutual annihilation of triplets also gives rise to a HFE with a linewidth determined by the ZFS.[79] However, since the triplet–triplet mechanism creates free charges, and an increasing magnetic field effectively reduces the amount of available triplets, this leads to a negative MC. A distinctly different HFE displays in the e–h mechanism. The opposite polarons in the e–h pair will generally have a (slightly) different g-factor, leading to dephasing of the precessing electron and hole spins.[81] As a consequence, additional spin mixing occurs at large fields (typically 1 T), referred to as Δg-mechanism. The associated HFE on the current will necessarily have a sign opposite to the corresponding LFE, which is based on the suppression of spin

mixing. All the above mentioned LFE and HFE mechanisms have been explicitly calculated using a density matrix formalism (see Fig. 5.2) and the characteristic resulting MFE lineshapes are depicted in the right panel of Fig. 5.1b. For explicit details on these calculations we refer to the original work of Schellekens *et al.* [79]

In passing we note that other models –based on spin-mixing by hyperfine fields– have been proposed in the literature. These models are mostly different implementations of one of the mechanisms as discussed before. For example, Harmon and Flatté recently proposed a model which is a percolation implementation of the spin-blocking -or bipolaron- mechanism, [75] whereas Hu and Wu combined e-h pair mixing with triplet polaron interactions and included dissociation processes. [104] Besides hyperfine fields, other mixing mechanisms such as spin–orbit coupling have been proposed to explain OMAR. [132,133] However, for the organic materials which consist of low-molecular-weight organic semiconductors, as used in this Chapter, this process is of minor relevance. Finally, completely different mechanisms have been introduced in the literature such as Lorentz-force deflection, hopping magnetoresistance or effects like weak localization and wave function shrinking. [35,134] However, most of them seem no viable candidates to explain the effect, or are not needed to fully explain experimentally observed trends.

Summarizing, the three mechanisms display clear fingerprints, with distinguishable characteristics such as sign and field scale of the LFE and HFE. These characteristics are schematically shown in Fig. 5.1b, and will prove invaluable in identifying the relevant mechanisms.

5.2 Methods

Samples

In this work we studied the magnetic field effects on the current for devices consisting of a blend of poly[(2-methoxy-5-(3,7-dimethyloctyloxy))-1,4-phenylenevinylene] (MDMO-PPV) and [6,6]-phenyl-C_{61}-butyric acid methyl ester (PCBM). The MDMO-PPV was purchased from American Dye Source Inc. and the PCBM (>99% pure) from Solenne B.V. The devices were prepared on glass substrates with patterned indium tin oxide (ITO) anodes. After careful cleaning, followed by a UV-ozone treatment, a thin layer of poly(3,4-ethylenedioxythiophene):poly(styrenesulfonate) (PEDOT:PSS) was applied by spin coating. The MDMO-PPV and PCBM were both dissolved in orthodichlorobenzene, with a concentration of 10 mg/ml and 20 mg/ml respectively, and stirred on a hot plate at 50 °C for at least 2 hours after appropriate blending. The blends were spin coated at 1200 rpm for 60 s. Subsequently, the samples were transferred to a nitrogen filled glove box where the cathode, consisting of LiF and Al, was evaporated in a high vacuum system (~10^{-7} mbar). From this point on, the

samples always remain in a dry nitrogen environment. The total junction stack thus consisted of ITO/PEDOT:PSS(60 nm)/[PPV_{1-x}–$PCBM_x$](~80 nm)/LiF(1 nm)/Al(100 nm), with x the PCBM concentration in wt.-%.

Measurements

Magnetic field effect measurements were performed in a cryostat that is attached to a glovebox with a nitrogen environment ([O_2] <0.3 ppm, [H_2O] <0.3 ppm). The cryostat is placed between the poles of an electromagnet. The measurements described in this Chapter were performed at room temperature. The devices were driven at a constant voltage V using a Keithley 2400 Series SourceMeter. We measured the current I through the device while sweeping the magnetic field B. From this measurement, the magnetoconductance (MC) was calculated with $\mathrm{MC}(B) = [I(B) - I(0)]/I(0)$.

Empirical Lineshapes

We have analyzed our experimental results using the following fitting function: $\mathrm{MC}(B) = \mathrm{LFE} \cdot f(B, B_{\mathrm{hf}}, B_{\mathrm{m}}, r) + \mathrm{HFE} \cdot B^2/(|B| + B_{\mathrm{HFE}})^2$, where the function $f(B, B_{\mathrm{hf}}, B_{\mathrm{m}}, r)$ is explained in full detail in Chapter 3 and is used to correctly describe the low-field effect including the ultra-small-field effect as is shown in Fig. 5.4b. This empirical function allows us to separately extract the role of the hyperfine field (B_{hf}) and the additional broadening (B_{m}) induced by the microscopic mechanisms involved. The USFE is incorporated by the parameter r which describes the limit in which hopping of carriers is no longer slow compared to spin precession in the hyperfine fields. The high-field effect is fitted with a so-called non-Lorentzian lineshape. In the fitting procedure, for each specific blend x, the line widths (B_{hf}, B_{m} and B_{HFE}) were shared fit parameters, whereas the magnitudes (LFE and HFE) and the hopping ratio (r) were free fit parameters. In this study, we investigated the amplitudes and line widths. The discussion of the other fitting parameters, although extracted and analyzed, is beyond the scope of the present work.

5.3 Results and discussion

In this study, we used a variety of blends, but most focus will be on blends of MDMO-PPV:PCBM, where PPV acts as hole-conducting polymer and electron donor, whereas PCBM acts as electron acceptor. This blend is a well-known and extensively studied organic photovoltaic system.[13,84,85,90,92,93,129,130,135–137] We will exploit the thorough understanding of the charge transport and morphology of this model system as a basis of our identification.

We have systematically investigated the magnetic field effect on the current (MC) as a function of the applied magnetic field B and the bias voltage V for a

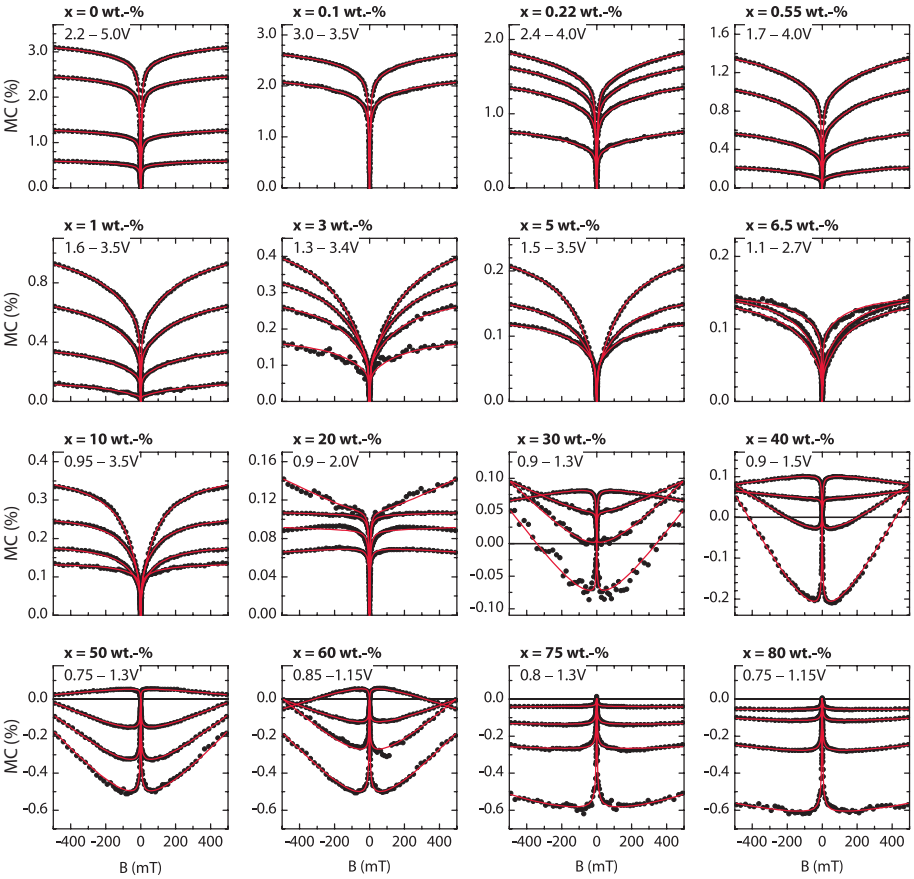

Figure 5.3 | Magnetic field effect on the current (MC) as a function of the applied magnetic field for a broad range of PCBM concentrations. For each distinct blend a few MC(B) curves at different applied bias voltages are shown (solid symbols) and all curves are fitted using the empirical lineshape (solid line, see Sect. 5.2).

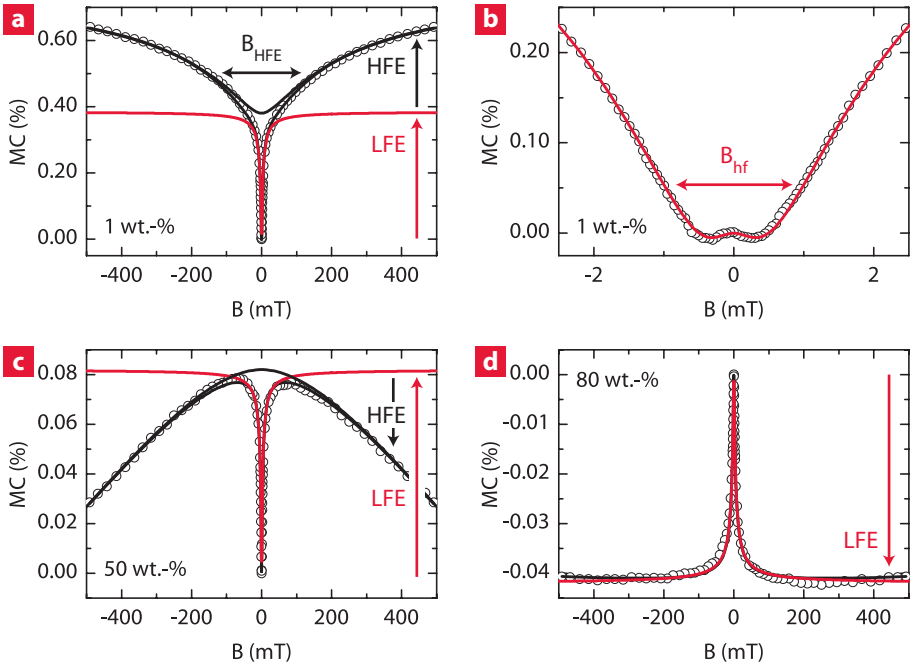

Figure 5.4 | Magnetic field effect on the current as a function of the applied magnetic field for three different blends. a | The MFE for a 1.0 wt.-% MDMO-PPV$_{1-x}$–PCBM$_x$ blend at 3.0 V. The solid line is a fit using the empirical lineshape (see Sect. 5.2), where the low (LFE) and high magnetic field (HFE) contributions are separately depicted. The magnitude of LFE and HFE and their corresponding line widths B_{hf} and B_{HFE} are also shown. **b |** At low magnetic fields, on the order of a millitesla, an ultra-small-field effect (USFE) appears which is also correctly described by the fit. **c |** The MFE for a 50% blend at 1.1 V. Here, the LFE and HFE have a different sign and the line width of the HFE is much broader. **d |** The MFE for a 80% blend at 1.1 V, showing a negative LFE and almost no HFE.

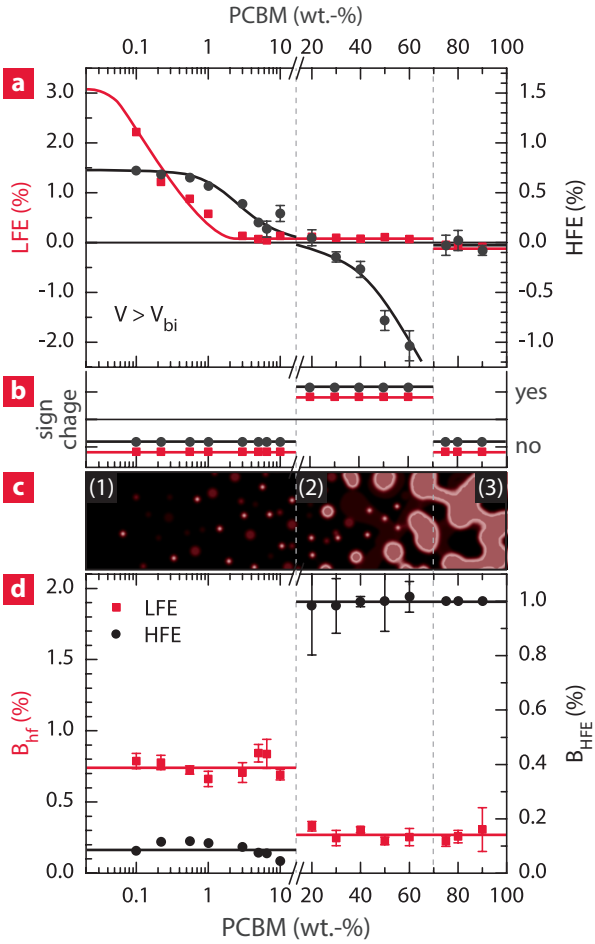

Figure 5.5 | Global trends of the magnetic field effects in the current as a function of PCBM content. a | The top figure shows the maximum value of the magnitude of the magnetoconductance for the low (LFE, left axis, red squares) and high magnetic field effect (HFE, right axis black circles) as a function of PCBM content at voltages higher than the built-in voltage V_{bi}. The lines provide a guide to the eye. **b |** This panel shows if there is a sign change in the MFE as a function of voltage. **c |** An illustration of the morphology of the organic layer with the three distinct regions indicated. **d |** The bottom figure shows the width of the two magnetic field effects (B_{hf} and B_{HFE}).

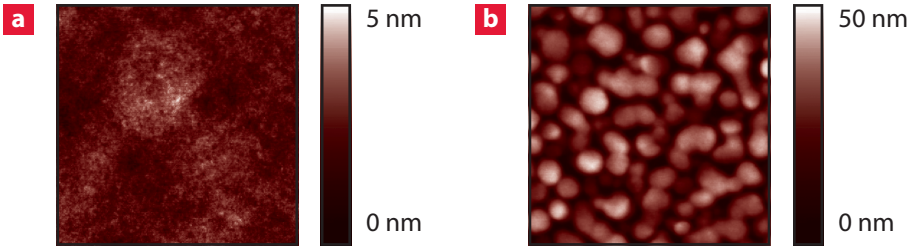

Figure 5.6 | AFM height images of the MDMO-PPV:PCBM blend. a | Surface scan of a blend with 50 wt.-% PCBM showing a smooth surface (roughness < 5 nm). **b |** Surface scan of a 80% device clearly showing the phase separation. The widths of the phase separated domains are on the order of 200 nm. In both cases the scan size is $2 \times 2\ \mu m^2$.

broad range of PCBM concentrations x. Fig. 5.3 shows an extensive overview of our experimental data set. We observed an extremely rich behavior of the magnetic field effect with very pronounced changes in both the amplitudes and line widths. Typical results for three different concentrations x are shown in Fig. 5.4. At low PCBM concentrations (0–10 wt.-%, Fig. 5.4a), we observe a positive LFE, which is accompanied by a positive HFE with a width on the order of 100 mT. The corresponding USFE is shown in Fig. 5.4b. In sharp contrast, at intermediate concentrations (30–60 wt.-%, Fig. 5.4c), a positive LFE and an opposite (negative) HFE at much larger field scale (~1 T) are observed. When increasing the PCBM content over 70%, all MC curves only show a negative LFE and almost no HFE. Based on these fingerprints, we raise the hypothesis that the triplet–polaron, e–h and bipolaron mechanism, respectively, are the dominant underlying mechanisms. This conjecture will be put on more solid ground using quantitative arguments in the remainder of this Chapter.

We performed a quantitative analysis by fitting the MC(B) data at all x and V with a superposition of a LFE (including USFE) and a HFE (see Sect. 5.2 and Chapter 3). Thus, for each measurement, we get an amplitude of the LFE and HFE, but also the intrinsic hyperfine field scale (B_{hf}), as well as the half-width at quarter-height of the HFE (B_{HFE}). Fig. 5.5 shows the extracted parameters. Fig. 5.5a presents the maximum observed magnitude of the LFE and HFE in each specific blend, while the line widths are shown in Fig. 5.5d. In both figures we observe very pronounced trends, which can be correlated with different morphology regimes of the polymer–fullerene blend,[129] schematically represented in Fig. 5.5c.

Initially, at small x, regime (1) in Fig. 5.5c, PCBM will form scattered (clusters of) molecules in the PPV matrix, providing efficient quenching sites for excitons, and introducing charge-transfer states with holes residing on the polymer and

electrons on the PCBM. Beyond x = 20%, regime (2), a percolative network for electron conduction along PCBM molecules forms. Importantly, the electrons remain in intimate contact with holes in the PPV matrix. When increasing x beyond 70%, regime (3), phase separation occurs, creating separate regions dominated by single-carrier electron and hole currents. The exact concentration at which this happens for our blends is known from the literature, but has been verified by means of (tapping mode) atomic force microscopy (AFM). It has been shown that the topology observed in AFM scans can be related to the actual morphology in the blend.[129] Devices up to 60 wt.-% PCBM show a relatively smooth surface, indicating a homogeneous mixture of PPV and PCBM, as shown in Fig. 5.6a. However, at higher PCBM concentrations, a clear domain structure can be observed, as shown in Fig. 5.6b. These large domains, in our case approximately 100 – 200 nm, indicate phase separation in the device. Very interestingly, pronounced changes in Fig. 5.5a and d, such as sign changes and abrupt changes in line widths, exactly correlate with boundaries between the three morphology regimes.

We start our discussion with regime (1). In the pristine polymer, triplet exciton densities can be very high due to the long triplet lifetime, making the triplet–polaron mechanism a likely candidate. The positive sign of the LFE and the width of the HFE (~80 mT), a typical value for the ZFS,[80] is consistent with this interpretation. Very remarkably, we observe that the magnitude of both the LFE and HFE are quenched by adding just a few wt.-% PCBM, consistent with PCBM acting as an efficient quencher of excitons. Note that the LFE responds more sensitively to adding PCBM, which can be assigned to the relative alignment of CTS and triplet exciton energy (see Appendix 5.A).

Next, we will discuss regime (2). In these blends, PCBM is still homogeneously distributed throughout the PPV, but forms percolative current paths for electrons.[129] Excitons are effectively quenched and transferred into CTS pairs, which in our blend are known to be energetically aligned with the triplet excitons on the PPV (Fig. 5.1a).[136,137] This would provide an ideal scenario for an electron (on PCBM) - hole (on PPV) pair mediated mechanism, for which it is necessary that there is a finite chance for e–h pair formation as well as dissociation. Indeed, the observation of a sign change to a negative HFE, as well as an abrupt change to a large field scale due to a Δg-mechanism when entering regime (2) corroborates this assignment. The field scale of approximately 1 T agrees with the field scale we calculated based on experimental values of g_e=1.9995 and g_h=2.0028.[84,85,135] Even more excitingly, a sudden and significant reduction of B_{hf}, as extracted from the LFE, can be witnessed. This is naturally explained by the very small hyperfine field coupling that electrons experience on the fullerene cages due to the vanishing nuclear magnetic moment of ^{12}C.

Finally, in regime (3) the blends are separated into two phases. The electrons are primarily transported through a PCBM phase and the holes through a mixed phase of PPV and PCBM.[129,130] With separate current paths for electrons and holes, locally the device will perform as a single carrier device. Thus, the bipolaron mechanism, the only mechanism not relying on charge carriers with opposite charges, is expected to become dominant over the e–h mechanism in phase-separated blends. Indeed, we observe the LFE changing to a negative value and we observe a quenching of the HFE caused by the Δg-mechanism.

Voltage dependence

After this satisfactory identification of the dominant mechanisms in all three regimes, we show that we can also quantitatively describe the voltage dependence and that specific features herein are in full agreement with our assignment. As such, this provides an alternative route towards unraveling underlying mechanisms. In order to do so, we performed finite element drift-diffusion simulations[90–93] for realistic parameters (please refer to Appendix 5.B for more details). Here, we will briefly discuss the MC(V) in all three regimes, starting with regime (2).

In Fig. 5.5b it is displayed whether at a certain x, a sign change in MC(V) is observed in LFE and HFE. Apparently, regime (2), dominated by the e–h mechanism, is a special regime, where experiments on both the LFE and HFE show a sign change. The experimental LFE(V) and current density, $J(V)$, are plotted in Fig. 5.7b and 5.7d, respectively. Thereby it gets clear that the sign change in the LFE occurs around the built-in voltage V_{bi}, where the current undergoes a transition from the (exponential) diode-like diffusion regime to the (power law) space-charge limited (SCL) drift regime.[13]

We can provide an intuitive explanation for the sign change. In the drift regime, enhancing recombination by applying a magnetic field reduces space-charge compensation of the electron and hole currents and hence reduces the current of bipolar SCL devices, whereas in the diffusion regime carriers recombining in the depletion zone of the diode enhance the current. To quantify this prediction, we performed simulations for devices consisting of homogeneous blends of the polymer and fullerene. The calculated current density, as shown in Fig. 5.7d, matches the experimental result using realistic parameters.[92,93] We also explicitly calculated the magnetic field effects by assuming a change in the recombination mobility μ_r, or hole mobility μ_p. The results of these simulations are depicted in Fig. 5.7b. Here, it is clear that the sign change around V_{bi} is readily reproduced in the case of a change in recombination mobility, strengthening our conclusion that the e–h mechanism is dominant in this regime.

In regime (3) a rather similar dependence of the LFE is observed (Fig. 5.7c), however, without the characteristic sign change. Explicit simulations show that

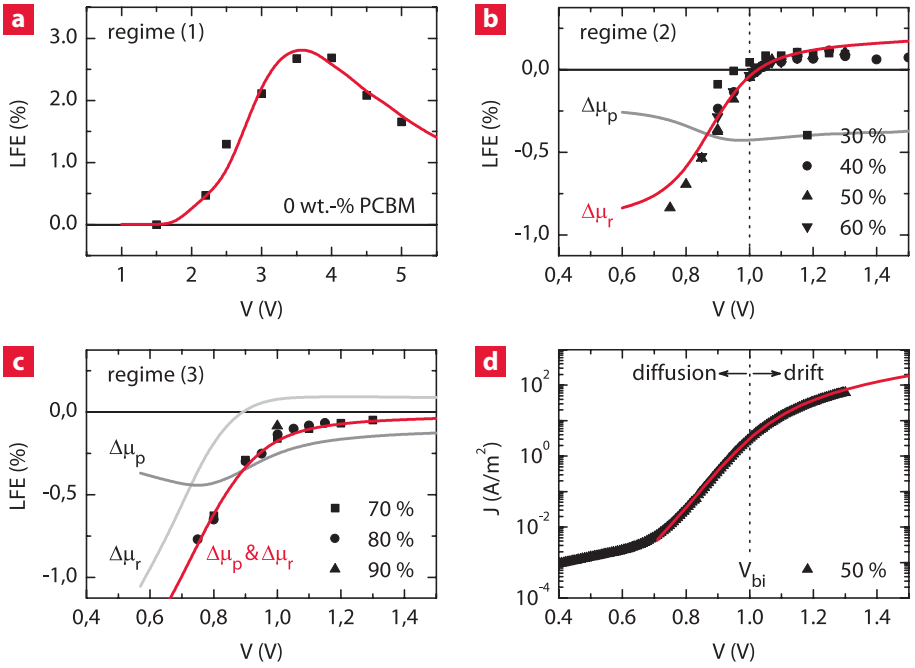

Figure 5.7 | Experimental and simulated voltage dependencies. Experimental (symbols) and simulated (solid line) low-field effect as a function of voltage for **a |** pristine devices, **b |** homogenous mixed blends in regime (2) and **c |** the phase separated blends in regime (3). **d |** Experimental (symbols) and simulated (solid line) current density as a function of voltage for a 50 wt.-% blend showing a transition from a diffusion to drift dominated regime around the built-in voltage.

this can be traced back to the superposition of an almost constant and negative MC(V) due to the bipolaron mechanism (realized by a change in carrier mobility μ_p) and a finite contribution from the e–h mechanism (change in recombination mobility μ_r). The latter contribution is most probably related to the interaction of electrons and holes at the interface between the two phases in the blend, an effect which our device simulations take into account.[92,93] We have experimentally verified this assumption by creating devices with unbalanced charge injection. By changing the electron injecting contact, we are able to reduce the density of the electrons and thereby reduce the contribution of the e–h mechanism. Please refer to Appendix 5.C for more details and the experimental results.

Also regime (1) shows a very characteristic MC(V) dependence (Fig. 5.7a), vanishing below the built-in voltage and peaking somewhat above. A full description of those dependencies goes beyond the scope of our present Chapter, but more information on the calculation is provided in the Appendix. Here,

we will briefly discuss these recent advances, where trap states play an important role. We found that we can numerically simulate the MC(V) trend with a trapped triplet–polaron mechanism, as is shown in Fig. 5.7a. This mechanism involves the spin-dependent formation of triplet excitons at trap sites and their subsequent reaction with free polarons. A magnetic field will reduce the number of triplets and thereby enhance the number of free polarons. The initial increase of the MC(V) then simply stems from the increase of triplet density with voltage, while the eventual decrease arises from the fact that there is only a limited number of traps available in a device.

Finally, as an outlook, we conjecture that by choosing the right materials to alter the alignment of triplet excitons and CTS or intentionally introducing specific trap sites,[118,138] huge effects on the reaction pathways and the resulting OMAR can be achieved. As an example of the former, we are currently investigating different polymer–fullerene blends and observe that even subtle changes give rise to additional, distinctly different low-field contributions. The insights obtained in our present work seem invaluable in understanding these novel magnetic field effects.

5.4 Conclusion

Concluding, in this Chapter we presented a proof of concept study, unraveling the role of the relevant particle pairs and their reactions for OMAR. Furthermore, we explained how striking differences in the magnetic field effect lineshapes are correlated with the underlying microscopic mechanisms and have shown the important role of device physics. Our findings open up unprecedented means to bring OMAR research from a phase of passively observing magnetic field effects in the current, to really engineering device characteristics by tailoring the molecular system.

Appendix 5.A
Quenching of the LFE and HFE when adding PCBM

We identified the exciton-charge mechanism as the dominant mechanism for the observed magnetic field effects in the first regime ($0 \leq x \leq 10$ wt.-%). Here, the magnitude of both the LFE and HFE are quenched by adding a few wt.-% PCBM, however the LFE responds more sensitively than the HFE to adding PCBM. We will explain this by examining the possible spin-dependent polaron pair interactions as illustrated in Fig. 5.1a. In explaining, we will subdivide the first regime in Fig. 5.5 into three parts: (a) the pristine polymer, (b) the region where the LFE is quenched (0.1 ~ 1 wt.-%) and (c) a region where also the HFE is quenched ($\geq$ 1 wt.-%).

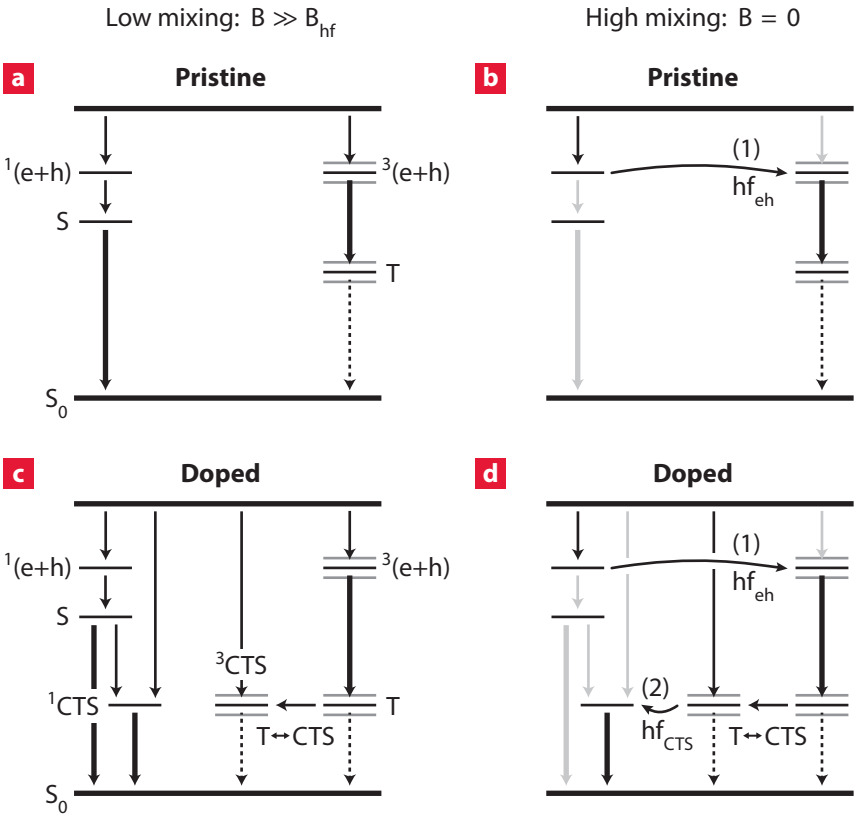

Figure 5.8 | Fastest relevant recombination routes. a | Pristine polymer with a large external applied magnetic field. **b |** Pristine polymer in the absence of an external magnetic field. **c |** Low PCBM concentration with a large external magnetic field. **d |** Low PCBM concentration in the absence of an external magnetic field.

Regime 1a:

First, we discuss the effects in the pristine polymer ($x \sim 0$ wt.-%). Here, the magnetic field reduces the hyperfine induced mixing between the singlet and triplet electron–hole pairs, as depicted in Fig. 5.8a. In the absence of a magnetic field, the spin mixing increases the number of triplet excitons due to a larger triplet exciton formation rate than that of singlets.[89] These triplet excitons can decrease the current by scattering the free charge carriers. Reducing the triplet formation by applying an external magnetic field thus reduces the scattering and thereby increases the total current, leading to a positive MC.

Regime 1b

Next, we discuss the effects of adding a small concentration PCBM ($0.1 < x < 1$ wt.-%). By doping the polymer with PCBM we introduce additional low-energy states which are called charge-transfer state, as depicted in Fig. 5.8c and d. The CTS is basically an electron–hole pair where the hole resides on the polymer and the electron on the PCBM molecule. Since the CTS is significantly lower in energy than the singlet exciton in PPV, it quenches singlet excitons into a charge-transfer state in the singlet configuration (^{1}CTS). In MDMO-PPV:PCBM blends the CTS has approximately the same energy as the triplet exciton in MDMO-PPV. Therefore, a charge-transfer state in the triplet configuration (^{3}CTS) can transfer its electron back into PPV, forming a triplet exciton in the polymer and vice versa. The CTS thereby adds an additional path to create (and quench) triplet excitons. Because the CTS is still spatially separated spin mixing via hyperfine interactions takes place similar to the electron–hole pairs.

We can now explain the reduction in the LFE by the addition of a small concentration PCBM. In the case of a large external applied magnetic field, hyperfine induced mixing is reduced and there is an equilibrium between the triplet exciton and triplet CTS, as depicted in Fig. 5.8c. Without a magnetic field, however, singlet and triplet precursor pairs will mix and will follow the same route to the triplet exciton as in the case without PCBM, causing an increase in the number of triplet excitons. But, in the absence of a magnetic field, CTSs can also mix, resulting in a decrease in triplet CTSs. Since the triplet CTS has approximately the same energy as the triplet state in the polymer, this leads to a decrease in triplet excitons and thereby a decrease in the magnetic field effects caused by triplet–polaron interactions. Summarizing, if we now increase the magnetic field, we observe a smaller change in triplet population in the polymer and thereby a smaller low-field magnetic field effect. Since the CTS does not affect the reaction between the triplet excitons and charges, we do not observe any changes in the HFE yet.

Regime 1c

Finally, we explain the last region where also the HFE is quenched ($1 < x < 10$ wt.-%). We conjecture that the reduction in the HFE is caused by the occurrence of transport of electrons between traps in the polymer and PCBM sites. While the percolation limit for electron transport completely via PCBM sites has not yet been reached (this happens at the transition from regime (1) to (2), i.e. between 10 and 20 wt.-%), it has been reported that electrons in deep lying PPV trap states can hop through the device via local PCBM states which are at approximately the same energy. The same channel of electron conduction has been conjectured to explain the observed increase in current upon adding a few percent PCBM on

these devices.[129] The exact effect of this additional electron current on the HFE is difficult to predict, but there are several mechanisms possible that could give rise to a lowering of the HFE in this regime. As an example, it has recently been shown that traps can significantly enhance the OMAR effect.[118] Therefore, by effectively detrapping the electrons we can expect a reduction of both magnetic field effects which we indeed observe. A more detailed interpretation of the role of traps on magnetic field effects is beyond the scope of this Chapter.

Appendix 5.B
Voltage dependence of the LFE

To further unravel the underlying mechanisms of the magnetic field effects, we performed finite element drift-diffusion simulations for realistic parameters.[91–93]

We simulated the MC(V) in regime (1) using a mechanism which considers the spin-dependent formation of triplet excitons at (electron) trap sites and their subsequent interaction with free polarons. Here we treat the triplet–polaron pair as an additional excitation -thereby temporarily immobilizing the polaron- and we assume it only has a significant lifetime on a trap site. We model the low-field effect as a reduction of the triplet exciton formation chance when it is created from the recombination of a trapped electron and a free hole. A magnetic field will thus reduce the number of triplet excitons and subsequent triplet–polaron pairs and will thereby enhance the number of free polarons. The initial increase of the MC(V) then simply stems from the increase of triplet–polaron reactions with V, while the eventual decrease arises from the fact that there is only a limited number of traps available in a device, and thus a limited number of excitations can be formed. This means that the MC will diminish at high voltages, since the number of free polarons will become much larger than the number of triplet–polaron pairs. The model incorporates the following parameters: the number of electron trap sites N_t (2×10^{-4} /nm^{-3}), the electron trapping coefficient γ_t (2×10^{8} nm^3/s), the hole recombination coefficient with trapped electrons γ_r (1×10^{8} nm^3/s), the triplet formation change P_T (0.25→0.20), the triplet exciton lifetime t_T (6×10^{-5} s), the triplet–polaron interaction coefficient γ_{TP} (1×10^{9} nm^3/s) and the triplet–polaron pair lifetime t_{TP} (1×10^{-3} s). The simulations for pristine devices are performed using the parameters in Table 5.1.

We also performed simulations for regime (2) and (3). Figure 5.9 shows the experimental and simulated voltage dependencies. The current density, $J(V)$, reveals three transport regimes: (i) an ohmic leakage current at the lowest voltages, (ii) a diffusion current in the diode regime below V_{bi}, with a rectifying exponential dependence $J \sim \exp(qV/nk_BT)$ and (iii) a space-charge limited current in the drift regime above the built-in voltage $V_{bi} \approx 1$ V, with a power law

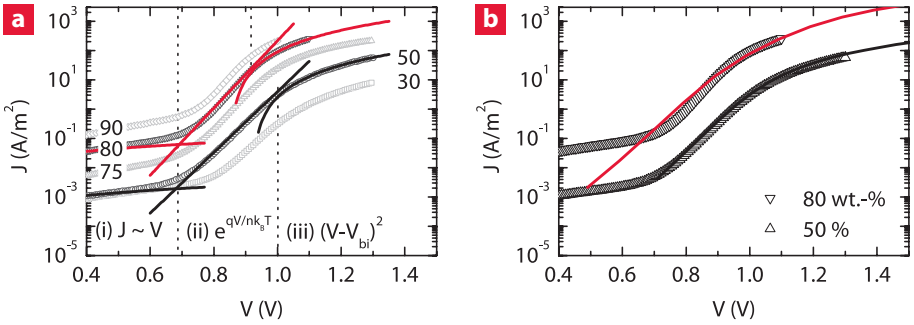

Figure 5.9 | Experimental and simulated voltage dependencies. a | Current density as function of voltage for a few different blends showing transitions from an (i) ohmic leakage current to a (ii) diffusion and finally (iii) drift dominated regime. **b |** Experimental (symbols) and simulated (solid line) $J(V)$ for a 50 and 80 wt.-% blend.

Table 5.1 | Parameters used in the drift-diffusion simulations. For all devices, the workfunctions of the LiF:Al and the PEDOT:PSS contact are set to give rise to ohmic electron and hole contacts respectively.[93]

	Pristine device	**Homogeneous blend**	**Phase separated blend:** Mixed phase	PCBM phase
μ_p (m^2/Vs)	1×10^{-10}	8×10^{-9}	4×10^{-8}	2×10^{-11}
μ_n (m^2/Vs)	2×10^{-9}	2×10^{-9}	2×10^{-10}	3×10^{-7}
ε_r	3.0	3.6	3.6	3.9
g_0 (nm^{-3})	0.3	0.3	0.3	0.3
HOMO (eV)	5.2	5.2	5.2	6.1
LUMO (eV)	2.4	4.1	4.1	4.1

dependence $J \sim (V - V_{bi})^n$ where $n = 2$. The simulations for devices consisting of a homogeneous (50 wt.-%) or phase separated (80 wt.-%) blend are performed using the parameters in Table 5.1. The current density, as shown in Fig. 5.9b, matches the experimental result. The magnetic field effects are calculated by introducing magnetic-field dependent change in the recombination mobility μ_r or hole mobility μ_p.

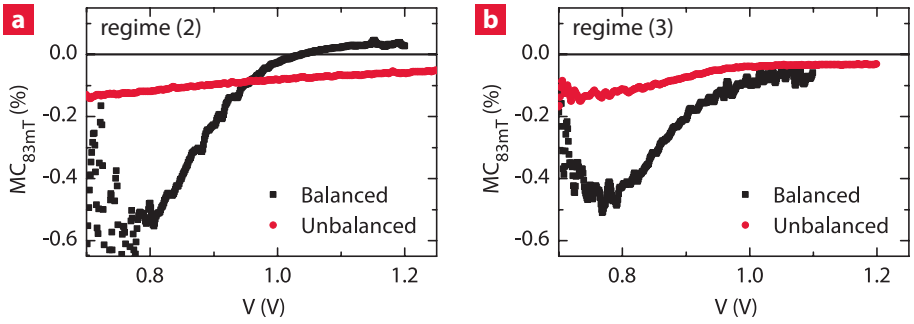

Figure 5.10 | Voltage dependence for balanced and unbalanced devices. In unbalanced devices, we reduced the electron injection by omitting the LiF layer in the cathode. **a |** Homogeneous blend consisting of 60 wt.-% PCBM. **b |** Phase separated blend consisting of 80 wt.-% PCBM.

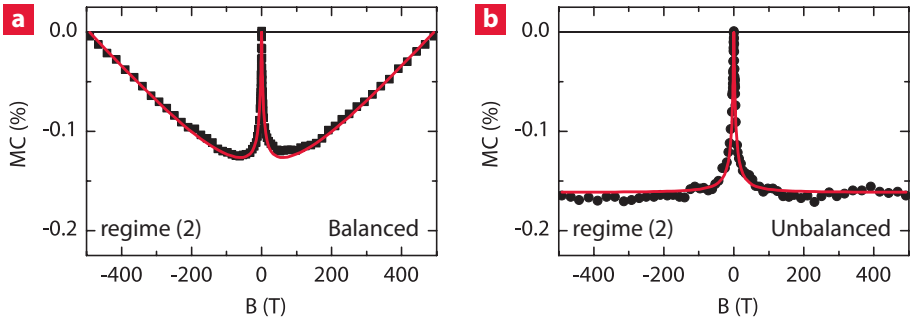

Figure 5.11 | Magnetic field effect for balanced and unbalanced devices. Homogeneous blend consisting of 60 wt.-% PCBM, measured at 0.95 V. **a |** In balanced devices, a negative LFE is accompanied by a clear HFE contribution arising from the Δg-mechanism. **b |** Unbalanced devices do not show this characteristic HFE.

Appendix 5.C
MFEs in unbalanced devices

To investigate the finite contribution of the e–h pair mechanism in phase separated blends, we created devices with unbalanced charge injection. Here, we have altered the electron injecting contact by omitting the LiF layer. This severely limits the electron injection into the organic layer. [139] The results for a 80 wt.-% PCBM device is shown in Fig. 5.10b. We observe an almost complete quenching of the e–h mechanism contribution and measure a small, negative, hardly voltage dependent magnetic field effect. This is in full agreement with the the bipolaron mechanism as simulated in Fig. 5.7

To verify the effect of unbalanced charge injection on the e–h mechanism, we have also created an unbalanced, homogeneously mixed polymer–fullerene device. Figure 5.10a shows the voltage dependence of such a device. Here, the characteristic sign change of the e–h mechanism, resulting from the magnetic field dependence on the recombination mobility, is no longer observed and we measure a small, negative, hardly voltage dependent magnetic field effect again. Moreover, the magnetic field effect lineshape also changes, as shown in Fig. 5.11. In unbalanced devices, we no longer observe the characteristic HFE related to a CTS based Δg-mechanism, as observed in regime (2). This strengthens our conclusion that the e–h mechanism is indeed quenched by unbalancing the charge carrier injection. And, as a consequence, this supports our assignment of the e–h mechanism as dominant underlying mechanism in regime (2). Finally, we want to emphasize that the foregoing exemplifies the major importance of proper device physics in understanding the magnetic field effects on the current.

Investigating the influence of the triplet energy alignment on organic magnetoresistance

6

Recently, it was discovered that the current through an organic semiconductor, sandwiched between two non-magnetic electrodes, can be changed significantly (up to 25%) by applying a small (order of milliteslas) magnetic field. At present, the microscopic mechanisms underlying this so-called organic magnetoresistance (OMAR) are intensively being debated. One of the mechanisms which can successfully describe the magnetic field effects on the current in pristine organic semiconductor devices uses the reactions of triplet excitons and polarons. Here, we present a proof of concept study in which we tune these interactions in the device by deliberately doping our devices with fullerene, creating additional charge-transfer states (CTS). By engineering devices with different energetic alignments of the CTS and triplet exciton, we can influence the triplet exciton density in the device. We correlate pronounced changes in the magnetic field effect magnitude and lineshape to the energy of the CTS with respect to the triplet exciton.[*]

[*]Under review at Organic Electronics as: *Investigating the influence of the triplet energy alignment on organic magnetoresistance.* P. Janssen, S.H.W. Wouters, M. Cox and B. Koopmans.

6.1 Introduction

The discovery of surprisingly large, room temperature, magnetoresistance effects in organic semiconductor devices without any ferromagnetic components has puzzled the young field of organic spintronics during the past decade.[33–35] The effect is often referred to as organic magnetoresistance (OMAR). The possibility to obtain large (up to 25%) changes in the current at room temperature, while applying only small (a few millitesla) magnetic fields, makes this effect interesting for future applications and, moreover, from a scientific point of view. Studying OMAR provides a deeper fundamental understanding of spin-physics and charge transport in organic semiconductor devices.

All contemporary models explaining OMAR rely on magnetic-field dependent reactions of the spin carrying particles, where a magnetic field suppresses the spin mixing of the particle pairs prior to the reaction. There is, however, an active debate about the nature of the particles (e.g. electrons, holes, bipolarons, excitons or trions) and the exact underlying mechanism influencing the current.[68–70,78,79,89,104,106,116] Currently, the possible mechanisms can be divided into two main categories: (i) mechanisms which only need one type of charge carrier or (ii) mechanisms which need both charge carriers. In the first class, the so-called bipolaron mechanism[68] has been successfully applied to explain magnetic field effects in unipolar devices.[67,106,119] In the second class, we can distinguish between models which describe the reactions of polarons with opposite charge into excitons[69] and models which rely on the spin-dependent reactions of triplet excitons with polarons.[70,78] Besides the microscopic models, it is also important to be aware of the highly non-trivial role played by the device physics in order to explain observed magnetic field effects (MFEs) on the current.[91,95] Very recently, we have shown that the dominant mechanism for OMAR depends on the exact material choice and operating conditions of the device[119] and that the MFE in pristine organic semiconductor devices are predominantly governed by the reactions of (trapped) triplet excitons and polarons.[78]

To study the underlying mechanism of triplet–polaron interactions, an exquisite control over the triplet exciton density is desired. In line with earlier work, we propose polymer–fullerene blends as an ideal model system.[106,119] We study the influence of triplet excitons on OMAR by introducing a low concentration of fullerene in the polymer devices. This creates additional charge-transfer states (CTS) by which the number of triplet excitons can be increased, stabilized or decreased, depending on the relative energetic alignment of the CTS with respect to the triplet exciton.[128] Different energetic alignments can be engineered by choosing the right material combinations.[136]

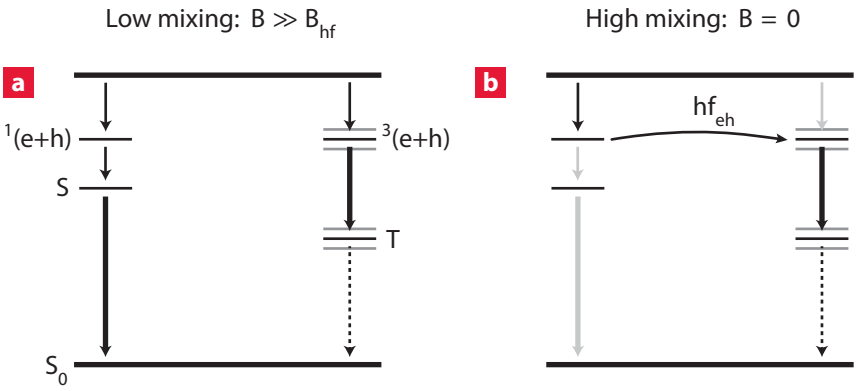

Figure 6.1 | Energy diagram of relevant spin-dependent transitions from free charges to the ground state in a pristine device. a | In a large external applied magnetic field, free charges can form precursor pairs in a singlet $^1(\ )$ or triplet $^3(\ )$ configuration. From this pair state, the precursor pair can recombine into a singlet (S) or triplet (T) exciton. **b |** Without a magnetic field, singlet and triplet precursor pairs can mix due to hyperfine interactions, as indicated by transition hf_{eh}.

6.2 Theory

Magnetic field effects

As introduced in the foregoing, mixing of spin states plays a crucial role in OMAR. In this section we will show how spin mixing can lead to magnetic field effects on the current. We start our discussion with MFEs in pristine polymer devices. Figure 6.1 presents an energy diagram of the relevant spin-dependent transitions from free charges to the ground state. Free charges can form precursor pairs in a singlet $^1(\ )$ or triplet $^3(\ )$ configuration. Within the precursor pairs the separation between the two carriers is such that exchange interactions are still negligible. This enables hyperfine fields, originating from the hydrogen nuclei in the organic material, to mix the singlet and triplet precursor pairs. An external magnetic field suppresses this mixing. From the precursor pair state, the electron–hole pair can recombine into a singlet (S) or triplet (T) exciton and thereafter to the ground state.

In the absence of a magnetic field (Fig. 6.1b), spin mixing increases the number of triplet excitons if the formation rate of triplets is larger than that of singlets.[89] This is indicated by process hf_{eh} in Fig. 6.1b. Triplet excitons can decrease the current by interacting with free charge carriers.[70,78] Increasing the magnetic field (Fig. 6.1a) reduces the triplet formation and thus reduces the triplet–polaron interactions and thereby increases the total current, leading to a positive MC. This magnetic field effect, which is governed by the hyperfine

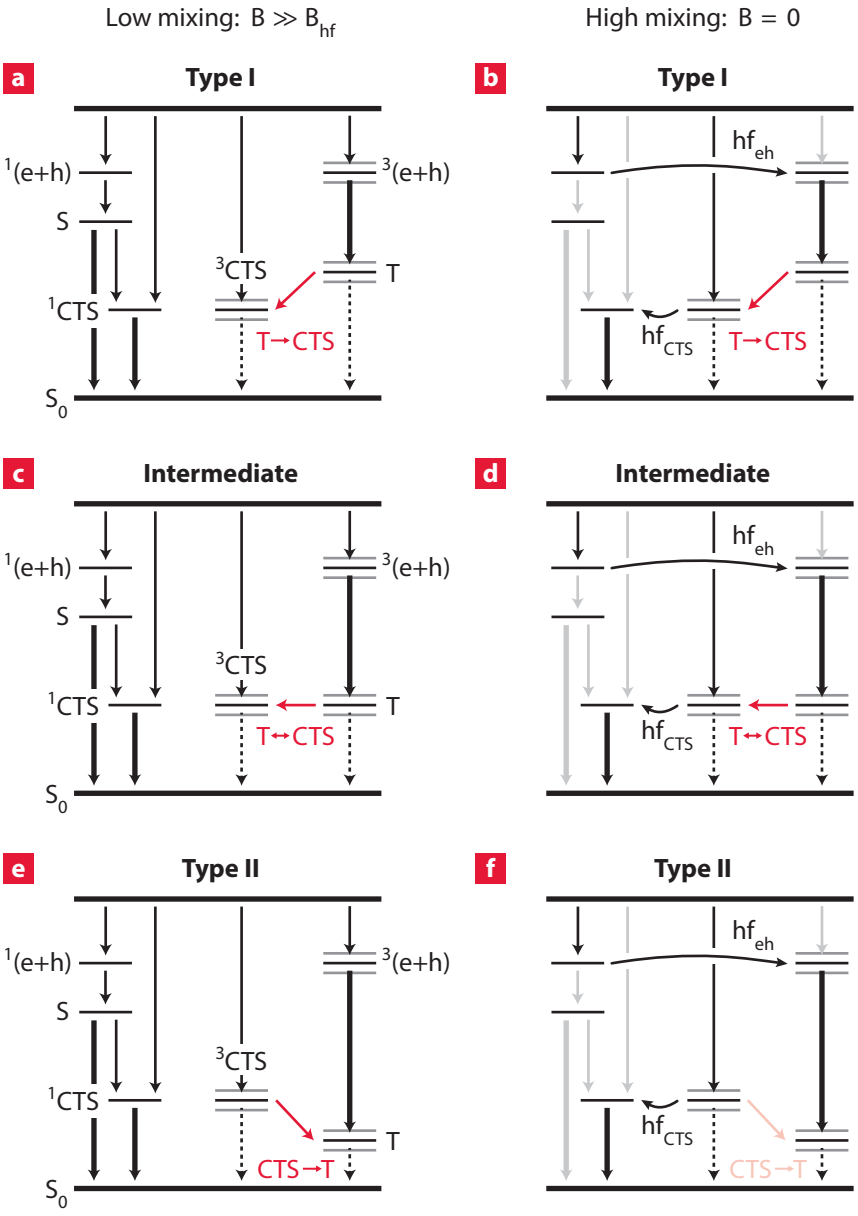

Figure 6.2 | Relevant spin-dependent transitions for devices with different triplet exciton charge-transfer state energy alignments. Three kinds of devices are depicted: **a,b |** the triplet exciton lies higher in energy than the CTS (Type I), **c,d |** both states are energetically aligned or **e,f |** the triplet exciton lies lower in energy than the CTS (Type II). The singlet and triplet CTS can also mix due to hyperfine fields, as indicated by transition hf_{CTS}. The spin-dependent transitions are shown with (left panel) and without (right panel) an external applied magnetic field.

field strength experienced by the precursor pair, will be referred to as a low-field effect (LFE) and has a linewidth of a few millitesla.

The LFE in the pristine polymer device can be accompanied by a distinct magnetic field effect at ultra-small field scales (USFE, typically ≤ mT) as has recently been demonstrated.[87,89] Moreover, the triplet–polaron interaction is also magnetic-field dependent, leading to so-called high-field effects (HFE) occurring at field scales on the order of the zero-field splitting (ZFS, typically 100 mT) of the triplet exciton. When describing the triplet–polaron interactions using a mechanism where (trapped) triplet excitons temporarily capture free polarons into meta-stable trions, as proposed by Cox *et al.*, then this HFE results in a positive MC.

Introducing additional states

To further investigate the underlying mechanism of triplet–polaron interactions, we are going to control the triplet exciton density by introducing additional states in the energy diagram. Hereby, the number of triplet excitons can be increased, stabilized or decreased. As introduced, this can be accomplished by adding fullerene to the polymer devices. At low concentration, the fullerene effectively quenches singlet excitons into weakly bound, spatially separated charge-transfer states, where the hole resides on the polymer and the electron on the fullerene. The effect of fullerene on the triplet excitons depends on the energetic alignment of the CTS and triplet exciton, where three different kinds of devices can be distinguished.

First, in device type I, where the triplet exciton lies higher in energy than the CTS, the triplet exciton will also be effectively transferred into a CTS in a triplet configuration, as depicted by process T→CTS in the top panel of Fig. 6.2. When both states are energetically aligned, the CTS and triplet exciton are in equilibrium and an increase in the number of triplet excitons will be stabilized by the CTS, as indicated by process T↔CTS in the middle panel of Fig. 6.2. Finally, in device type II, the triplet exciton lies lower in energy than the CTS and the number of triplet excitons can increase by a back-transfer from the triplet CTS, as shown by process CTS→T in bottom panel of Fig. 6.2.

The introduction of a CTS can have profound effects on the MFEs, since the number of triplet excitons, ultimately responsible for the magnetic field effect on the current, can be changed significantly in this manner. We will now briefly explain the MFEs. In device type I, CTS decrease the number of triplet excitons in the device by process T→CTS and this reduction is independent of the magnetic field. As a result, introducing CTS in device type I leads to a reduction of the MFE. In the intermediate case, the increase in the number of triplet excitons by process hf_{eh} is diminished by process T↔CTS, also leading

to a reduction in the MFE. Finally, type II devices will show a distinctly different behavior when introducing CTS.

The CTS is basically an electron–hole pair on two different molecules and therefore the singlet and triplet CTS can also undergo mixing due to hyperfine fields, as indicated by process hf_{CTS} in Fig. 6.2. In the absence of a magnetic field, (Fig. 6.2f), spin mixing of CTS decreases the number of triplet CTS back-transferred to triplet excitons if the singlet CTS recombination rate is larger than the back-transfer rate. Increasing the magnetic field leads to an increase of the number of triplet excitons as indicated by process CTS→T in Fig. 6.2e. Thus, increasing the magnetic fields leads to more triplet–polaron interactions and thereby a decrease in the total current, resulting in a negative MC. This magnetic field effect is governed by the hyperfine field strength experienced by CTS ($B_{hf,CTS}$) rather than the electron–hole pair ($B_{hf,eh}$). This field strength will be significantly lower as a result of the very small hyperfine field coupling that electrons experience on the fullerene sites due to the vanishing nuclear magnetic moment of ^{12}C. [119] Thus, type II devices can give rise to two opposing MFEs with distinctly different linewidths.

In summary, the introduction of additional states, whereby the triplet exciton density can be influenced, could be a valuable tool to study triplet–polaron interactions unraveling their role in OMAR.

6.3 Methods

Materials

In this work we studied the magnetic field effects on the current for devices consisting of different polymer–fullerene blends. We used a variety of blends, but this study will focus on blends consisting of poly[(2-methoxy-5-(3,7-dimethyloctyloxy))-1,4-phenylenevinylene] (MDMO-PPV) and a phenyl substituted poly(1,4-phenylenevinylene) semiconducting polymer called Super Yellow PPV (SY-PPV). Both polymers were blended with [6,6]-phenyl-C_{61}-butyric acid methyl ester (PCBM) in different concentrations. In these devices, PPV acts as hole-conducting polymer and electron donor, whereas PCBM acts as electron acceptor and this blend is a well-known and extensively studied organic photovoltaic system. [13] The MDMO-PPV was purchased from American Dye Source Inc., the SY-PPV from Merck and the PCBM from Solenne B.V. and all materials were used as received.

Device fabrication

The devices were prepared on glass substrates with patterned indium tin oxide (ITO) anodes. After careful cleaning, followed by a UV-ozone treatment,

a thin layer of poly(3,4-ethylenedioxythipophene):poly(styrenesulfonate) (PEDOT:PSS) was applied by spin coating. The MDMO-PPV, SY-PPV and PCBM were dissolved in orthodichlorobenzene, with a concentration of 10, 8 and 20 mg/ml respectively, and stirred on a hot plate at 50 °C for at least 2 hours after appropriate blending. The blends were spin coated at 1200 rpm for 60 s. Subsequently, the samples were transferred to a nitrogen filled glove box where the cathode, consisting of LiF and Al, was evaporated in a high vacuum system (~10^{-7} mbar). From this point on, the samples always remain in a dry nitrogen environment. The total junction stack thus consisted of ITO/PEDOT:PSS(60 nm)/blend(~80 nm)/LiF(1 nm)/Al(100 nm), where the blend is either MDMO-$PPV_{(1-x)}$:$PCBM_x$ or SY-$PPV_{(1-x)}$:$PCBM_x$ and with x the PCBM concentration in wt.-%.

Measurements

Magnetic field effect measurements were performed in a cryostat that is attached to a glovebox with a dry nitrogen environment ($[O_2] < 0.3$ ppm, $[H_2O] < 0.3$ ppm). The cryostat is placed between the poles of an electromagnet, which allows us to apply an external magnetic field up to 0.5 T, with an accuracy of 50 μT. The devices were driven at a constant voltage V using a Keithley 2400 Series SourceMeter. We measured the current I through the device while sweeping the magnetic field B. From this measurement, the magnetoconductance (MC) was calculated with $\mathrm{MC}(B) = [I(B) - I(0)]/I(0)$.

Empirical lineshapes

To analyze the magnetoconductance, we used the following fitting function:

$$\begin{aligned}\mathrm{MC}(B) = {} & \mathrm{LFE} \cdot f(B, B_{\mathrm{LFE}}, B_{\mathrm{m}}, r) \\ & + \mathrm{HFE} \cdot B^2/(|B| + B_{\mathrm{HFE}})^2 \\ & + \mathrm{CTS} \cdot f(B, B_{\mathrm{CTS}}, B_{\mathrm{m}}, r)\end{aligned} \tag{6.1}$$

The function $f(B, B_{\mathrm{LFE}}, B_{\mathrm{m}}, r)$, with $f(B = 0) = 0$ and $f(B = \infty) = 1$, is explained in full detail in Chapter 3. The function correctly describes the low-field effect (LFE), including the ultra-small-field effect, in pristine polymer devices, as is shown in the right panel of Fig. 6.3a. This empirical function allows us to separately extract the role of the intrinsic hyperfine field (B_{LFE}) and the extrinsic additional broadening (B_{m}) induced by the microscopic mechanism. The function converges to a Lorentzian lineshape for $f(B_{\mathrm{m}} = 0)$ and a so-called non-Lorentzian for $f(B_{\mathrm{m}} \gg 0)$. The USFE is incorporated by the parameter r which describes the limit in which hopping of carriers is no longer slow compared to spin precession in the hyperfine fields. The accompanying high-field

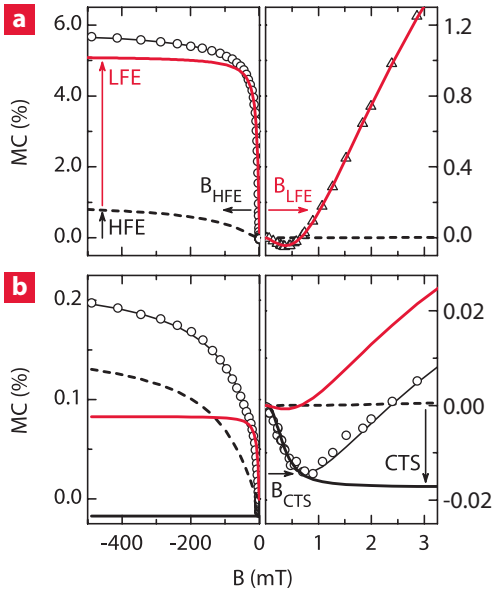

Figure 6.3 | Magnetoconductance as a function of magnetic field. a | Experimental result at a bias voltage of 3.0 V for a pristine SY-PPV device. The solid line is a fit using the empirical lineshape, where the low (LFE) and high magnetic field (HFE) contributions are separately depicted. The magnitude of LFE and HFE and their corresponding linewidth parameters (B_{LFE} and B_{HFE}) are also shown. **b |** Magnetoconductance for a 1 wt.-% doped SY-PPV device at 3.0 V. The MC clearly shows an additional low-field contribution, which is included in Eq. (6.1) with an amplitude CTS and linewidth B_{CTS}.

effect (HFE), depicted in the left panel of Fig. 6.3a, is fitted with non-Lorentzian lineshape and has a characteristic linewidth B_{HFE}. Given the similarity of the magnetic field effect induced by charge-transfer states compared to the LFE, we will use the same empirical function f, but using a necessarily different hyperfine field parameter (B_{CTS}).

In the fitting procedure, to reduce the number of fitting parameters, the intrinsic hyperfine strength (B_{LFE}), extrinsic additional broadening (B_{m}) and the USFE parameter (r) are determined for the pristine polymer devices and these values are then used for the doped devices. The intrinsic hyperfine strength of the CTS (B_{CTS}) and the high-field effect linewidth (B_{HFE}) are determined in a global fit. The amplitudes of the magnetic field effects (LFE, HFE and CTS) can vary with composition and voltage.

6.4 Results and discussion

Magnetic field effects

To investigate the influence of additional states on magnetic field effects in the current, we have systematically measured the magnetoconductance as a function of magnetic field B, bias voltage V and PCBM concentrations x for two different polymer–fullerene blends. Typical results for three different concentrations x are shown in Fig. 6.4 and 6.5 for MDMO and SY blends, respectively. Both pristine devices (Fig. 6.4a,b and 6.5a,b), show a similar lineshape with a positive LFE accompanied by a positive HFE and a USFE. When increasing the PCBM content, we observe a drastic decrease in amplitude of the MFEs. Although the LFE and HFE still show a similar shape for both polymers (Fig. 6.4c,e and 6.5c,e), the lineshape around zero applied field is completely different, as is clearly visible in Fig. 6.4d,f and 6.5d,f. We conjecture that the drastic decrease in amplitude as well as the remarkable differences in lineshape around zero applied field are caused by the introduction of CTS and their energetic alignment with respect to the triplet exciton in the polymer host. This conjecture will be put on more solid ground in the remainder of this Chapter.

Lineshapes analysis

We performed a quantitative analysis by fitting the MC(B) data for all compositions and voltages with a superposition of a LFE (including USFE), a HFE and a contribution from the CTS (refer to the Methods section for a complete description). Thus, for each measurement, we get an amplitude of the LFE, HFE and CTS, and also the intrinsic hyperfine field scales (B_{LFE} and B_{CTS}), as well as the linewidth of the HFE (B_{HFE}). The extracted parameters are shown in Fig. 6.6. Figure 6.6a and b present the amplitude of the MFEs in MDMO and SY blends respectively, while the linewidths are shown in Fig. 6.6c and d. We observe pronounced trends in the amplitudes of the MFEs, whereas the linewidths are approximately constant over the whole doping range (B_{LFE} = 0.85±0.10 mT, B_{HFE} =70±25 mT and B_{CTS} = 0.45±0.05 mT). We previously stated that triplet–polaron interactions are the dominant underlying mechanism for the magnetic field effects in the current in our devices. The positive sign of the LFE and HFE, and the corresponding linewidths are consistent with this interpretation.

Effect of additional states

We will continue our discussion by examining the triplet exciton–CTS alignment. In both polymer–fullerene blends, the magnetic field effects caused by triplet–polaron interactions (LFE, HFE) are quenched by more than an order of magnitude by adding only a few wt-% PCBM. However, in the SY-PPV blends,

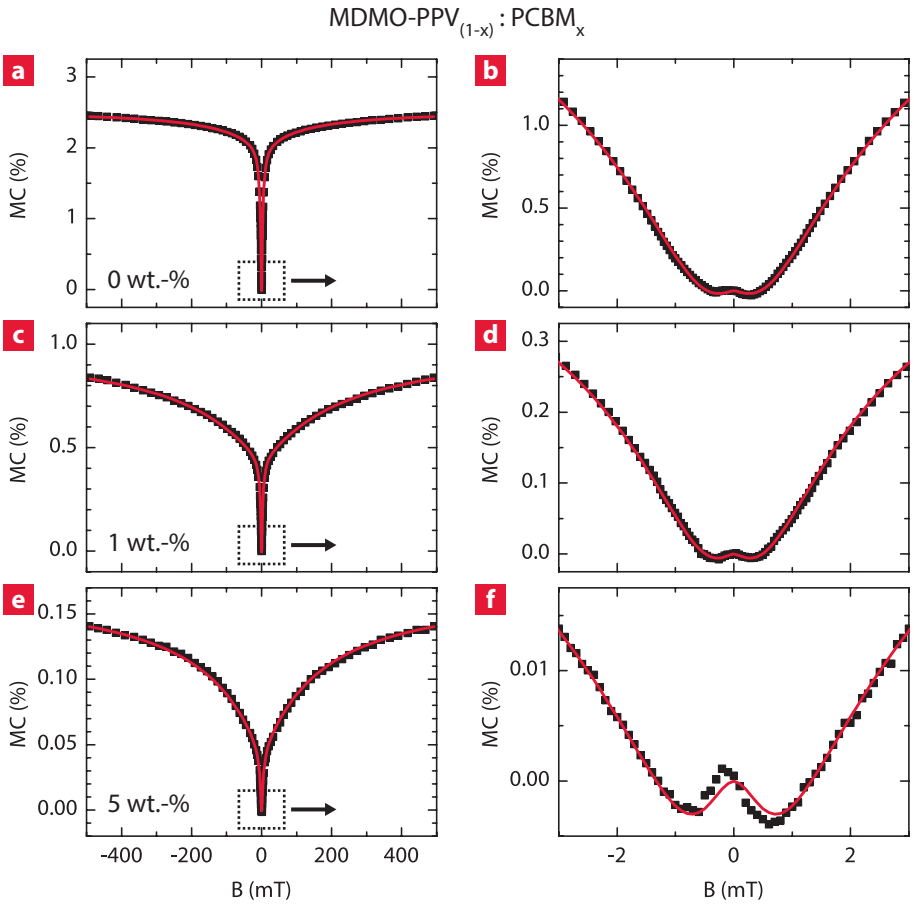

Figure 6.4 | Magnetoconductance as a function of magnetic field. Experimental result at a bias voltage of 3.0 V for **a,b |** a pristine, **c,d |** 1 wt.-% doped and **e,f |** 5 wt.-% doped MDMO-PPV device. The solid line is a fit using Eq. (6.1). The right panels show a zoom around zero applied field.

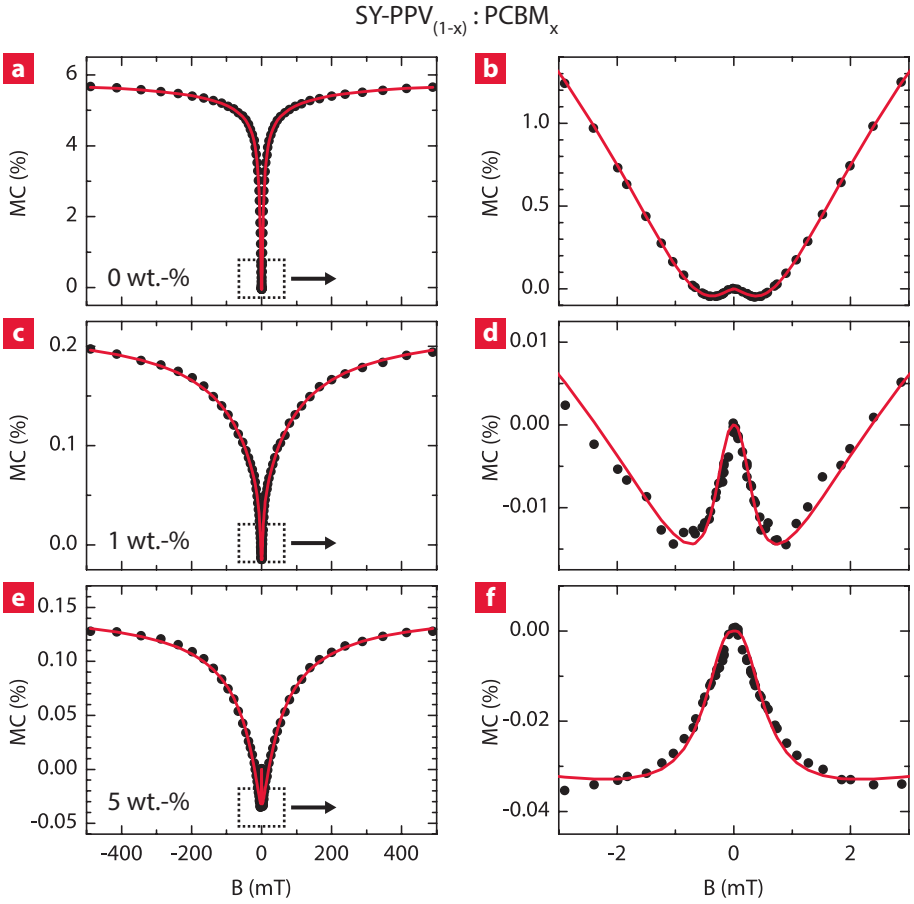

Figure 6.5 | Magnetoconductance as a function of magnetic field. Experimental result at a bias voltage of 3.0 V for **a,b |** a pristine, **c,d |** 1 wt.-% doped and **e,f |** 5 wt.-% doped MDMO-PPV device. The solid line is a fit using Eq. (6.1). The right panels show a zoom around zero applied field.

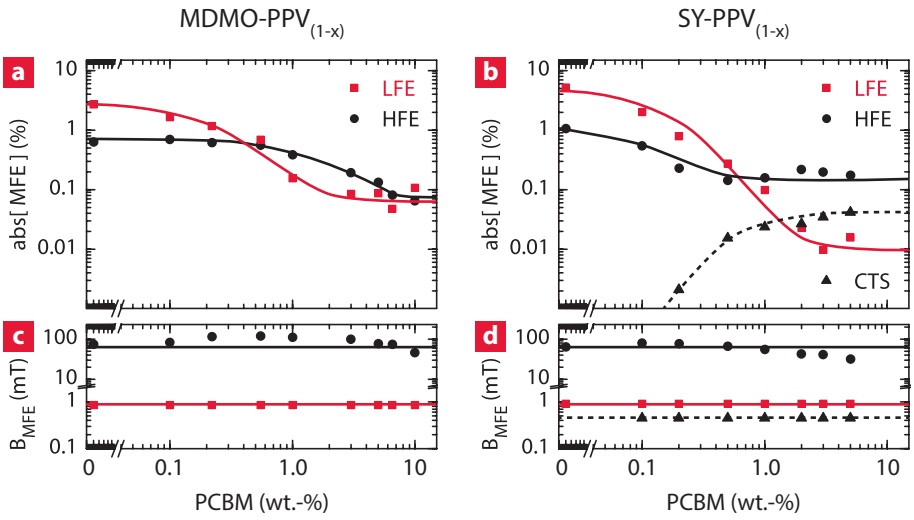

Figure 6.6 | Global trends of the magnetic field effects in the current as a function of PCBM content. The left panels show the results for the MDMO-PPV device and the right panels the SY-PPV device. The top panels show the amplitude of the magnetic field effects, whereas the bottom panels indicate the corresponding linewidths. The lines provide a guide to the eye.

an additional MFE contribution arises when the PCBM concentration is increased. This contribution has the opposite sign as the LFE and the linewidth is significantly smaller. We therefore attribute this MFE to the CTS and assign the SY blend as type II, where the triplet exciton lies lower in energy than the CTS. The absence of an additional MFE caused by the CTS in MDMO-PPV blends, gives rise to a classification as type I. To confirm this hypothesis, we need to know the exact energy levels. However, only few reports about the energy alignments of CTS and triplet excitons in low (≤20 wt.-%) concentration polymer–fullerene blends are available in the literature.[129,137,140] Triplet energies in conjugated polymers, however, have been studied intensively.[141–143] From the literature, we can conclude that the triplet exciton and CTS in MDMO-PPV:PCBM blends are approximately aligned (1.40 eV[136] and 1.40–1.55 eV[129,137] respectively), whereas the triplet energy in SY-PPV lies slightly lower in energy (1.30 eV[144]). This is in agreement with our assignment. To further explore the effects of energy alignments on the MFEs, one would like to study devices with more pronounced differences in triplet exciton CTS energies. Therefore, we have identified the polymers PF10TBT (E_T = 1.35 eV[140] and E_{CTS} = 1.60 eV[140]) and P3HT (E_T = 1.40[136] and E_{CTS} = 0.90 eV[145]) mixed with PCBM as good candidates.

6.5 Conclusion

In conclusion, in this Chapter we presented a proof of concept study in which we tune triplet–polaron interactions in our devices by deliberately doping with fullerene which influences the triplet exciton density. We have systematically investigated the magnetic field effects on the current for two different polymer–fullerene blends. Using a quantitative analysis of the lineshapes we are able to extract the amplitudes and linewidths of the MFEs. We show that distinct changes in the lineshapes between the two polymer–fullerene blends are correlated to the energetic alignment of the triplet exciton and CTS in the blends. Our findings enable a novel method to engineer the OMAR effect at ultra-small magnetic fields and, moreover, investigate the energetic alignment of excited states in organic semiconductors.

The role of minority carriers in the frequency dependence of organic magnetoresistance

7

In this Chapter we investigate the frequency dependence of organic magnetoresistance (OMAR) both in small molecule-based (Alq_3) and polymer (PPV derivative) materials, and investigate its thickness dependence. For all devices, we observed a strong decrease in magnetoconductance (MC) with increasing frequency of the AC component of the applied magnetic field. Moreover, we observed a strong reduction of the cut-off frequencies for increasing film thickness. By means of admittance spectroscopy and device simulations, we show that the cut-off frequency is related to the inverse transit time of the minority charge carriers. These observations confirm the important role of minority carriers in OMAR, and show that changes in OMAR are not only due to microscopic mechanisms, but also device physics is of significant relevance.[*]

[*] Published as: *On the role of minority carriers in the frequency dependence of organic magnetoresistance.* P. Janssen, W. Wagemans, W. Verhoeven, E.H.M. van der Heijden, M. Kemerink and B. Koopmans, Synthetic Metals **161**, 617 (2011)

7.1 Introduction

Due to their relative ease of processing, chemical tunability and possible low costs, organic semiconductors provide exceptional promise for (future) electronic applications. Recently, it was discovered that the current through an organic semiconductor, sandwiched between two non-magnetic electrodes, can be changed by applying a small (~10 mT) magnetic field.[35] This large (up to 25%) magnetoresistance effect is called organic magnetoresistance (OMAR) and the effect can be both positive and negative depending on operating conditions.[102] OMAR is both interesting for applications and from a scientific point of view.

Up to now, several models have been proposed to explain OMAR,[68–70,104] but the exact origin is still unclear. Most models agree on the fact that OMAR is caused by spin correlations between charge carriers. However, which charge carriers (electrons and/or holes) and how the magnetic fields affect the current, is still heavily debated. Also, it has been suggested that different models might be at work in different regimes of operation.[106] In the current models explaining OMAR different mechanisms are suggested. These mechanisms affect processes in organic devices in different ways and occur on different timescales. Therefore, performing measurements of OMAR on various timescales could provide clues about the processes relevant for OMAR, and thus discriminate between the proposed models.

For instance, on a microscopic scale, the hopping rate of the charge carrier compared to the precession frequency of its spin about the local effective magnetic field is of crucial importance in certain models.[68] These processes typically occur on a nanosecond timescale. On the other hand, triplet excitons could play a role in triplet–triplet annihilation or in reactions with charges.[146] These excitons have a typical lifetime of 25 μs in Alq_3.[147] Also, traps have been suggested to enhance the magnetoconductance (MC), for instance via space-charge effects[91] and by conditioning[148] the devices. Traps in the devices have a typical detrapping time from less than milliseconds up to hours, depending on how deep the traps are. On a macroscopic scale, the time it takes a charge carrier to cross the device from one electrode to the other is given by the transit time τ, which is directly linked to the mobility of the charge carrier, $\tau = L^2/\mu V$, with L the device thickness, μ the mobility, and V the voltage.[149,150] The transit time for holes and electrons is usually different due to the different mobilities, and can be on the order of ms to s in low mobility organic materials.

In the literature, only few experiments were reported in which the frequency of the applied magnetic field played a role. Veeraraghavan *et al.* reported no significant change in the response to an AC magnetic field for frequencies up to 100 kHz.[43] On the other hand, a slow step response on the order of seconds

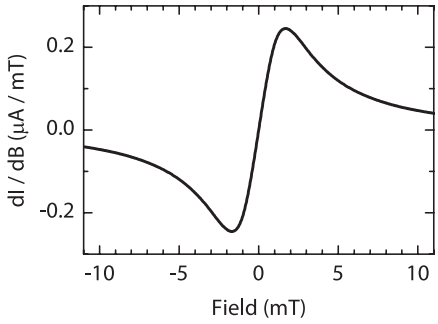

Figure 7.1 | Magnetoconductance measured using an alternating magnetic field. A typical dI/dB measurement at 8 V, 90 Hz, corrected for offset.

was reported by Meruvia *et al.* which they suggested to be caused by the magnetic field acting on the trapping times.[151] Majumdar *et al.* recently showed an increase in OMAR when the rate at which B was swept was decreased, which they conjectured could be caused by traps.[152] Very recently we reported on a systematic study of the frequency dependence of OMAR In an Alq_3 based device, we observed a decrease in MC when the frequency of the oscillating magnetic field was increased from 1 Hz to 1 kHz.[115]

In this Chapter we present a comparison of the frequency dependence of OMAR in different materials and investigate its thickness dependence. We show that the magnetoconductance decreases when the frequency of the AC component of the applied magnetic field is increased. By comparing the frequency dependent OMAR measurements with admittance spectroscopy, we relate the decrease in OMAR to the transit times of the minority carriers and demonstrate that all results are in line with previous claims.[115] Finally, we present preliminary results on device modeling of the frequency dependence.

7.2 Methods

Samples

Here, we show experimental results on tris-(8-hydroxyquinoline) aluminum (Alq_3) and poly[(2-methoxy-5-(3,7-dimethyloctyloxy))-1,4-phenylenevinylene] (MDMO-PPV) based devices. The devices were prepared on glass substrates with patterned indium tin oxide (ITO) anodes. After careful cleaning, followed by a UV-ozone treatment, a thin layer of poly(3,4-ethylenedioxythiophene):poly(styrenesulfonate) (PEDOT:PSS) (Baytron P, H.C. Starck) was applied by spin coating. The MDMO-PPV (American Dye Source) was spin coated from a chlorobenzene solution, whereas the Alq_3 (Sigma–Aldrich) was thermally evaporated in a high vacuum system (~10^{-7} mbar) inside a nitrogen

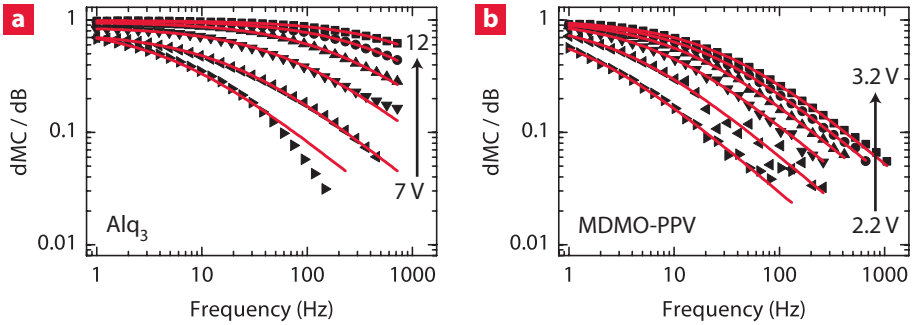

Figure 7.2 | Frequency dependence for two different devices. a | A typical dI/dB measurement at 8 V, 90 Hz, corrected for offset. **b |** Normalized $d\mathrm{MC}/dB$ as a function of frequency for different voltages for a 100 nm thick Alq_3 device and **c |** a MDMO-PPV device, using $dB = 0.5$ mT. The lines are a fit to $\mathrm{MC}_0/[1+(f/f_0)^p]$.

filled glove box. In another vacuum system within the same glove box, LiF and Al were subsequently evaporated as the cathode. The total junction stack thus consisted of ITO/PEDOT:PSS(60 nm)/[Alq_3(100–250 nm) or MDMO-PPV(80 nm)]/LiF(1 nm)/Al(100 nm), with a junction area of 3 mm × 3 mm.

Measurements

Magnetic measurements were performed using an air coil through which a current with both a DC and AC component was sent. This resulted in a magnetic field B with an AC component with amplitude dB. We could sweep the frequency f of the AC magnetic field from 1 Hz to 1 kHz, with a typical amplitude dB of 0.1–0.5 mT. The AC response of the sample current dI was measured with a lockin amplifier over a series resistor, while a constant voltage was applied using a Keithley 2400 Series SourceMeter. Using the magnetic field modulation dB, we can measure the derivative of the current with respect to the magnetic field (dI/dB).[57] An example of such a measurement is shown in Fig. 7.1, which, when integrated, gives a typical OMAR curve. Here, however, we do not measure a full field sweep, but divide the signal at a fixed B by the current to get a measure for the MC, called $d\mathrm{MC}/dB = (dI/dB)/I$. We verified that the shape of the MC curves does not change with frequency, justifying this approach. To remove any extra signal from induction, picked up by the wires at higher frequencies, we measure the difference in signal at +2 and −2 mT, where dI/dB has an opposite sign.

Admittance spectroscopy measurements were performed with a Solartron SI 1260 impedance analyzer. The analyzer can superimpose an AC voltage v_{AC} with a frequency between 1 Hz and 1 MHz on top of a bias voltage up to 35 V.

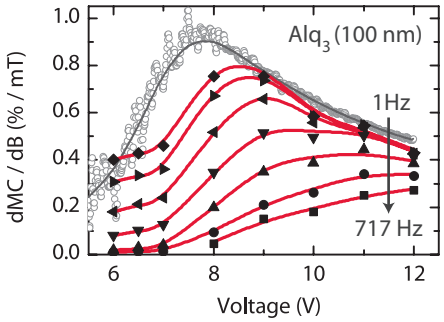

Figure 7.3 | The voltage dependence of the MC for different frequencies. The $d\mathrm{MC}/dB$ as a function of voltage for different frequencies for the 100 nm thick Alq_3 device and MC as a function of voltage for B = 83 mT, measured with a permanent magnet (open symbols).[57]

We used an AC voltage of 50 mV, but our results were checked to be independent of the magnitude of v_{AC}.

7.3 Frequency dependence

We measured the frequency dependence of the MC at different voltages, starting from a voltage just above the onset of OMAR. The results for the 100 nm thick Alq_3 device and MDMO-PPV device are shown in Fig. 7.2a and b respectively. We observe a clear frequency dependence of OMAR, where, for all measured voltages, the MC decreases with increasing frequency. This decrease is more pronounced for lower voltages. We excluded experimental artifacts by also measuring the system response to magnetic field modulations, where we did not observe any frequency dependence. In Fig. 7.2 we can observe that the point where the MC starts to decrease shifts to higher frequencies with increasing voltage for both devices. We used an empirical fitting function $d\mathrm{MC}/dB = \mathrm{MC}_0/[1 + (f/f_0)^p]$ to fit our data. Here, MC_0 represents $d\mathrm{MC}/dB$ at 0 Hz, f_0 the frequency were $d\mathrm{MC}/dB$ is reduced by a factor of 2 and p is the slope of the curve at high frequencies ($f \gg f_0$). Note that other fitting functions can be used as well,[115] however this function yields the best global fit of all measured data.

Alternatively, we can extract the voltage dependence of the MC at fixed frequencies from Fig. 7.2. The corresponding result for Alq_3 is shown in Fig. 7.3. At low frequencies, a typical $\mathrm{MC}(V)$ curve is obtained, which first increases with increasing voltage, has a maximum, and then slowly decreases. For increasing frequency, the $\mathrm{MC}(V)$ curve collapses, with the strongest reduction at low voltages. Also plotted is the MC obtained from a quasi-DC measurement using a technique introduced by Wagemans *et al.* (small symbols).[57] This curve fits

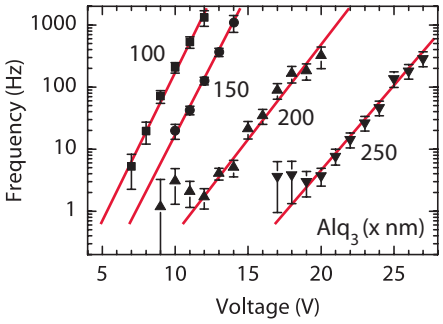

Figure 7.4 | Frequency dependency of Alq_3 devices as a function of thickness. The characteristic cut-off frequency f_0 as a function of voltage for different Alq_3 layer thicknesses. The lines provide a guide to the eye.

the extrapolation of the trend in the curves from 717 to 1 Hz, except for voltages smaller than 7 V.

To investigate the role of organic layer thickness, we have performed frequency dependent measurements on Alq_3 samples as a function of thickness. Results for film thickness varying from 100 to 250 nm are shown in Fig. 7.4. Here the characteristic cut-off frequency f_0, obtained from the fits, is plotted as a function of voltage for different Alq_3 layer thicknesses. From Fig. 7.4 we can see that the shift in cut-off frequency to higher frequencies with increasing voltages also holds for thicker devices. Moreover, we observe a strong reduction of the cut-off frequencies for increasing film thickness.

7.4 Admittance spectroscopy

In the previous section we showed the results for the frequency dependence of OMAR while using an oscillating magnetic field. In addition to the response of the current to this AC magnetic field, we can also measure the response to an AC voltage. This response is described by the admittance $Y = dI/dV = G + iB$, where G is the conductance and $B = 2\pi f C$ the susceptance, in which C represents the capacitance. The measured C and B for the 100 nm thick Alq_3 device are shown in Fig. 7.5.

In Fig. 7.5, below 7 V a decreasing capacitance as a function of frequency is observed, while for $V > 7$ V the capacitance starts negative and then converges to the low voltage signal. For increasing voltage, this negative contribution to the capacitance is more pronounced and shifts to higher frequencies with increasing voltage. The different contributions to the out-of-phase part of the admittance are more clearly visualized by plotting the normalized differential susceptance $\Delta B = 2\pi f(C - C_{geo})/\Delta B_{max}$, as can be seen in Fig. 7.5b. Here, C_{geo}

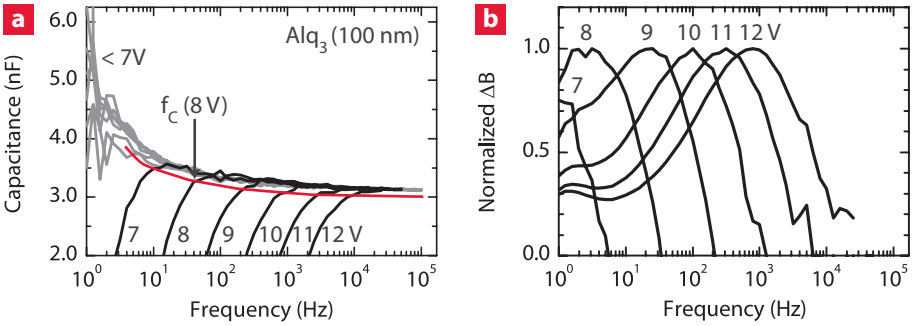

Figure 7.5 | Capacitance as a function of the AC voltage frequency for different DC bias voltages. a | The frequency f_C where C is 95% of the 0 V value is indicated for the 8 V measurement. **b |** The normalized differential susceptance ΔB as a function of frequency for different voltages.

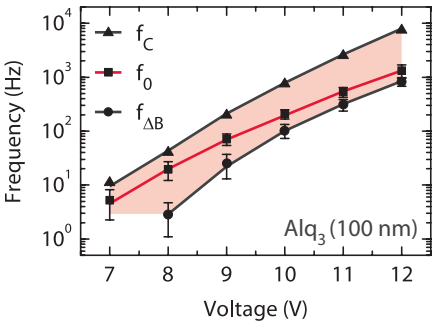

Figure 7.6 | Characteristic frequencies as a function of voltage for the 100 nm Alq_3 device. The cut-off frequency f_0 (squares), the frequency where the capacitance is 95% of its low voltage value, f_C (triangles), and the frequency for the peak in differential susceptance $f_{\Delta B}$ (circles).

is the geometrical capacitance given by $C_{geo} = \varepsilon\varepsilon_0 A/L$, with A the area and L the thickness of the device and ε the dielectric constant of the organic material. A clear peak in the differential susceptance, shifting to higher frequencies with increasing voltage, is observed.

Interestingly, the decrease in MC, shifting to higher frequencies with increasing voltage, seems to be correlated to the negative contribution to the capacitance and the shift in differential susceptance. To illustrate this correlation, Fig. 7.6 shows the characteristic cut-off frequency f_0 for the MC as well as the frequency where the capacitance is 95% of its low voltage value, f_C, and the frequency for the peak in differential susceptance $f_{\Delta B}$ as a function of voltage for the 100 nm Alq_3 device. A clear correlation between the frequencies is observed and all

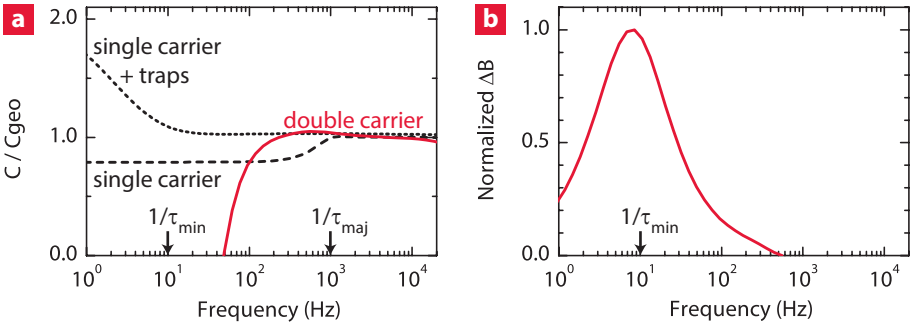

Figure 7.7 | Device model simulation of a typical device. a | Simulation of the capacitance of a single-carrier device with (dotted line) and without (dashed line) traps, and of a double-carrier device (solid line) as a function of frequency. **b |** The calculated normalized differential susceptance ΔB of the double-carrier device.

curves are approximately showing an exponential increase with voltage. We have to note that the low frequency/voltage values have a larger uncertainty, resulting in a possible overestimation of the cut-off frequency.

In order to interpret the correlation between f_0, f_C and $f_{\Delta B}$, first we will discuss the observed trends in the (differential) capacitance. Therefore, we simulated a prototype device using an approach similar to Gommans *et al.*[153] Model parameters were chosen such as to obtain a significant difference between the transit times for majority and minority carriers. Furthermore we assumed ohmic injection of majority carriers, and an injection limited process of minority carrier injection.[91] A typical set of results is shown in Fig. 7.7. Let us first examine the single-carrier device without traps (dashed line in Fig. 7.7). At high frequencies ($f \gg 1/\tau_{maj}$), the dielectric properties of the organic material, as giving by the geometric capacitance C_{geo}, are probed. At low frequencies ($f \ll 1/\tau_{maj}$), the (majority) charges in the device easily follow the voltage modulation and due to charge relaxation C is less than C_{geo}. Shao and Wright[154] demonstrated this effect for drift-only transport and calculated that the low frequency capacitance is exactly 3/4 of the geometric capacitance. Here, we also included diffusion into our simulations and thereby we observe a small deviation from this factor. The transition between the two regimes occurs around $f = 1/\tau_{maj}$. Including traps into our device simulation,[91] results in an increase of capacitance at low frequencies (dotted line in Fig. 7.7). Traps increase the ability of the device to store charges, resulting in an increased capacitance. Once the frequency becomes larger than the inverse trapping time, the contribution from the traps diminishes. The simulated results for the single-carrier device

with traps nicely resemble the situation for $V < 7$ V in our measurements, as shown in Fig. 7.5.

If we now simulate a double-carrier device, where both majority and minority carriers are injected, we can simulate the negative contribution to the capacitance as measured for $V \geq 7$ V (solid line in Fig. 7.7). Figure 7.7b shows the calculated normalized differential susceptance ΔB of the double-carrier device. The negative contribution to the capacitance is equivalent to the reduction in capacitance in the single-carrier device as described above. The (differential) capacitance reflects the (change in) stored charge in the device. The presence of (additional) space-charge in the device results in an extra contribution ΔC to the geometrical capacitance. Because it takes time to build-up the space-charge, this contribution lags behind, and ΔC becomes negative. Due to cancelation of the space-charge, a much larger amount of charge can be stored in a double-carrier device, resulting in negative contribution ΔC, which can be larger than the geometrical capacitance, and thereby causing the total capacitance to be negative. If the frequency becomes larger than $1/\tau_{\min}$, the minority charge carriers can no longer follow the voltage modulation and the device starts to follow the single carrier case. The position of the peak in the differential susceptance is inversely proportional to the transit time of the minority charge carriers $f_{\Delta B} \sim 1/\tau_{\min}$.

Now, we can interpret the measured capacitance as shown in Fig. 7.5 as follows. For $V < 7$ V the device is single-carrier and contains traps, while for $V \geq 7$ V, minority carriers are injected as is evident from the presence of a negative capacitance at low frequencies. At frequencies higher than f_C, the negative contribution to the capacitance diminishes; eliminating the role of the minority carriers and thereby yielding a single-carrier device behavior. At frequencies lower than $f_{\Delta B}$, the minority carriers in the device can almost completely follow the modulations and remain present in the AC response of the device. We can therefore state that the upper frequency limit for the role of minority carriers in the AC response of the device is governed by f_C, whereas the lower limit by $f_{\Delta B}$. The intermediate regime, where the role of the minority carriers diminishes, is marked in Fig. 7.6. The cut-off frequency for MC f_0 is found to lie in this intermediate regime, as shown in Fig. 7.6, meaning that the MC is significantly reduced beyond frequencies where the role of the minority carriers diminishes.

Both $f_{\Delta B}$ and f_C scale inversely with the transit time of the minority charge carrier $f_{\Delta B} \sim f_C \sim 1/\tau_{\min} = \mu_{\min} V/L^2$. Since we observe a strong reduction of the cut-off frequencies for increasing film thickness, as shown in Fig. 7.4, our results for the frequency dependence of OMAR as a function of organic layer thickness seem to be in agreement with our claim that the frequency dependence is related to the transit time of the minority carrier. These observations confirm the important role of minority carriers in OMAR, and show that changes in

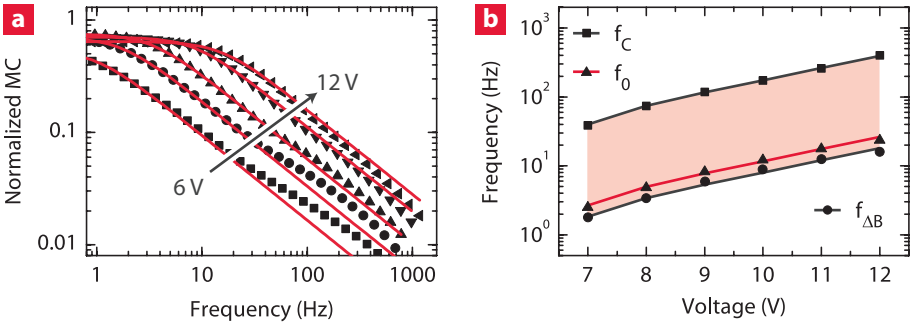

Figure 7.8 | Simulated frequency dependence for a 100 nm Alq_3 device. **a |** Normalized MC as a function of frequency for different voltages **b |** The cut-off frequency f_0 (squares), the frequency where the capacitance is 95% of its low voltage value, f_C (triangles), and the frequency for the peak in differential susceptance $f_{\Delta B}$ (circles).

OMAR are not only due to microscopic mechanisms, but can be explained in terms of device physics. [91,102]

7.5 Device modeling

In order to gain more insight in the processes governing the frequency dependence of OMAR we have performed device simulations, where we solve the drift and diffusion equations numerically. In our approach we include traps in the majority charge carrier channel (a more detailed description of the device model is provided in the work of Bloom *et al.* [91]). We modeled the device using an ohmic contact for the majority carriers and an injection limited minority contact. Actually, the IV-characteristics and admittance of the device for the conditions used here was already shown in Fig. 7.7.

Here, in addition, we model the OMAR effect by assuming a magnetic-field induced change in minority, majority or recombination mobility. Bloom *et al.* [91] used this approach to calculate the steady state currents. In order to derive the frequency dependence, we calculate the transient response to a step in one of the mobilities, and apply a Fourier transformation to the data. As an example, we simulated the case where the magnetic field acts only on the minority mobility. The results are shown in Fig. 7.8, where the symbols represent the simulation for a 100 nm thick Alq_3 device and the solid lines are a fit to extract the cut-off frequency f_0. Figure 7.8b shows the characteristic frequencies obtained from the simulations as a function of voltage. We observe a qualitatively similar trend to the experimental results as shown in Fig. 7.6. We are currently performing a more systematic study comparing measurements and simulations,

also on other organic materials. Thereby, we aim at further understanding the frequency dependence of OMAR, which possibly will allow us to further unravel the underlying mechanisms.

7.6 Conclusion

In conclusion, we have shown frequency dependent OMAR measurements on MDMO-PPV and Alq_3 based devices, where we studied the frequency dependence as a function of organic layer thickness. For all devices, we observed a strong decrease in MC with increasing frequency, and the decrease is more pronounced for lower voltages. Moreover, we observed a strong reduction of the cut-off frequencies for increasing film thickness. By means of admittance spectroscopy and device simulations, we have shown that the cut-off frequency for the decrease in MC is related to the inverse transit time of the minority charge carriers. Preliminary results on device modeling of the frequency dependence show a qualitative fit to the measured data, although a more elaborate comparative study is needed to fully unravel the underlying mechanism.

8

Conclusions and outlook

This final Chapter concludes the work presented in this thesis. We will reexamine the goal of this thesis and show that we have successfully succeeded in achieving it. Then, we proceed by presenting an outlook on future research. Here, we will discuss two highly interesting (near-)future developments. The first is aimed at a deeper fundamental understanding of OMAR, which can be done by investigating the magnetic field effects in the electroluminescence. In the second part we sketch possible routes towards optimally engineered OMAR devices.

8.1 Conclusions

The work presented in this thesis focused on magnetic field effects on the current in organic semiconductor based devices, often referred to as "organic magnetoresistance" (OMAR). The goal of this thesis was to reveal the dominant underlying mechanisms of OMAR. Therefore, we presented a unified picture of the different contemporary mechanisms that have been proposed for OMAR and we combined this with theoretical models that have been developed to describe OMAR in a quantitative way. Using this framework, we were able to relate changes in the measured magnetic field effects to different underlying microscopic and device parameters. To unravel the physics of OMAR lineshapes, we introduced a novel empirical function that allows us to separately extract the role of different relevant microscopic parameters. From the research presented in this thesis we can conclude that:

> "*The dominant mechanism of OMAR depends on the exact material choice, morphology and operating conditions of the device. Moreover, we showed that detailed measurements of the magnetic field effects on the current as a function of voltage and magnetic field can be used as fingerprints to identify the underlying mechanism.*"

Furthermore, we presented a proof of concept study which illustrates that we can engineer devices in order to tailor the OMAR effects as desired. Therefore, we tuned the triplet–polaron interactions in the device by deliberately doping the organic layer with fullerene. Using the framework as developed in this thesis, we showed that distinct changes in the lineshapes were correlated to the energetic alignment of the triplet exciton and charge-transfer state in the device. In the last section of this thesis, we present an outlook on future research (partly) based on the conclusions of this work.

8.2 Outlook

By unraveling scientifically intriguing puzzles such as OMAR –inevitably– new fundamental questions and technological possibilities emerge. At this point, the list of possible new experiments might be even longer then when we started researching OMAR. In this final section, we will highlight two highly interesting topics. The first is related to a deeper fundamental understanding of the processes involved in OMAR, whereas the second is more aimed at (commercially) exploiting the effect.

Expanding our view

In this thesis, we have measured and explained OMAR in terms of magnetic-field dependent changes in the current trough the devices. There are, however, other

experimental methods to investigate OMAR. We can, for example, induce a current in an organic semiconductor device by illuminating the device with an external light source. Then, we can measure the magnetic field effects in this so-called photocurrent (MPC). In this case, we do not inject free charge carriers into the device, as has been done throughout this thesis and is depicted in Figs. 2.1 and 2.6, but we create (excited) singlet exciton states within the organic layer. In the literature it has been shown that this can have profound effects on the magnetic field effects in terms of their linewidths and amplitudes.[57] Investigating these magnetic field effects on the photocurrent using the framework as presented in this thesis, can provide a deeper understanding of the relevant particles and their spin-dependent reactions.

Another additional experimental method to further investigate OMAR is by measuring the magnetic field effect on the electroluminescence (MEL). In this case, we do not measure the effects on the current through the device, but we directly probe the magnetic field dependent emissive transitions to the ground state. Although the MEL and MC share some common origin, their lineshapes and voltage dependencies can be completely different. In preliminary results on SY-PPV:PCBM blends (Chapter 5), for example, the distinct low-field feature in the MC (clearly visible in Fig. 6.5d,f) is not observed in the MEL. Moreover, both magnetic field effects show different high field effects. A detailed study on such a system could provide supplementary information on the exact underlying mechanisms.

Finally, we would like to note that it is also possible to measure the electroluminescence spectrum instead of the total intensity. We have recently performed pilot experiments to examine the feasibility of this novel experimental approach. Ultimately, this enables us to measure the magnetic field effects on the luminesce for different energetic transitions. In the case of polymer–fullerene blends for example, we are then able to distinguish between singlet-to-ground state transitions in the polymer and charge-transfer state.

Engineering magnetoconductive devices

In the last section of this thesis, we want to sketch possible routes towards optimally engineered OMAR devices. Since its discovery, a number of possible applications have been proposed, such as magnetic pen-input organic light-emitting displays,[43] magnetic field sensors[44] and, very recently, an OMAR based compass able to measure the earth's magnetic field.[155]

From an engineering point of view, OMAR devices face the same challenges as contemporary organic based devices such as OLEDs and OPVs. The main issues to be solved include increasing the stability and reducing the degradation of the devices during operation in ambient conditions. In order to make the devices commercially attractive, they must be easy and cheap to process

–preferably on a roll-to-roll base, allowing the use of flexible substrates. Most of these problems can be solved by properly engineering the organic materials and the actual devices.

From a scientific point of view, one would like to enhance the OMAR effect and, ultimately, design the lineshape as desired. Theoretically, Kersten *et al.* [138] recently proposed a system where very large (up to 99%) magnetic field effects could be realized by creating a optimally designed doped polymer device. Even more excitingly, Mahato *et al.* [156] showed results on giant magnetic field effects (more than 90%) in molecular wires. These results show that, both theoretically and experimentally, it seems possible to engineer huge magnetic field effects on the current at roomtemperature.

We are now faced with the challenge to create actual prototype devices wherein these large effects can also be obtained. As mentioned earlier, we want to exploit the unique advantages of organic materials, and therefore would like to be able to create these devices using cheap and relatively easy production techniques. Moreover, we would like the possibility to completely tune the effect. The framework as presented in this thesis provides researchers with guide to do so.

Summary

Spins in organic semiconductors

Revealing the dominant mechanisms of organic magnetoresistance

The research described in this thesis focuses on the combination of two fields in physics, namely organic electronics and spintronics. The first exploits the (chemical) tunability, ease of processing and low costs of organic semiconductors and provides an exceptional promise for (future) electronic applications. The latter makes explicit use of the electron spin in electronic devices and has revolutionized magnetic data storage over the last decades. By combining the two into organic spintronics, we can use organic materials in spintronic devices or add spin and magnetic field functionality into organic devices. One of the exciting developments in the field of organic spintronics is the discovery of a surprisingly large, room temperature, magnetoresistance effect in organic semiconductor devices without any ferromagnetic components, often referred to as "organic magnetoresistance" (OMAR). The current through such a device, where the organic layer is sandwiched between two non-magnetic electrodes, can be changed significantly (up to 25%) by applying a small (a few milliteslas) magnetic field.

During the last decade, OMAR has puzzled the young field of organic spintronics. Even though recently writable organic displays and cheap plastic sensor technology have been proposed as an example of its application potential, the fundamental understanding of the interactions of spins and charges in organic semiconductors remains the goal of extensive experimental and theoretical research. The goal of this thesis is to reveal the dominant underlying mechanisms of OMAR and present a unified, quantitative framework to describe the experimentally observed trends. By achieving this goal, we open up unprecedented means to bring OMAR research from a phase of passively observing magnetic field effects in the current, to a stage of really engineering devices to tailor the OMAR effect as desired.

In this thesis, we have discussed the current perspectives on organic magnetoresistance. We presented a unified picture of the different contemporary mechanisms that have been proposed for OMAR. Combined with theoretical models that have been developed to describe OMAR in a quantitative way, this unified picture acts as a framework to relate changes in the measured magnetic field effect lineshapes and voltage dependencies to microscopic and device parameters throughout this thesis. To analyze the physics of OMAR lineshapes, we introduced a new empirical function that allows us to separately extract the role of different relevant microscopic parameters. By addressing recent numerical and experimental studies, we have shown that this new function can be successfully used to analyze the lineshapes.

We have determined the dominant mechanism for OMAR by performing a proof of concept study using a polymer–fullerene blend. By changing the blending ratio, we tuned the spin and charge interactions in the device. We have systematically investigated the magnetic field effect on the current as a function of the applied magnetic field and the bias voltage for a broad range of fullerene concentrations. We observed an extremely rich behavior of the OMAR effect with very pronounced changes in amplitudes and linewidths. By examining the lineshapes and voltage dependencies, and comparing them with explicit quantitative calculations, we identified three regimes where: (1) reactions between triplet excitons and polarons are the dominant mechanism, (2) interactions of electrons and holes become dominant and (3) the magnetic field effects are mainly caused by a bipolaron mechanism which relies on the interaction of like charges. Which mechanism dominates, depends on the exact material choice, morphology and operating conditions of the device. Our findings showed that detailed measurements of the magnetic field effects on the current as a function of voltage and magnetic field can be used as fingerprints to identify the underlying mechanism.

Furthermore, in a detailed study, we have measured the magnetic field effects on the current as a function of the applied voltage and temperature in pristine polymer devices where the reactions between triplet excitons and polarons are dominant. We presented a fully quantitative analysis of the OMAR lineshape and extract all linewidth parameters. By studying these parameters as a function of voltage and temperature, we obtained detailed information about the interactions between excitons and charges. We have shown that the hyperfine field strength is almost identical for all measurements, whereas the additional broadening caused by the microscopic mechanism did show a remarkable voltage and temperature dependence. Moreover, we discovered a surprising voltage and temperature dependence of the high-field effect linewidth. Preliminary results on microscopic simulations have shown a qualitative agreement to the

experimental results, opening up novel routes towards a deeper fundamental understanding of the relevant triplet–polaron reaction rates for OMAR.

As a first example of really engineering OMAR devices, we presented a proof of concept study in which we tuned the triplet–polaron interactions in the device by deliberately doping the organic layer with fullerene which influences the triplet exciton density. We have systematically investigated the magnetic field effects on the current for two different polymer–fullerene blends. Using a quantitative analysis of the lineshapes we were able to extract the amplitudes and linewidths of the magnetic field effects. We showed that distinct changes in the lineshapes were correlated to the energetic alignment of the triplet exciton and charge-transfer state in the blends. Our findings enable a novel method to engineer the OMAR effect at ultra-small magnetic fields and, moreover, investigate the energetic alignment of excited states in organic semiconductors.

Finally, to illustrate the important and often highly non-trivial role of device physics, we have measured the frequency dependent OMAR. We performed measurements on small molecule and conjugated polymer based devices, where we studied the frequency dependence as a function of organic layer thickness. For all devices, we observed a strong decrease in the magnetic field effect with increasing frequency, where the decrease was more pronounced for lower voltages. Moreover, we observed a strong reduction of the cut-off frequencies for increasing film thickness. By means of admittance spectroscopy and device simulations, we have shown that the cut-off frequency for the decrease in OMAR can be related to the inverse transit time of the minority charge carriers. Preliminary results on device modeling of the frequency dependence have shown a qualitative fit to the measured data.

Curriculum vitae

Paul Janssen was born on May 20, 1982 in Roermond, the Netherlands. He went to high school at the Bisschoppelijk College in Echt. In 2000, he started his study Applied Physics at the Eindhoven University of Technology.

During his studies, he did a local internship in the Transport in Permeable Media (TPM) group of prof.dr.ir. Klaas Kopinga, where he performed Nuclear Magnetic Resonance studies on water-glycerin mixtures. Thereafter, he did an external traineeship in the group of dr. Patrick LeClair at the Center for Materials for Information Technology (MINT) in Tuscaloosa, Alabama, USA. Here, he studied spinpumping in CoFeB multilayers using a Ferromagnetic Resonance technique. For his graduation project, he investigated a novel method for creating nanometer sized magnetic devices. He did this research under the supervision of prof.dr.ir. Henk Swagten at the group Physics of Nanostructures (FNA).

After his graduation, Paul decided to stay at FNA as a PhD candidate. He started his PhD on a completely different subject, namely in the field of organic spintronics. His research has focused on magnetic field effects on the current in organic semiconductor devices. Part of his PhD work is described in this thesis. The work resulted in several publications in prominent scientific journals and presentations at international conferences. As part of his work, Paul supervised four Bachelor and four Master students.

During his PhD, Paul became a board member of the alumni association of Applied Physics (VENI). He was responsible for the quarterly magazine (N!), later became secretary and is currently chairman of the board. In his free time, Paul likes to lift heavy weights and to enjoy good food.

Publications and presentations

Publications

Tuning organic magnetoresistance in polymer-fullerene blends by controlling spin reaction pathways. P. Janssen, M. Cox, S.H.W. Wouters, M. Kemerink, M.M. Wienk and B. Koopmans. *Accepted for publication in Nature Communications* (2013).

Unraveling the temperature and voltage dependence of magnetic field effects in organic semiconductors. P. Janssen, S.H.W. Wouters, M. Cox and B. Koopmans. *Under review at Journal of Applied Physics* (2013).

Investigating the influence of the triplet energy alignment on organic magnetoresistance. P. Janssen, S.H.W. Wouters, M. Cox and B. Koopmans. *Under review at Organic Electronics* (2013).

Large magnetoresistance in electrochemically doped organic light emitting diodes. S. van Reenen, S.P. Kersten, M. Cox, P. Janssen, S.H.W. Wouters, B. Koopmans, P.A. Bobbert, R.A.J. Janssen and M. Kemerink. *Under review at Physical Review B* (2013).

Beneficial imperfections: Identifying intrinsic trap states as a crucial component for organic magnetoresistance M. Cox, E.H.M. van der Heijden, P. Janssen, and B. Koopmans. *In preparation*.

On the origin of organic magnetoresistance: Evidence for traps and trions. M. Cox, P. Janssen, F. Zhu, and B. Koopmans. *Physical Review B* **88**, 035202 (2013).

The influence of device physics on organic magnetoresistance. M. Cox, P. Janssen, S.H.W. Wouters, E.H.M. van der Heijden, M. Kemerink and B. Koopmans. *Synthetic Metals* **173**, 10 (2013).

On the role of minority carriers in the frequency dependence of organic magnetoresistance. P. Janssen, W. Wagemans, W. Verhoeven, E.H.M. van der Heijden, M. Kemerink and B. Koopmans. *Synthetic Metals* **161**, 617 (2011).

The many faces of organic magnetoresistance. W. Wagemans, P. Janssen, A.J. Schellekens, F.L. Bloom, P.A. Bobbert and B. Koopmans. *SPIN* **1**, 93 (2011).

Frequency dependence of organic magnetoresistance. W. Wagemans, P. Janssen, E.H.M. van der Heijden, M. Kemerink and B. Koopmans. *Applied Physics Letters* **97**, 123301 (2010).

Spin pumping in $Co_{56}Fe_{24}B_{20}$ multilayer systems. H. Lee, L. Wen, M. Pathak, P. Janssen, P. LeClair, C. Alexander, C.K.A Mewes and T. Mewes. *Journal of Physics D* **41**, 215001 (2008).

Presentations

Tuning spins in organics: Unraveling organic magnetoresistance by experiments and modeling (poster). P. Janssen, M. Cox, F. Zhu, S.H.W. Wouters, E.H.M. van der Heijden, M. Kemerink, M.M. Wienk and B. Koopmans. *Physics @FOM 2013*, Veldhoven, The Netherlands (22 – 23 January 2013).

Tuning spin interactions in organic semiconductors (contributed). P. Janssen, M. Cox, M. Kemerink, M.M. Wienk and B. Koopmans. *The 4^{th} Topical Meeting on Spins in Organic Semiconductors (SPINOS)*, London, United Kingdom (10 – 13 September 2012).

Tuning spin interactions in organic semiconductors (poster). P. Janssen, M. Cox, M. Kemerink, M.M. Wienk and B. Koopmans. *The 7^{th} International Conference on Physics and Applications of Spin-related Phenomena in Semiconductors (PASPS)*, Eindhoven, The Netherlands (5 – 8 August 2012).

Tuning spin interactions in organic semiconductors (contributed). P. Janssen, M. Cox, M. Kemerink, M.M. Wienk and B. Koopmans. *Physics@FOM 2012*, Veldhoven, The Netherlands (17 – 18 January 2012).

Unraveling frequency dependence of organic magnetoresistance by experiments and device modeling (poster). P. Janssen, W. Wagemans, M. Kemerink and B. Koopmans. *The 11th European Conference on Molecular Electronics (ECME)*, Barcelona, Spain (7 – 10 September 2011).

Unraveling organic magnetoresistance by experiments and modeling (poster). P. Janssen, M. Cox, W. Wagemans, A.J. Schellekens, F.L. Bloom, M.M. Wienk, M. Kemerink, P. Bobbert and B. Koopmans. *The 4th Joint Nanoworkshop 2011*, München, Germany (1 June 2011).

Tuning spin interactions in organic semiconductors (contributed). P. Janssen, M. Cox, M. Kemerink, M.M. Wienk and B. Koopmans. *The 12th International Symposium on Spin and Magnetic Field Effects in Chemistry and Related Phenomena (SCM)*, Noordwijk, The Netherlands (15 – 20 May 2011).

Unraveling organic magnetoresistance by experiments and device modeling (poster). P. Janssen, W. Wagemans, F.L. Bloom, M. Cox, M. van Schijndel, M. Kemerink and B. Koopmans. *Physics@FOM 2011*, Veldhoven, The Netherlands (18 – 19 January 2011).

Frequency dependence of organic magnetoresistance (contributed). P. Jansssen, W. Wagemans, E.H.M. van der Heijden, M. Kemerink and B. Koopmans. *The 56th Conference on Magnetism and Magnetic Materials (MMM)*, Atlanta, Georgia, U.S.A. (14 – 18 November 2010).

Frequency dependence of organic magnetoresistance (contributed). P. Janssen, W. Wagemans, E.H.M. van der Heijden, M. Kemerink and B. Koopmans. *The 3rd Topical Meeting on Spins in Organic Semiconductors (SPINOS)*, Amsterdam, The Netherlands, (30 August – 3 September 2010).

Organic magnetoresistance: unravelling the origin of sign changes (poster). P. Janssen, W. Wagemans, F.L. Bloom and B. Koopmans. *cNM Research Day 2010*, Eindhoven, The Netherlands (30 June 2010).

Organic magnetoresistance: unravelling the origin of sign changes (poster). P. Janssen, W. Wagemans, F.L. Bloom and B. Koopmans. *Physics@FOM 2010*, Veldhoven, The Netherlands (19 – 20 January 2010).

Acknowledgements / Dankwoord

Het dankwoord. Het leukste hoofdstuk om te schrijven. Eindelijk kan ik alle mensen die mij direct of indirect geholpen hebben bedanken. Dus als eerste: jij. Bedankt! Ook al lees je alleen dit dankwoord of kijk je vluchtig naar de figuren in dit proefschrift, toch bedankt voor je interesse. Een aantal mensen wil ik in het bijzonder bedanken.

Als eerste wil ik graag mijn directe begeleider en promotor, Bert Koopmans, bedanken. Bert, het is mij een genoegen dat ik met jou heb mogen samenwerken de afgelopen jaren. Ik bewonder je onuitputtelijke energie en je immer aanwezige enthousiasme. Ondanks je drukke schema –veroorzaakt door de vele colleges en onze verhuizing– wist je toch steeds weer tijd vrij te maken voor een wetenschappelijk of persoonlijk gesprek. Bedankt hiervoor!

Ik wil de leden van mijn commissie, Henk Swagten, Martijn Kemerink, Paul Blom, Michael Flatté, Peter Bobbert en Etienne Goovaerts, ook hartelijk bedanken. Henk, dankzij jou heb ik in een ver verleden de keuze gemaakt om bij FNA te komen afstuderen. Bedankt voor je kritische commentaar de afgelopen jaren. Martijn, bedankt voor je medewerking bij ons onderzoek. Dankzij jouw expertise en je DriftKicker hebben we vele mysterieuze OMAR verschijnselen kunnen verklaren. Peter, bedankt voor je hulp bij theoretische vraagstukken. Ik ben ervan overtuigd dat we dankzij onze samenwerking OMAR nu veel beter begrijpen. Etienne, ook jou wil ik graag bedanken voor onze samenwerking. Helaas heeft het nog geen hoofdstuk in mijn thesis mogen opleveren, maar ik weet zeker dat er nog een mooie publicatie uit voort gaat komen.

Alle leden en oud-leden van de vakgroep fysica van nanostructuren (FNA) wil ik graag bedanken. Jullie hebben ervoor gezorgd dat ik hier een aantal onvergetelijke jaren heb gehad. Ik zal de talloze bier-en-chips of champagne-en-vis borrels nooit meer vergeten. Ook bedankt voor de gezelligheid tijdens de diverse andere sociale activiteiten die we ondernomen hebben: De jaarlijkse groepsuitjes, Sinterklaasavond, de braspartij, de spellenavonden, bezoekjes aan

de borrel, sportevenementen en ga zo maar door. Dus, Beatriz, Gerrie, Jeroen, Karin, Wim, Jürgen, Bert, Oleg, Jef, Henk, Arno, Matthijs, Jeroen, June, Koen, Reinoud, Reinier, Sjors, Nidhi, Timothy, Aurelie, Feng en alle studenten, bedankt! Een bijzonder dankwoord aan de lange man die het ruim vier jaar met mij op één kamer heeft uitgehouden, of moet ik zeggen: ik met hem? Koen, bedankt voor de talloze (zinloze) YouTube fragmenten, onze discussies over van-alles-en-nog-wat en de duizenden kilo's die we in de sportschool verplaatst hebben.

Een dankbetuiging voor de organics-crew: Wiebe, Francisco, Jurgen, Matthijs en Feng. Ontzettend bedankt voor jullie hulp bij het uitvoeren van de experimenten en simulaties, en tijdens het schrijven van artikelen. Ook bedankt voor jullie fijne gezelschap tijdens de conferenties die we samen bezocht hebben. Aan bijna alle hoofdstukken van dit proefschrift hebben één of meerdere studenten die ik heb mogen begeleiden meegeholpen. Dus Ilse, Steinar, Matthijs en Mathijs (Master), en Wouter, Jan, Christiaan en Ilse (Bachelor): hartelijk bedankt.

Ik wil Jos, Rick, Guy en Hugo bedanken voor de vriendschap die wij nu al jaren delen. Ook al ontaarden onze activiteiten vaak in te veel eten, drinken en slap geouwehoer, ik geniet er nog steeds iedere keer met volle teugen van! Maarten, Nicole, Frank en Wenya, bedankt voor de fijne tijd die we samen op de Van der Waalsweg gehad hebben en de vriendschap die ik daar aan overgehouden heb.

Natuurlijk wil ik graag mijn familie bedanken. Pap, mam, Inge en Kamil bedankt voor jullie steun, liefde en vertrouwen. Bedankt dat jullie mij al die jaren zijn blijven steunen. Als laatste wil ik iemand bedanken die mijn leven de laatste jaren heeft verrijkt. Desie, bedankt voor je steun en liefde. Het was niet altijd even makkelijk de afgelopen jaren, maar samen hebben we het toch allemaal maar mooi voor elkaar gekregen!

Bedankt!

Bibliography

[1] W. Brütting and C. Adachi, ed., *Physics of Organic Semiconductors* (Wiley, 2012).

[2] M.C. Petty, *Molecular Electronics: From Principles to Practice* (Wiley, 2007).

[3] H. Akamatu, H. Inokuchi and Y. Matsunaga, *Electrical conductivity of the perylene–bromine complex*, Nature **173**, 168 (1954).

[4] C.K. Chiang, C.R. Fincher, Y.W. Park, A.J. Heeger, H. Shirakawa, E.J. Louis, S.C. Gau and A.G. MacDiarmid, *Electrical conductivity in doped polyacetylene*, Phys. Rev. Lett. **39**, 1098 (1977).

[5] A. Bernanose, M. Comte and P. Vouaux, *A new method of light emission by certain organic compounds*, J. Chim. Phys. **50**, 64 (1953).

[6] C.W. Tang and S.A. VanSlyke, *Organic electroluminescent diodes*, Appl. Phys. Lett. **51**, 913 (1987).

[7] J.H. Burroughes, D.D.C. Bradley, A.R. Brown, R.N. Marks, K. Mackay, R.H. Friend, P.L. Burns and A.B. Holmes, *Light-emitting diodes based on conjugated polymers*, Nature **347**, 539 (1990).

[8] H.T. Yi, M.M. Payne, J.E. Anthony and V. Podzorov, *Ultra-flexible solution-processed organic field-effect transistors*, Nat. Commun. **3**, 1259 (2012).

[9] S.R. Forrest, *The path to ubiquitous and low-cost organic electronic appliances on plastic*, Nature **428**, 911 (2004).

[10] Philips, *BASF and Philips first to develop OLED lighting for use as a transparent car roof*, www.lighting.philips.com (2012).

[11] H. Spreitzer, H. Becker, E. Kluge, W. Kreuder, H. Schenk, R. Demandt

and H. Schoo, *Soluble phenyl-substituted PPVs: New materials for highly efficient polymer LEDs*, Adv. Mater. **10**, 1340 (1998).

[12] M.A. Baldo, D.F. O'Brien, Y. You, A. Shoustikov, S. Sibley, M.E. Thompson and S.R. Forrest, *Highly efficient phosphorescent emission from organic electroluminescent devices*, Nature **395**, 151 (1998).

[13] C. Deibel and V. Dyakonov, *Polymer–fullerene bulk heterojunction solar cells*, Rep. Prog. Phys. **73**, 096401 (2010).

[14] Y. Zhou, C. Fuentes-Hernandez, T.M. Khan, J. Liu, J. Hsu, J.W. Shim, A. Dindar, J.P. Youngblood, R.J. Moon and B. Kippelen, *Recyclable organic solar cells on cellulose nanocrystal substrates*, Sci. Rep. **3**, 1536 (2013).

[15] Heliatek GmbH, *Heliatek consolidates its technology leadership by establishing a new world record for organic solar technology with a cell efficiency of 12%*, www.heliatek.com (2013).

[16] H. Sirringhaus, P.J. Brown, R.H. Friend, M.M. Nielsen, K. Bechgaard, B.M.W. Langeveld-Voss, A.J.H. Spiering, R.A.J. Janssen, E.W. Meijer, P. Herwig and D.M. de Leeuw, *Two-dimensional charge transport in self-organized, high-mobility conjugated polymers*, Nature **401**, 685 (1999).

[17] C.D. Dimitrakopoulos and P.R.L. Malenfant, *Organic thin film transistors for large area electronics*, Adv. Mater. **14**, 99 (2002).

[18] H. Klauk, *Organic thin-film transistors*, Chem. Soc. Rev. **39**, 2643 (2010).

[19] S. Paydavosi, K.E. Aidala, P.R. Brown, P. Hashemi, G.J. Supran, T.P. Osedach, J.L. Hoyt and V. Bulović, *Detection of charge storage on molecular thin films of tris(8-hydroxyquinoline) aluminum (Alq_3) by kelvin force microscopy: A candidate system for high storage capacity memory cells*, Nano Lett. **12**, 1260 (2012).

[20] M. Prezioso, A. Riminucci, P. Graziosi, I. Bergenti, R. Rakshit, R. Cecchini, A. Vianelli, F. Borgatti, N. Haag, M. Willis, A.J. Drew, W.P. Gillin and V.A. Dediu, *A single-device universal logic gate based on a magnetically enhanced memristor*, Adv. Mater. **25**, 534 (2013).

[21] E.M. Roeling, W.C. Germs, B. Smalbrugge, E.J. Geluk, T. de Vries, R.A.J. Janssen and M. Kemerink, *Organic electronic ratchets doing work*, Nat. Mater. **10**, 156 (2010).

[22] S.A. Wolf, D.D. Awschalom, R.A. Buhrman, J.M. Daughton, S. von Molnar, M.L. Roukes, A.Y. Chtchelkanova and D.M. Treger, *Spintronics: A spin-based electronics vision for the future*, Science **294**, 1488 (2001).

[23] I. Žutić, J. Fabian and S. Das Sarma, *Spintronics: Fundamentals and applications*, Rev. Mod. Phys. **76**, 323 (2004).

[24] R. Hanson, L.P. Kouwenhoven, J.R. Petta, S. Tarucha and L.M.K. Vandersypen, *Spins in few-electron quantum dots*, Rev. Mod. Phys. **79**, 1217 (2007).

[25] D.D. Awschalom, L.C. Bassett, A.S. Dzurak, E.L. Hu and J.R. Petta, *Quantum spintronics: Engineering and manipulating atom-like spins in semiconductors*, Science **339**, 1174 (2013).

[26] M.N. Baibich, J.M. Broto, A. Fert, F. Nguyen Van Dau, F. Petroff, P. Etienne, G. Creuzet, A. Friederich and J. Chazelas, *Giant magnetoresistance of (001)Fe/(001)Cr magnetic superlattices*, Phys. Rev. Lett. **61**, 2472 (1988).

[27] G. Binasch, P. Grünberg, F. Saurenbach and W. Zinn, *Enhanced magnetoresistance in layered magnetic structures with antiferromagnetic interlayer exchange*, Phys. Rev. B **39**, 4828 (1989).

[28] G. Szulczewski, S. Sanvito and M. Coey, *A spin of their own*, Nat. Mater. **8**, 693 (2009).

[29] W.J.M. Naber, S. Faez and W.G. van der Wiel, *Organic spintronics*, J. Phys. D **40**, R205 (2007).

[30] V.A. Dediu, L.E. Hueso, I. Bergenti and C. Taliani, *Spin routes in organic semiconductors*, Nat. Mater. **8**, 707 (2009).

[31] R.C. Johnson, R.E. Merrifield, P. Avakia and R.B. Flippen, *Effects of magnetic fields on the mutual annihilation of triplet excitons in molecular crystals*, Phys. Rev. Lett. **19**, 285 (1967).

[32] E.L. Frankevich and I.A. Sokolik, *On the mechanism of the magnetic field effect on anthracene photoconductivity*, Solid State Commun. **8**, 251 (1970).

[33] J. Kalinowski, M. Cocchi, D. Virgili, P. Di Marco and V. Valeria, *Magnetic field effects on emission and current in Alq_3-based electroluminescent diodes*, Chem. Phys. Lett. **380**, 710 (2003).

[34] T.L. Francis, Ö. Mermer, G. Veeraraghavan and M. Wohlgenannt, *Large magnetoresistance at room temperature in semiconducting polymer sandwich devices*, New. J. Phys. **6**, 185 (2004).

[35] Ö. Mermer, G. Veeraraghavan, T.L. Francis and M. Wohlgenannt, *Large magnetoresistance at room-temperature in small-molecular-weight or-*

ganic semiconductor sandwich devices, Solid State Commun. **134**, 631 (2005).

[36] Z.H. Xiong, D. Wu, Z.V. Vardeny and J. Shi, *Giant magnetoresistance in organic spin-valve*, Nature **427**, 821 (2004).

[37] M. Cinchetti, K. Heimer, J-P. Wustenberg, O. Andreyev, M. Bauer, S. Lach, C. Ziegler, Y. Gao, Y and M. Aeschlimann, *Determination of spin injection and transport in a ferromagnet/organic semiconductor heterojunction by two-photon photoemission*, Nat. Mater. **8**, 115 (2009).

[38] J-W. Yoo, C-Y. Chen, H.W. Jang, C.W. Bark, V.N. Prigodin, C.B. Eom and A.J. Epstein, *Spin injection/detection using an organic-based magnetic semiconductor*, Nat. Mater. **9**, 638 (2010).

[39] T.D. Nguyen, E. Ehrenfreund and Z.V. Vardeny, *Spin-polarized light-emitting diode based on an organic bipolar spin valve*, Science **337**, 204 (2012).

[40] J.M. Manriquez, G.T. Yee, R.S. McLean, A.J. Epstein and J.S. Miller, *A room-temperature molecular/organic-based magnet*, Science **252**, 1414 (1991).

[41] A.R. Rocha, V.M. Garcia-Suarez, S.W. Bailey, C.J. Lambert, J. Ferrer and S. Sanvito, *Towards molecular spintronics*, Nat. Mater. **4**, 335 (2005).

[42] J. Ferrer and V.M. Garcia-Suarez, *From microelectronics to molecular spintronics: an explorer's travelling guide*, J. Mater. Chem. **19**, 1696 (2009).

[43] G. Veeraraghavan, T.D. Nguyen, S. Yugang, Ö. Mermer and M. Wohlgenannt, *An 8 times 8 pixel array pen-input OLED screen based on organic magnetoresistance*, IEEE Trans. Electron Devices **54**, 1571 (2007).

[44] W.J. Baker, K. Ambal, D.P. Waters, R. Baarda, H. Morishita, K. van Schooten, D.R. McCamey, J.M. Lupton and C. Boehme, *Robust absolute magnetometry with organic thin-film devices*, Nat. Commun. **3**, 898 (2012).

[45] R.E. Peierls, *Quantum Theory of Solids* (Oxford University Press, 1955).

[46] H. Bässler, *Charge transport in disordered organic photoconductors*, Phys. Status Solidi B **175**, 15 (1993).

[47] V. Coropceanu, J. Cornil, D.A. da Silva Filho, Y. Olivier, R. Silbey and J-L. Brédas, *Charge transport in organic semiconductors*, Chem. Rev. **107**, 926 (2007).

[48] R. Coehoorn and P.A. Bobbert, *Effects of Gaussian disorder on charge*

carrier transport and recombination in organic semiconductors, Phys. Status Solidi A **209**, 2354 (2012).

[49] S. Stafström, *Electron localization and the transition from adiabatic to nonadiabatic charge transport in organic conductors*, Chem. Soc. Rev. **39**, 2484 (2010).

[50] A. Miller and E. Abrahams, *Impurity conduction at low concentrations*, Phys. Rev. **120**, 745 (1960).

[51] H.T. Nicolai, M. Kuik, G.A.H. Wetzelaer, B. de Boer, C. Campbell, C. Risko, J-L. Brédas and P.W.M. Blom, *Unification of trap-limited electron transport in semiconducting polymers*, Nat. Mater. **11**, 882 (2012).

[52] S.M. Sze and K.N. Kwok, *Physics of Semiconductor Devices* (Wiley, 2006).

[53] N.F. Mott and R.W. Gurney, *Electronic processes in ionic crystals* (Oxford University Press, 1940).

[54] R.H. Parmenter and W. Ruppel, *Two-carrier space-charge-limited current in a trap-free insulator*, J. Appl. Phys. **30**, 1548 (1959).

[55] L. Onsager, *Initial recombination of ions*, Phys. Rev. **54**, 554 (1938).

[56] P.W.M. Blom and M.C.J.M. Vissenberg, *Charge transport in poly(p-phenylene vinylene) light-emitting diodes*, Mater. Sci. Eng. R. **27**, 53 (2000).

[57] W. Wagemans, W.J. Engelen, F.L. Bloom and B. Koopmans, *Separating photocurrent and injected current contributions to the organic magnetoresistance*, Synth. Met. **160**, 266 (2010).

[58] Y. Cao, I.D. Parker, G. Yu, C. Zhang and A.J. Heger, *Improved quantum efficiency for electroluminescence in semiconducting polymers*, Nature **397**, 414 (1999).

[59] M. Wohlgenannt, K. Tandon, S. Mzumdar, S. Ramasesha and Z.V. Vardeny, *Formation cross-sections of singlet and triplet excitons in π-conjugated polymers*, Nature **409**, 494 (2001).

[60] J.S. Wilson, A.S. Dhoot, A.J.A.B. Seeley, M.S. Kahn, A. Köler and R.H. Friend, *Spin-dependent exciton formation in π-conjugated compounds*, Nature **413**, 828 (2001).

[61] M. Segal, M.A. Baldo, R.J. Holmes, S.R. Forrest and Z.G. Soos, *Excitonic singlet–triplet ratios in molecular and polymeric organic materials*, Phys. Rev. B **68**, 075211 (2003).

[62] M. Carvelli, R.A.J. Janssen and R. Coehoorn, *Determination of the exciton singlet-to-triplet ratio in single-layer organic light-emitting diodes*, Phys. Rev. B **83**, 075203 (2011).

[63] K. Schulten and P. Wolynes, *Semiclassical description of electron spin motion in radicals including the effect of hopping*, J. Chem. Phys. **68**, 3292 (1978).

[64] A.A. Zezin, V.I. Feldman, J.M. Warman, J. Wildeman and G. Hadzioannou, *EPR study of positive holes on phenylene vinylene chains: from dimer to polymer*, Chem. Phys. Lett. **389**, 108 (2004).

[65] S-Y. Lee, S-Y. Paik, D.R. McCamey, J. Yu, P.L. Burn, J.M. Lupton and C. Boehme, *Tuning hyperfine fields in conjugated polymers for coherent organic spintronics*, J. Am. Chem. Soc. **133**, 2019 (2011).

[66] P.A. Bobbert, W. Wagemans, F.W.A. van Oost, B. Koopmans and M. Wohlgenannt, *Theory for spin diffusion in disordered organic semiconductors*, Phys. Rev. Lett. **102**, 156604 (2009).

[67] T.D. Nguyen, Y. Sheng, J. Rybicki, G. Veeraraghavan and M. Wohlgenannt, *Device-spectroscopy of magnetic field effects in several different polymer organic light-emitting diodes*, Synth. Met. **160**, 320 (2010).

[68] P.A. Bobbert, T.D. Nguyen, F.W.A. van Oost, B. Koopmans and M. Wohlgenannt, *Bipolaron mechanism for organic magnetoresistance*, Phys. Rev. Lett. **99**, 216801 (2007).

[69] V.N. Prigodin, J.D. Bergeson, D.M. Lincoln and A.J. Epstein, *Anomalous room temperature magnetoresistance in organic semiconductors*, Synth. Met. **156**, 757 (2006).

[70] P. Desai, P. Shakya, T. Kreouzis, W.P. Gillin, N.A. Morley and M.R.J. Gibbs, *Magnetoresistance and efficiency measurements of Alq_3-based OLEDs*, Phys. Rev. B **75**, 094423 (2007).

[71] R.C. Johnson and R.E. Merrifield, *Effects of magnetic fields on the mutual annihilation of triplet excitons in anthracene crystals*, Phys. Rev. B **1**, 896 (1970).

[72] A. Jabłoński, *Efficiency of anti-Stokes fluorescence in dyes*, Nature **131**, 839 (1933).

[73] M.N. Bussac and Z. Zuppiroli, *Bipolaron singlet and triplet states in disordered conducting polymers*, Phys. Rev. B **47**, 5493 (1993).

[74] Z.V. Vardeny, E. Ehrenfreund, O. Brafman, M. Nowak, H. Schaffer, A.J.

Heeger and F. Wudl, *Photogeneration of confined soliton pairs (bipolarons) in polythiophene*, Phys. Rev. Lett. **56**, 671 (1986).

[75] N.J. Harmon and M.E. Flatté, *Spin-flip induced magnetoresistance in positionally disordered organic solids*, Rev. Rev. Lett. **108**, 186602 (2012).

[76] N.J. Harmon and M.E. Flatté, *Semiclassical theory of magnetoresistance in positionally disordered organic semiconductors*, Rev. Rev. B **85**, 075204 (2012).

[77] J.D. Bergeson, V.N. Prigodin, D.M. Lincoln and A.J. Epstein, *Inversion of magnetoresistance in organic semiconductors*, Phys. Rev. Lett. **100**, 067201 (2008).

[78] M. Cox, P. Janssen, F. Zhu and B. Koopmans, *Traps and trions as origin of magnetoresistance in organic semiconductors*, Phys. Rev. B **88**, 035202 (2013).

[79] A.J. Schellekens, W. Wagemans, S.P. Kersten, P.A. Bobbert and B. Koopmans, *Microscopic modeling of magnetic-field effects on charge transport in organic semiconductors*, Phys. Rev. B **84**, 075204 (2011).

[80] R. Österbacka, M. Wohlgenannt, D. Chinn and Z.V. Vardeny, *Optical studies of triplet excitations in poly(p-phenylene vinylene)*, Phys. Rev. B **60**, R11253 (1999).

[81] U.E. Steiner and T. Ulrich, *Magnetic field effects in chemical kinetics and related phenomena*, Chem. Rev. **89**, 51 (1989).

[82] C.F.O. Graeff, G.B. Silva, F. Nüesch and L. Zuppiroli, *Transport and recombination in organic light-emitting diodes studied by electrically detected magnetic resonance*, Eur. Phys. J. E **18**, 21 (2005).

[83] F.L. Bloom, *Exploring organic magnetoresistance: An investigation of microscopic and device properties*, Ph.D. thesis, Eindhoven University of Technology (2010).

[84] V. Dyakonov, G. Zoriniants, M. Scharber, C.J. Brabec, R.A.J. Janssen, J.C. Hummelen and N.S. Sariciftci, *Photoinduced charge carriers in conjugated polymer–fullerene composites studied with light-induced electron-spin resonance*, Phys. Rev. B **59**, 8019 (1999).

[85] J. de Ceuster, E. Goovaerts, A. Bouwen, J.C. Hummelen and V. Dyakonov, *High-frequency (95 Ghz) electron paramagnetic resonance study of the photoinduced charge transfer in conjugated polymer–fullerene composites*, Phys. Rev. B **64**, 195206 (2001).

[86] W. Wagemans, F.L. Bloom, P.A. Bobbert, M. Wohlgenannt and B. Koop-

mans, *A two-site bipolaron model for organic magnetoresistance*, J. Appl. Phys. **103**, 07F303 (2008).

[87] T.D. Nguyen, G. Hukic-Markosian, F. Wang, L. Wojcik, X-G. Li, E. Ehrenfreund and Z.V. Vardeny, *Isotope effect in spin response of π-conjugated polymer films and devices*, Nat. Mater. **9**, 345 (2010).

[88] T.D. Nguyen, B.R. Gautam, E. Ehrenfreund and Z.V. Vardeny, *Magnetoconductance response in unipolar and bipolar organic diodes at ultrasmall fields*, Phys. Rev. Lett. **105**, 166804 (2010).

[89] S.P. Kersten, A.J. Schellekens, B. Koopmans and P.A. Bobbert, *Magnetic-field dependence of the electroluminescence of organic light-emitting diodes: A competition between exciton formation and spin mixing*, Phys. Rev. Lett. **106**, 197402 (2011).

[90] P.W.M. Blom, V.D. Mihailetchi, L.J.A. Koster and D.E. Markov, *Device physics of polymer:fullerene bulk heterojunction solar cells*, Adv. Mater. **19**, 1551 (2007).

[91] F.L. Bloom, M. Kemerink, W. Wagemans and B. Koopmans, *Sign inversion of magnetoresistance in space-charge limited organic devices*, Phys. Rev. Lett. **103**, 066601 (2009).

[92] K. Maturová, S.S. van Bavel, M.M. Wienk, R.A.J. Janssen and M. Kemerink, *Morphological device model for organic bulk heterojunction solar cells*, Nano Lett. **9**, 3032 (2009).

[93] K. Maturová, S.S. van Bavel, M.M. Wienk, R.A.J. Janssen and M. Kemerink, *Description of the morphology dependent charge transport and performance of polymer:fullerene bulk heterojunction solar cells*, Adv. Funct. Mater. **21**, 261 (2011).

[94] G.G. Malliaras, J.R. Salem, P.J. Brock and J.C. Scott, *Photovoltaic measurement of the built-in potential in organic light emitting diodes and photodiodes*, J. Appl. Phys. **84**, 1583 (1998).

[95] M. Cox, P. Janssen, S.H.W. Wouters, E.H.M. van der Heijden, M. Kemerink and B. Koopmans, *The influence of device physics on organic magnetoresistance*, Synth. Met. **173**, 10 (2013).

[96] V.A. Dediu, L.E. Hueso, I. Bergenti, A. Riminucci, F. Borgatti, P. Graziosi, C. Newby, F. Casoli, M.P. de Jong, C. Taliani and Y. Zhan, *Room-temperature spintronic effects in Alq_3-based hybrid devices*, Phys. Rev. B **78**, 115203 (2008).

[97] T.S. Santos, J.S. Lee, P. Migdal, I.C. Lekshmi, B. Satpati and J.S. Moodera, *Room-temperature tunnel magnetoresistance and spin-polarized tunnel-*

ing through an organic semiconductor barrier, Phys. Rev. Lett. **98**, 016601 (2007).

[98] W. Xu, G.J. Szulczewski, P. LeClair, I. Navarrete, R. Schad, G. Miao, H. Guo and A. Gupta, *Tunneling magnetoresistance observed in $La_{0.67}Sr_{0.33}MnO_3$/organic molecule/Co junctions*, Appl. Phys. Lett. **90**, 072506 (2007).

[99] J.H. Shim, K.V. Raman, Y.J. Park, T.S. Santos, G.X. Miao, B. Satpati and J.S. Moodera, *Large spin diffusion length in an amorphous organic semiconductor*, Phys. Rev. Lett. **100**, 226603 (2008).

[100] J.J.H.M. Schoonus, P.G.E. Lumens, W. Wagemans, J.T. Kohlhepp, P.A. Bobbert, H.J.M. Swagten and B. Koopmans, *Magnetoresistance in hybrid organic spin valves at the onset of multiple-step tunneling*, Phys. Rev. Lett. **103**, 146601 (2009).

[101] C. Barraud, P. Seneor, R. Mattana, S. Fusil, K. Bouzehouane, C. Deranlot, P. Graziosi, L. Hueso, I. Bergenti, V.A. Dediu, F. Petroff and A. Fert, *Unravelling the role of the interface for spin injection into organic semiconductors*, Nat. Phys. **6**, 615 (2010).

[102] F.L. Bloom, W. Wagemans, M. Kemerink and B. Koopmans, *Separating positive and negative magnetoresistance in organic semiconductor devices*, Phys. Rev. Lett. **99**, 257201 (2007).

[103] P. Desai, P. Shakya, T. Kreouzis and W.P. Gillin, *The role of magnetic fields on the transport and efficiency of aluminum tris(8-hydroxyquinoline) based organic light emitting diodes*, J. Appl. Phys. **102**, 073710 (2007).

[104] B. Hu and Y. Wu, *Tuning magnetoresistance between positive and negative values in organic semiconductors*, Nat. Mater. **6**, 985 (2007).

[105] U. Niedermeier, M. Vieth, R. Patzold, W. Sarfert and H. von Seggern, *Enhancement of organic magnetoresistance by electrical conditioning*, Appl. Phys. Lett. **92**, 193309 (2008).

[106] F.J. Wang, H. and Bässler and V.Z. Vardeny, *Magnetic field effects in π-conjugated polymer–fullerene blends: Evidence for multiple components*, Phys. Rev. Lett. **101**, 236805 (2008).

[107] Y. Sheng, T.D. Nguyen, G. Veeraraghavan, Ö. Mermer, M. Wohlgenannt, S. Qiu and U. Scherf, *Hyperfine interaction and magnetoresistance in organic semiconductors*, Phys. Rev. B **74**, 045213 (2006).

[108] P.A. Bobbert, T.D. Nguyen, W. Wagemans, F.W.A. van Oost, B. Koopmans and M. Wohlgenannt, *Spin relaxation and magnetoresistance in disordered organic semiconductors*, Synth. Met. **160**, 223 (2010).

[109] R. Liu, Y. Zhang, Y.L. Lei, P. Chen and Z.H. Xiong, *Magnetic field dependent triplet–triplet annihilation in Alq_3-based organic light emitting diodes at different temperatures*, J. Appl. Phys. **105**, 093719 (2009).

[110] Ö. Mermer, G. Veeraraghavan, T.L. Francis, Y. Sheng, T.D. Nguyen, M. Wohlgenannt, A. Köhler, M.K. Al-Suti and M.S. Khan, *Large magnetoresistance in nonmagnetic π-conjugated semiconductor thin film devices*, Phys. Rev. B **72**, 205202 (2005).

[111] F.L. Bloom, W. Wagemans and B. Koopmans, *Temperature dependent sign change of the organic magnetoresistance effect*, J. Appl. Phys. **103**, 07F320 (2008).

[112] S.A. Bagnich, U. Niedermeier, C. Melzer, W. Sarfert and H. von Seggern, *Electron–hole pair mechanism for the magnetic field effect in organic light emitting diodes based on poly(paraphenylene vinylene)*, J. Appl. Phys. **106**, 113702 (2009).

[113] S. Zhang, A.J. Drew, T. Kreouzis and W.P. Gillin, *Modelling of organic magnetoresistance as a function of temperature using the triplet polaron interaction*, Synth. Met. **161**, 628 (2011).

[114] N.J. Rolfe, M. Heeney, P.B. Wyatt, A.J. Drew, T. Kreouzis and W.P. Gillin, *Elucidating the role of hyperfine interactions on organic magnetoresistance using deuterated aluminium tris(8-hydroxyquinoline)*, Phys. Rev. B **80**, 241201 (2009).

[115] W. Wagemans, P. Janssen, E.H.M. van der Heijden, M. Kemerink and B. Koopmans, *Frequency dependence of organic magnetoresistance*, Appl. Phys. Lett. **97**, 123301 (2010).

[116] W.P. Gillin, S. Zhang, N.J. Rolfe, P. Desai, P. Shakya, A.J. Drew and T. Kreouzis, *Determining the influence of excited states on current transport in organic light emitting diodes using magnetic field perturbation*, Phys. Rev. B **82**, 195208 (2010).

[117] W. Wagemans, A.J. Schellekens, M. Kemper, F.L. Bloom, P.A. Bobbert and B. Koopmans, *Spin–spin interactions in organic magnetoresistance probed by angle-dependent measurements*, Phys. Rev. Lett. **106**, 196802 (2011).

[118] J. Rybicki, R. Lin, F. Wang, M. Wohlgenannt, C. He, T. Sanders and Y. Suzuki, *Tuning the performance of organic spintronic devices using X-ray generated traps*, Phys. Rev. Lett. **109**, 076603 (2012).

[119] P. Janssen, M. Cox, S.H.W. Wouters, M. Kemerink, M.M. Wienk and B. Koopmans, *Tuning organic magnetoresistance in polymer-fullerene*

blends by controlling spin reaction pathways, Nat. Commun. (2013), In Press.

[120] W. Wagemans, P. Janssen, A.J. Schellekens, F.L. Bloom, P.A. Bobbert and B. Koopmans, *The many faces of organic magnetoresistance*, SPIN **1**, 93 (2011).

[121] J.Y. Song, N. Stingelin, A.J. Drew, T. Kreouzis and W.P. Gillin, *Effect of excited states and applied magnetic fields on the measured hole mobility in an organic semiconductor*, Phys. Rev. B **82**, 085205 (2010).

[122] D. Hertel and K. Meerholz, *Triplet–polaron quenching in conjugated polymers*, J. Phys. Chem. B **111**, 12075 (2007).

[123] M. Kuik, L.J.A. Koster, G.A.H. Wetzelaer and P.W.M. Blom, *Trap-assisted recombination in disordered organic semiconductors*, Phys. Rev. Lett. **107**, 256805 (2011).

[124] A. Kadashchuk, V.I. Arkhipov, C-H. Kim, J. Shinar, D-W. Lee, Y-R. Hong, J-I. Jin, P. Heremans and H. Bässler, *Localized trions in conjugated polymers*, Phys. Rev. B **76**, 235205 (2007).

[125] M. Kemerink, J.M. Kramer and H.H.P. Gommans, *Temperature-dependent built-in potential in organic semiconductor devices*, Appl. Phys. Lett. **88**, 192108 (2006).

[126] G. Silvestre, M. Johnson, A. Giraldo and J. Shannon, *Light degradation and voltage drift in polymer light-emitting diodes*, Appl. Phys. Lett. **78**, 1619 (2001).

[127] W. Wagemans and B. Koopmans, *Spin transport and magnetoresistance in organic semiconductors*, Phys. Status Solidi B **248**, 1029 (2011).

[128] C. Deibel, T. Stroble and V. Dyakonov, *Role of the charge transfer state in organic donor–acceptor solar cells*, Adv. Mater. **22**, 4097 (2010).

[129] J.K.J. van Duren, X. Yang, J. Loos, C.W.T. Bulle-Lieuwma, A.B. Sieval, J.C. Hummelen and R.A.J. Janssen, *Relating the morphology of poly(p-phenylene vinylene)/methanofullerene blends to solar-cell performance*, Adv. Funct. Mater. **14**, 425 (2004).

[130] V.D. Mihailetchi, J.K.J. van Duren, P.W.M. Blom, J.C. Hummelen, R.A.J. Janssen, J.M. Kroon, M.T. Rispens, W.J.H. Verhees and M.M Wienk, *Electron transport in a methanofullerene*, Adv. Funct. Mater. **13**, 43 (2003).

[131] H.O.H. Churchill, A.J. Bestwick, J.W. Harlow, F. Kuemmeth, D. Marcos, C.H. Stwertka, S.K. Watson and C.M. Marcus, *Electron–nuclear interaction in ^{13}C nanotube double quantum dots*, Nat. Phys. **5**, 321 (2009).

[132] Y. Wu, Z. Xu, B. Hu and J. Howe, *Tuning magnetoresistance and magnetic-field-dependent electroluminescence through mixing a strong-spin–orbital-coupling molecule and a weak-spin–orbital-coupling polymer*, Phys. Rev. B **75**, 035214 (2007).

[133] Z.G. Yu, *Spin–orbit coupling, spin relaxation, and spin diffusion in organic solids*, Phys. Rev. Lett. **106**, 106602 (2011).

[134] A.S. Alexandrov, V.A. Dediu and V.V. Kabanov, *Hopping magnetotransport via nonzero orbital momentum states and organic magnetoresistance*, Phys. Rev. Lett. **108**, 186601 (2012).

[135] J. Behrends, A. Schnegg, K. Lips, E.A. Thomsen, A.K. Pandey, I.D.W. Samuel and D.J. Keeble, *Bipolaron formation in organic solar cells observed by pulsed electrically detected magnetic resonance*, Phys. Rev. Lett. **105**, 176601 (2010).

[136] D. Veldman, S.C.J. Meskers and R.A.J. Janssen, *The energy of charge transfer states in electron donor–acceptor blends: Insight into the energy losses in organic solar cells*, Adv. Funct. Mater. **19**, 1939 (2009).

[137] F. Piersimoni, S. Chambon, K. Vandewal, R. Mens, T. Boonen, A. Gadisa, M. Izquierdo, S. Filippone, B. Ruttens, J. D'Haen, N. Martin, L. Lutsen, D. Vanderzande, P. Adriaensens and J.V. Manca, *Influence of fullerene ordering on the energy of the charge-transfer state and open-circuit voltage in polymer:fullerene solar cells*, J. Phys. Chem. C **115**, 10873 (2011).

[138] S.P. Kersten, S.C.J. Meskers and P.A. Bobbert, *Route towards huge magnetoresistance in doped polymers*, Phys. Rev. B **86**, 045210 (2012).

[139] S.E. Shaheen, G.E. Jabbour, M.M. Morrell, Y. Kawabe, B. Kippelen, N. Peyghambarian, M-F. Nabor, R. Schlaf, E.A. Mash and N.R. Armstrong, *Bright blue organic light-emitting diode with improved color purity using a LiF/Al cathode*, J. Appl. Phys. **84**, 2324 (1998).

[140] D. Veldman, I. Özlem, S.C.J. Meskers, J. Sweelssen, M.M. Koetse, S.C. Veenstra, J.M. Kroon, S.S. van Bavel, J. Loos and R.A.J. Janssen, *Compositional and electric field dependence of the dissociation of charge transfer excitons in alternating polyfluorene copolymer–fullerene blends*, J. Am. Chem. Soc. **130**, 7721 (2008).

[141] A.P. Monkman, H.D. Burrows, L.J. Hartwell, L.E. Horsburgh, I. Hamblett and S. Navaratnam, *Triplet energies of π-conjugated polymers*, Phys. Rev. Lett. **86**, 1358 (2001).

[142] A. Köhler and D. Beljonne, *The singlet–triplet exchange energy in conjugated polymers*, Adv. Func. Mater. **14**, 11 (2004).

[143] A. Köhler and H. Bässler, *Triplet states in organic semiconductors*, Mater. Sci. Eng. R **66**, 71 (2009).

[144] V. Jankus, E.W. Snedden, D.W. Bright, V.L. Whittle, J.A.G. Williams and A. Monkman, *Energy upconversion via triplet fusion in Super Yellow PPV films doped with palladium tetraphenyltetrabenzoporphyrin: a comprehensive investigation of exciton dynamics*, Adv. Funct. Mater. **23**, 384 (2013).

[145] Y. Kim, S.A. Choulis, J. Nelson, D.D.C. Bradley, S. Cook and J.R. Durrant, *Composition and annealing effects in polythiophene/fullerene solar cells*, J. Mater. Sci. **40**, 1371 (2005).

[146] B. Hu, L. Yan and M. Shao, *Magnetic-field effects in organic semiconducting materials and devices*, Adv. Mater. **21**, 1500 (2009).

[147] M.A. Baldo and S.R. Forrest, *Transient analysis of organic electrophosphorescence: Transient analysis of triplet energy transfer*, Phys. Rev. B **62**, 10958 (2000).

[148] S.A. Bagnich, U. Niedermeier, C. Melzer, W. Sarfert and H. von Seggern, *Origin of magnetic field effect enhancement by electrical stress in organic light emitting diodes*, J. Appl. Phys. **105**, 123706 (2009).

[149] H.C.F. Martens, J.N. Huiberts and P.W.M. Blom, *Simultaneous measurement of electron and hole mobilities in polymer light-emitting diodes*, Appl. Phys. Lett. **77**, 1852 (2000).

[150] H.H.P. Gommans, M. Kemerink and R.A.J. Janssen, *Negative capacitances in low-mobility solids*, Phys. Rev. B **72**, 235204 (2005).

[151] M.S. Meruvia, J.A. Freire, I.A. Hümmelgen, J. Gruber and C.F.O. Graeff, *Magnetic field release of trapped charges in poly (fluorenylenevinylene)s*, Org. Electron. **8**, 695 (2007).

[152] S. Majumdar, H.S. Majumdar, H. Aarnio and R. Österbacka, *Hysteretic magnetoresistance in polymeric diodes*, Phys. Status Solidi (RRL) **3**, 242 (2009).

[153] H.H.P. Gommans, M. Kemerink, G.G. Andersson and R.M.T. Pijper, *Charge transport and trapping in Cs-doped poly(dialkoxy-p-phenylene vinylene) light-emitting diodes*, Phys. Rev. B **69**, 155216 (2004).

[154] J. Shao and G.T. Wright, *Characteristics of the space-charge-limited dielectric diode at very high frequencies*, Solid-State Electron. **3**, 291 (1961).

[155] T.D. Nguyen, E. Ehrenfreund and Z.V. Vardeny, *Organic magnetoresis-*

tance at small magnetic fields: Compass effect, Org. Electron. (2013), In Press.

[156] R.N. Mahato, H. Lülf, M.H. Siekman, S.P. Kersten, P.A. Bobbert, M.P. de Jong, L. de Cola and W.G. van der Wiel, *Ultrahigh magnetoresistance at room temperature in molecular wires*, Science (2013), In Press.

Index

Δg-mechanism, 24, 28, 77

Admittance, 106
Alq_3, 7
Anode, *see* Electrode

Bipolaron, 20, 26
Bipolaron mechanism, 20, 28, 31
Branching ratio, 21, 44, 45
Built-in voltage, 16

Cathode, *see* Electrode
Charge-transfer state, 25, 26, 66, 69, 76, 82, 91, 94
Conjugated polymer, *see* Organic semiconductor
CTS, *see* Charge-transfer state

Device model, 29–32
Disorder, 14, 21, 45
Dissociation, 22, 47, 56, 59, 77
Double-carrier device, 16
Doublet, 24

e–h mechanism, *see* Electron–hole mechanism
e–h pair, *see* Electron–hole pair
Electrode, 15, 51, 86
Electron–hole mechanism, 20, 22, 28, 31
Electron–hole pair, 17, 26
Empirical lineshapes, 38–40, 42
Energy diagram, 20, 23, 25, 26, 52, 68, 81, 89, 90
Exciton, 18, 26

Fast hopping, 28, 41, 46

hf, *see* Hyperfine field
HFE, *see* High-field effect
High-field effect, 20, 23–24, 55, 58, 75, 80–83, 98
Highest occupied molecular orbit, 14, 15
HOMO, *see* Highest occupied molecular orbit
Hopping transport, 15
Hyperfine field, 18, 26, 38, 57, 76, 77, 95

Intermediate hopping, 41, 46

Jabłoński diagram, *see* Energy diagram

LFE, *see* Low-field effect
Lorentzian lineshape, 36
Low-field effect, 20–23, 55, 57, 75, 80–83, 98

Lowest unoccupied molecular orbit, 14, 15
LUMO, *see* Lowest unoccupied molecular orbit

Magnetoconductance, 30
MC, *see* Magnetoconductance
MDMO-PPV, 7
Mixing, *see* Spin mixing
Mobility, 17
Monte Carlo simulation, 21, 44

Non-Lorentzian lineshape, 36

Ohmic contact, 16
OLED, *see* Organic light-emitting diode
OMAR, *see* Organic magnetoresistance
OPV, *see* Organic photovoltaic cell
Organic electronics, 6
Organic light-emitting diode, 6
Organic magnetoresistance, 10, 19
Organic photovoltaic cell, 7
Organic semiconductor, 6
  Charge transport, 14
  Conduction, 14
  Examples, 7
Organic spintronics, 9
OSC, *see* Organic semiconductor

PCBM, 7
Percolation, 21, 77
Photocurrent, 17
Polaron, 14

Quartet, 24, 26

Recombination, 16, 22, 59, 92
Recombination mobility, 17, 22, 30, 78, 84

SCLC, *see* Space-charge limited current
Single-carrier device, 16
Singlet, 18, 26
Singlet–triplet ratio, 18, 19, 22
Site, 15
Slow hopping, 27, 29, 38
Small molecule, *see* Organic semiconductor
Space-charge limited current, 16
Spin blocking, 21
Spin mixing, 19, 21–25, 29
Spin precession, 18, 24, 29, 42
Spin–orbit interaction, 18
Spintronics, 8
Stochastic Liouville equation, 28, 59
SY-PPV, 7

Transit time, 102, 109
Trap, 15, 23, 32, 54, 82, 102, 108
Trions, 23, 24, 26, 31, 55, 56
Triplet, 18, 26
Triplet–polaron mechanism, 20, 22, 28, 31
Triplet–triplet mechanism, 20, 24
Two-site model, 27, 41, 43

Ultra-small field effect, 29, 47, 58
USFE, *see* Ultra-small field effect

Voltage dependence, 31, 46, 55, 57, 58, 78–80, 83–84, 105

Zero-field splitting, 24, 26, 58, 77
ZFS, *see* Zero-field splitting


ENERGY
RESULT
DISORDER
CONDUCTION
CHARGE-TRANSFER
HOLE
ELECTRODE
QUANTUM
STATE
ZERO-FIELD
SENSOR
FULLERENE
LFE
PPV
NOVEL
TRAP
FREQUENCY
MODEL
SPACE-CHARGE
DEVICE
KNOWLEDGE
G-FACTOR
FIELD
TUNING
NEGATIVE
OMAR
SEMICONDUCTOR
DEMONSTRATE
MOLECULES
CHEMISTRY
ELECTRON
TRANSFER
INFLUENCE
UNIPOLAR
RECOMBINATION
GLOVEBOX
PERCOLATION
MOBILITY
EXCITON
BLEND
MODELING
ULTRA-SMALL
HIGH-FIELD
LINESHAPE
PHOTOVOLTAIC
LIGHT-EMITTING
JUNCTION
DOUBLET
HOLE
PAIR
TRIPLET
LOW-FIELD
NOVEL-LOW-FIELD
EXCITON
HOLE-DEPENDENCE
FULLERENE
INTERACTION
SITE
DISSOCIATION
GLOVEBOX
ELECTRODE
PAIR
RESEARCH
OMAR
REACTIONS
DIAGRAM
SPACE-CHARGE
PHYSICS
QUARTET
G-FACTOR
TRIONBLOCKING
TUNING
PARTICLES
SIMULATION
TRAP
NEGATIVE
ELECTRONICS
CHARGE
EFFICIENCY
DEMONSTRATE
MODEL
DEPENDENCE
POSITIVE
EQUATION
TRIPLET
TRIONS
PUZZLING
OMAR
DISSOCIATION
ADMITTANCE
FULLERENE
BLEND
LOW-FIELD
DIODE
SPINTRONICS
ORGANIC
VOLTAGE
SENSOR
DIAGRAM
MIXING
RESULT
MOLECULES
CHEMISTRY
ELECTRODE
DISSOCIATION
PUZZLING
SPINTRONICS
FULLERENE
SINGLE
PARTICLES
SENSOR
TRAP
ANALYSIS
EQUATION
EFFECT
QUANTUM
TUNING
ELECTRON
CATHODE
TRIPLET
DIODE
MECHANISM
DISORDER
SPACE-CHARGE
REACTIONS
NEGATIVE
BIPOLARON
TRANSPORT